Investigation on control of graphene interlayer interaction by nanospacer insertion

DING MINGDA

Supervisor: Prof. Yoshihiro Kobayashi

Department of Applied Physics
Graduate School of Engineering
Osaka University

Doctoral Dissertation

December 2024

Abstract

Monolayer graphene is renowned for its exceptional properties in various fields, making it a highly promising material for applications. Its unique linear electronic dispersion leads to high carrier mobility and wavelength-independent uniform light absorption. However, in the multilayer AB-stacking graphene, the strong interlayer interactions, result in a parabolic electronic dispersion that undermines the performance. It is essential to reduce interlayer interactions and preserve the intrinsic property of each layer. Moreover, the porous 3D sponge graphene structure has promising applications in energy storage, environmental remediation, and sensor technology due to its high surface area, conductivity, and mechanical resilience. The material's porosity and interlayer spacing critically influence its performance. Understanding and optimizing the microstructure are essential to tailor the material's performance.

The strategy of this dissertation is to reduce the interlayer interactions of multilayer graphene with the insertion of nanomaterials, such as carbon nanotubes (CNTs) and nanodiamonds (NDs). These nanospacers increase the interlayer distance, weakening the interlayer coupling and altering the properties of the stacked graphene layers. To obtain a systematical understanding of the phenomena and mechanism, both experimental study and theoretical analysis were conducted. The simulations can overcome experimental limitations in illustrating microstructures and difficulties in controlling variables. The study also accumulated experience in increasing the monolayer ratio in the graphene sponge structure.

The first part of this dissertation focuses on the effect of CNT insertion in multilayer graphene. Graphene-CNT (Gr-CNT) stacking structures were experimentally fabricated via dry transfer, enabling precise control over the layer number and CNT insertion. Atomic force microscopy (AFM) and Raman spectroscopy confirmed the increase in interlayer distance and reduction in interlayer interaction, respectively. Molecular dynamics (MD) simulations further explored the impact of CNT diameter and inter-tube distance on the microstructure. Two distinct stable configurations: separation and adhesion were observed, determined by the CNT geometric parameters and the difference in potential energy.

The second part investigated graphene-ND (Gr-ND) stacking structures. Unlike CNTs, NDs provide point-like contact, minimizing the impact on graphene's intrinsic properties

while the larger size can further increase the interlayer distance. The Raman spectroscopy and AFM experimentally verified the reduced interlayer interaction and layer separation. The MD simulation and continuum model analysis were conducted to predict the critical inter-ND distance for the interlayer separation.

In the third part, the property modulations of Gr-CNT and Gr-ND structures are studied. Firstly, the mechanical behavior of Gr-CNT structures is studied from a microscopic view. MD simulations studied the effect of CNT wall numbers and initial configurations on the stable structures. The loading-unloading curves exhibit hysteresis and energy dissipation due to the bi-stable nature of the system. The dissipation was experimentally verified in multilayer Gr-CNT. Secondly, the electrical transport measurement was experimentally implemented for the Gr-ND stacking system. The non-linear I-V curve was obtained which comes from the tunneling current through ND spacers. Such nonlinearity has potential applications for physical neural network devices.

In this dissertation, the multilayer Gr-CNT and Gr-ND stacking structures were separately studied by combining experiment and simulation. The spacer effect on the interlayer interaction and microstructure was illustrated. The differences between the two spacers were compared. Then, the bi-stable microstructure and hysteresis mechanical behavior of the Gr-CNT stacking system were unveiled. Finally, the non-linear I-V property of the Gr-ND stacking system was studied. The contributions of this dissertation include the layer-controllable fabrication method, atomistic insight, and property adjustment. These studies advance the understanding of interlayer interactions in multilayer graphene and pave the way for optimizing graphene-based materials for high-performance applications.

Table of contents

List of figures

List of tables

Chapter 1

Introduction

1.1 Family of low-dimensional carbon materials

The discovery of carbon nanotubes in 1991 [1] and the isolation of monolayer graphene in 2004 [2, 3] marked the beginning of a revolutionary research era in low-dimensional materials. These breakthroughs revealed previously unimaginable properties and opened up promising avenues for applications, sparking intense interest among researchers and engineers to explore and harness these materials.

Over the past decades, the family of low-dimensional materials has expanded significantly. Based on their nanoscale dimensionality (Figure 1.1), these materials can be categorized into:

- Two-dimensional (2D) materials, represented by graphene, hexagonal boron nitride (hBN), and transition-metal dichalcogenides (TMDCs);
- One-dimensional (1D) materials, including carbon nanotubes (CNTs) and graphene nanoribbons;
- Zero-dimensional (0D) materials, such as nanodiamonds (NDs) and fullerenes.

Among these novel materials, low-dimensional carbon materials, particularly graphene, have attracted the most attention. Graphene stands out for its exceptional properties and wide-ranging applications, making it a key focus of scientific research.

This dissertation investigates the role of nanospacers in modifying the microstructure and properties of multilayer-stacked graphene. NDs and CNTs are explored as potential nanospacer candidates. The following section provides a concise overview of the properties, synthesis methods, and applications of these three materials.

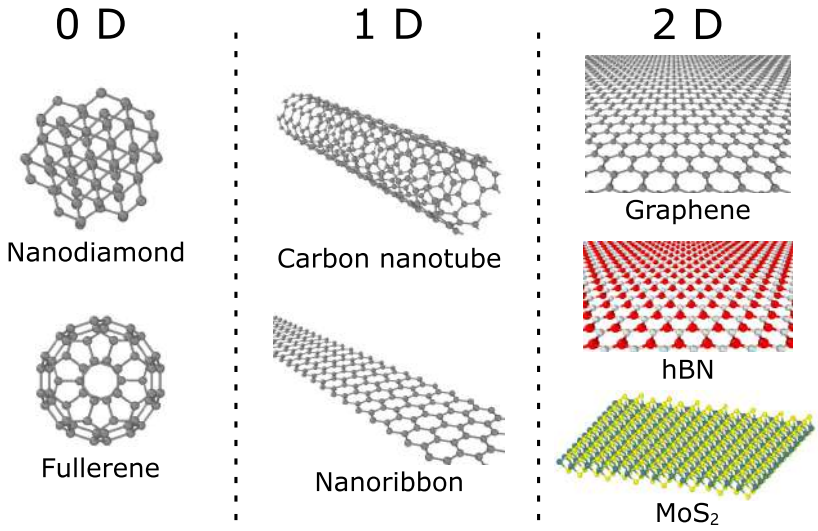

Fig. 1.1 The family of low-dimensional materials.

1.2 Introduction of graphene

Monolayer graphene consists of a single layer of carbon atoms arranged in a hexagonal lattice [2, 4]. Structurally, the carbon atoms exhibit sp^2 hybridization, with C-C bond angles of 120°, forming a flat honeycomb structure. This monolayer of carbon also serves as the fundamental building block for other carbon-based materials, including graphite, CNTs, and fullerenes [3]. Its unique atomic structure leads to exceptional physical and chemical properties, which have been widely studied since its first mechanical exfoliation in 2004. This section offers a basic overview of graphene's significance in advanced materials science, highlighting its key properties, fabrication methods, and the wide range of applications.

1.2.1 Properties of graphene

Graphene shows extraordinary properties in various fields. The unique lattice structure of graphene determines its properties. Graphene has a honeycomb lattice structure (see Figure 1.2a). Each carbon atom is bonded to its three nearest neighbors with a carbon-carbon bond length of approximately $a_{C-C} \approx 1.42$ Å. The honeycomb lattice can be characterized as a Bravais lattice with a basis of two atoms, indicated as A and B, and these contribute a total of two π electrons per unit cell to the electronic properties of graphene. The primitive unit cell of the Bravais lattice can be considered a rhombus with side $a = \sqrt{3}a_{C-C} = 2.46$ Å. The

primitive unit vectors are

$$\mathbf{a}_1 = \left(\frac{\sqrt{3}a}{2}, \frac{a}{2}\right), \mathbf{a}_2 = \left(\frac{\sqrt{3}a}{2}, -\frac{a}{2}\right). \tag{1.1}$$

The reciprocal lattice of graphene is also a hexagonal lattice but rotated 90° from the real space (see Figure 1.2b). The reciprocal lattice vectors are

$$\mathbf{b}_1 = \left(\frac{2\pi}{\sqrt{3}a}, \frac{2\pi}{a}\right), \mathbf{b}_2 = \left(\frac{2\pi}{\sqrt{3}a}, -\frac{2\pi}{a}\right). \tag{1.2}$$

The first Brillouin zone is hexagonal with an area of $8\pi^2/\sqrt{3}a^2$. There are three key locations of high symmetry in the Brillouin zone, the Γ-point, the M-point, and the K-point. The Γ-point is at the center of the Brillouin zone, the K point is the corner of the first Brillouin, and the M point is the center point of the first Brillouin side. Thus, there are six K-points and six M-points within the Brillouin zone.

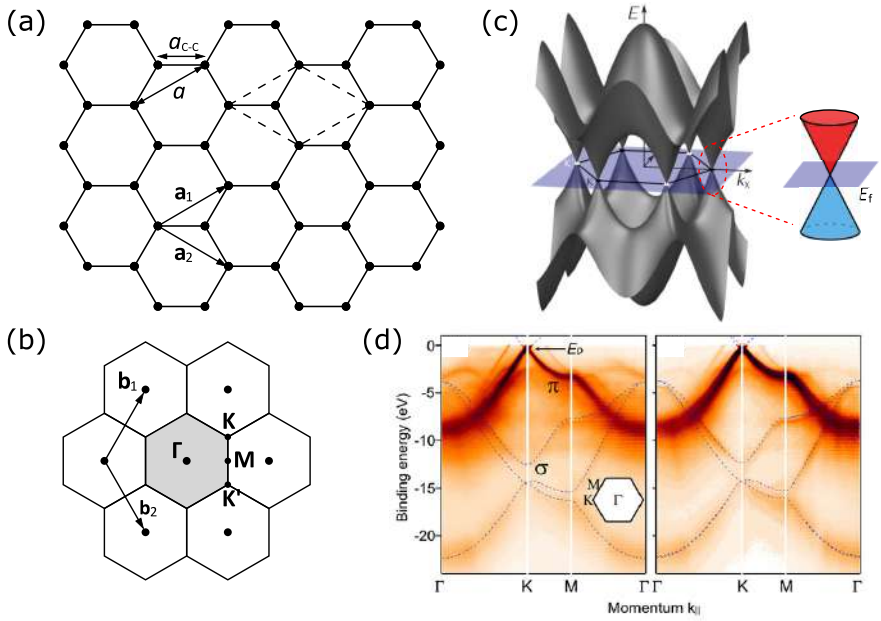

Fig. 1.2 The lattice structure and band structure of graphene. (a) Lattice structure of monolayer graphene. (b) Brillouin zone of graphene. (c) Band structure and Dirac cone of graphene. (d) Band structure of graphene measured by angle-resolved photoemission spectroscopy (ARPES) [5].

The distinctive band structure is the origin of the graphene's exceptional properties. The band structures of monolayer graphene are shown in Figure 1.2c. The conduction and valence bands touch at the K-point (frequently called Dirac point), where there is a zero density of

states but no band gap. Thus, graphene shows a semimetallic (or zero-gap semiconductor) character. The band structure shows a linear dispersion at the Dirac point [5–7]. The linear dispersion has been confirmed up to approximately ± 0.6 eV by experimental spectroscopic measurements [6]. The effective mass is $m_{\text{eff}} = \hbar^2 / \left(\partial^2 E / \partial k^2\right)$, where E is the energy and k is the wave vector. The electrons near the Dirac point behave as massless Dirac fermions ($m_{\text{eff}} \to 0$), governed by an equivalent massless Dirac equation which is of significant interest for condensed matter physics [4, 8, 9].

Graphene exhibits exceptional electrical conductivity, allowing electrons to move through it with minimal resistance The remarkable carrier mobility at room temperature has been reported in both suspended and SiO_2 supported graphene (~ 15000 cm^2/V$\cdot$s) [10]. The mobilities of electrons and holes are nearly identical [2]. The resistivity of graphene sheets is much less than the resistivity of silver, the lowest known at room temperature. The high mobility and lower resistivity make graphene nearly ideal for high-speed electronics.

Graphene is highly thermally conductive, with conductivity values up to 5000 W/m·K [11, 12], making it excellent for heat dissipation applications in electronics and materials science. Graphene is also one of the strongest known materials, with a Young's modulus of 1 TPa and a tensile strength of around 130 GPa [13, 14], which is 200 times stronger than steel by weight. The graphene layer is extremely flexible and stretchable for bending and tensile without breaking. The light absorbance of monolayer graphene is about 2.3% [15, 16]. The absorption spectrum is broadband, covering ultraviolet, visible, infrared, and even terahertz regions [15, 17]. This is due to its linear energy dispersion, which allows electron transitions across a wide range of photon energies without the restriction of the band gap.

Graphene has a very high surface area (~ 2630 m^2/g for single-layer graphene), making it useful for adsorption processes. Its surface area also enhances its chemical reactivity for functionalization. Although the basal plane of pristine graphene is relatively inert, the edges and defects within graphene sheets are chemically active. Functionalization, such as oxidation to form graphene oxide (GO), makes graphene more versatile and enhances its compatibility with other materials [18]. Pristine graphene is generally hydrophobic. Oxidation or other chemical modifications can alter its interaction with water, making it more hydrophilic and enabling it to disperse better in aqueous solutions.

1.2.2 Preparation methods of graphene

To explore and harness the unique properties of graphene, the synthesis process plays a crucial role. The quality and potential applications of graphene are directly influenced by the synthesis method, as each approach results in distinct structural and electronic characteristics. This section discusses several key graphene synthesis techniques, including mechanical

exfoliation, chemical vapor deposition, the oxidation-reduction process, epitaxial growth, and other emerging methods. Each method offers specific advantages and limitations, balancing factors such as production cost, quality, and scalability. Refining these techniques and developing hybrid methods will be essential for unlocking graphene's full potential in commercial applications.

Mechanical Exfoliation: Mechanical exfoliation, also known as the "Scotch tape method," was the first approach used to isolate single-layer graphene. In 2004, Andre Geim and Konstantin Novoselov first realized the isolation process [2]. This discovery earned them the Nobel Prize in Physics in 2010. This simple, yet effective method involves peeling layers of graphene from graphite using adhesive tape until single-layer graphene sheets are obtained. Mechanical exfoliation produces high-quality, defect-free graphene with pristine electronic properties, making it ideal for fundamental research [19]. However, this approach has limitations in scalability and reproducibility, restricting its application for large-scale production.

Chemical Vapor Deposition: Chemical Vapor Deposition (CVD) is one of the most widely used techniques for synthesizing large-area graphene on metal substrates, such as copper, nickel, and their alloy [20–22]. In this process, hydrocarbon gases are decomposed at high temperatures in a chamber, allowing carbon atoms to deposit and form graphene on the metal surface. Copper tends to promote monolayer graphene growth due to its low carbon solubility, while nickel can yield multilayer graphene. The candidates for hydrocarbon gas include methane, ethylene, and ethanol. CVD is highly scalable and produces continuous graphene films with few defects, making it suitable for industrial applications like transparent conductive films and flexible electronics. Transferring graphene from the metal substrate to an insulating substrate is a complex process that can degrade quality by introducing residue dopants, defects, and cracks.

Oxidation-Reduction of Graphite: The oxidation-reduction process involves the chemical oxidation of graphite to produce GO, which is then reduced to graphene by chemical or thermal treatments [23]. This method enables bulk production of graphene materials with high yield, making it suitable for applications where cost-effective production is a priority. However, graphene produced through this route tends to have residual oxygen groups and structural defects, which can compromise its electrical conductivity. Modified reduction techniques, such as hydrothermal reduction or electrochemical reduction, are being explored to improve the quality of reduced graphene oxide (rGO) [24].

Epitaxial Growth: Epitaxial growth is a promising method for producing high-quality graphene directly on an insulating substrate [25]. In this process, silicon carbide (SiC) is heated to high temperatures, causing the silicon atoms to sublimate and leaving behind a

carbon-rich surface that reorganizes into a graphene structure. This method yields high-purity graphene layers with controlled thickness and is particularly suitable for electronic applications, as it avoids the transfer step required in CVD. However, the cost of SiC substrates and the high temperatures required make this process less economically viable for mass production.

Other Emerging Methods: Other methods, such as liquid-phase exfoliation, laser direct writing, and molecular assembly. Liquid-phase exfoliation is a scalable method to produce graphene by dispersing graphite in a solvent and applying ultrasonication or shear force to separate graphene layers. It is cost-effective and suitable for large-scale production, yielding graphene in the form of flakes with applications in coatings, composites, and inks. Laser direct writing (LDW) is an efficient and versatile method for fabricating graphene by locally converting carbon-based precursors, such as polyimide (PI) or GO, into graphene using a focused laser beam. The laser induces rapid thermal or photochemical reactions, reducing GO or carbonizing PI to form graphene [26–29]. This mask-free process enables high-precision patterning and is flexible, cost-effective, and compatible with various substrates. LDW has shown great potential for applications in graphene-based sensors, electronic devices, and flexible circuits. Molecular assembly is a bottom-up synthesis method for precise control over graphene's structure at the atomic level. Common molecular precursors used in this method include small organic molecules, such as pyrene derivatives. It can be used for the synthesis of graphene nanoribbons, enabling precise control over the structure with designated widths and edges.

1.2.3 Application of graphene

The applications of graphene can be typically divided into two major categories: applications based on 2D single-layer or few-layer graphene sheets, and those based on three-dimensional (3D) graphene architectures such as aerogels and foams. This part outlines the distinct advantages and uses of each form, highlighting their contributions to fields such as electronics, energy storage, environmental engineering, and biomedical applications.

Applications of 2D Graphene Sheets

Single-layer or few-layer graphene sheets are highly suitable for applications in electronics, optoelectronics, and sensors. Due to its exceptional electrical conductivity and transparency, graphene is extensively studied as a material for transparent conductive films in touchscreens, organic light-emitting diode displays, and solar cells.

Graphene's broadband optical absorption, high carrier mobility, and ultrafast response time make it remarkably suitable for applications in photonics and optoelectronics. Its ultra-wideband absorption and exceptional carrier mobility make graphene an excellent candidate for photodetectors. It can replace the existing IV and III–V semiconductors which suffer from the "long-wavelength limit" and response delay. Graphene's ability to absorb light across a broad spectrum, from ultraviolet to terahertz, enables photodetectors to operate over a significantly wider wavelength range [30]. Both experimental and theoretical studies have extensively explored graphene's photoelectrical response, demonstrating much broader spectral detection capabilities [31]. Other optoelectronics devices such as modulators, filters, and terahertz generators are also reported.

Additionally, graphene's high carrier mobility makes it a promising material for next-generation field-effect transistors (FETs), offering the potential for faster and more efficient electronic devices. However, its zero band gap has historically hindered the real application. Recent breakthroughs, such as band gap engineering achieved through epitaxial growth on SiC, offer promising pathways to overcome this limitation [32].

Graphene's atomic thinness and high surface-to-volume ratio allow it to detect minute changes in its environment, leading to sensitive applications in chemical and biological sensing [33–36]. Graphene-based sensors exhibit exceptional sensitivity in detecting small gas molecules, heavy metals, pH levels, and biomolecules, which supports the trend toward lightweight, fast-response sensors in environmental monitoring and medical diagnostics.

Applications of 3D Graphene Aerogels and Foams

3D graphene architectures, such as aerogels and foams, expand graphene's application potential by adding structural complexity and porosity, which enables unique functionalities in energy, environmental, and biomedical fields.

The high porosity and surface area of 3D graphene aerogels make them excellent materials for adsorption and filtration. They are effective in removing heavy metals, dyes, and organic pollutants from water. Additionally, graphene foams are being explored in air purification and oil spill remediation, as they can efficiently adsorb oil and other contaminants [37].

The excellent conductivity of graphene improves charge transport. The 3D architecture with a large specific surface area of foam structure has higher charge storage, which enhances energy storage performance. These features are highly beneficial in supercapacitors, lithium-sulfur batteries, and fuel cells [26, 38]. Graphene-based electrodes enhance the energy density and cycling stability of lithium-ion batteries and provide high power density in supercapacitors. In fuel cells, graphene foams are used as catalyst supports, where their high

conductivity and surface area improve catalytic activity. The 3D graphene architectures have applications in portable electronics and electric vehicles.

The lightweight and resilient nature of graphene aerogels and foams make them suitable for applications where strength, flexibility, and low weight are required, such as in aerospace and structural composites. The open-cell structure of graphene foams also has the potential for heat dissipation and thermal management for high-performance devices [39, 40]. The high conductivity extent the application of flexible strain sensors [41–44].

1.2.4 Other two-dimensional materials

By replacing the carbon atoms in graphene's hexagonal structure with different atoms, a series of low-dimensional materials can be obtained. These materials also exhibit unique properties and have broad application potential. In this dissertation, the dry transfer method is also applied to the transfer and stacking of hBN and MoS_2 in collaboration with other researchers. Therefore, a brief introduction to hBN and MoS_2 is provided here.

Hexagonal boron nitride

Similar to graphene, hBN is a two-dimensional material with a hexagonal honeycomb structure. In hBN, the boron and nitrogen atoms are alternatively arranged with a bond length of 1.45 Å and intelayer spacing of $\sim$ 3.3 Å. The hBN is also known as "white graphene" due to its similar structure and properties with graphene.

Properties: The hBN exhibits a range of unique physical and chemical properties that distinguish it from other two-dimensional materials [45]. The hBN is an electrical insulator with an wide bandgap of approximately 5.9 eV [46, 47]. The hBN exhibits an optically transparent material with low absorption in the 250–900 nm wavelength range, yet an exceptionally high absorption peak in the deep ultraviolet (UV) range (200–220 nm) due to its anisotropic structure is observed. Despite a insulator, the hBN also has relatively high thermal conductivity up to 600 W/m·K. The Young's modulus of hBN can reach up to 1.16 TPa according to experimental measurement and theoretical analysis. The hBN has thermal stability up to high temperatures (1000 °C) and is chemically inert to most chemicals.

Synthesis: The hBN single crystal with best quality is synthesis by the high pressure high temperature (HPHT) method. Kenji Watanabe and Takashi Taniguchi developed such method. Their single crystal hBN has become the best choice for the scientific research of low-dimensional material [48, 49].

The mechanical exfoliation and CVD are also the common methods for hBN fabrication. Similar to graphene, single and few layers of hBN can be obtained by mechanical exfoliation

from bulk hBN crystals. This method produces high-quality flakes for research purpose, but it is limited by scalability. The hBN of Watanabe and Taniguchi is good candidate for mechanical exfoliation. CVD is also widely used for synthesizing high-quality, large-area hBN films [50, 51]. This method involves the decomposition of boron- and nitrogen-containing precursors, such as ammonia borane and borazine, at high temperatures, resulting in the formation of atomically thin hBN layers on metal substrates. The CVD method is widely used for creating hBN films suitable for electronic applications.

Applications: The wide-bandgap semi-conductivity of hBN leads to applications in deep UV to near infrared (NIR) emitters and detectors [52]. Kubota *et al.* reported the emission of intense 215 nm luminescence at room temperature in synthesized high purity hBN crystals [49]. Deng *et al.* fabricated UV light-emitting diodes using n-ZnO films on top of p-hBN/pGaN/sapphire substrate measuring a peak wavelength of $\approx$ 376 nm with a narrow full-width at half-maximum [53]. The combination of wide bandgap and presence of defects vacancies can create stable mid gap states resulting in highly efficient single-photon emitters. A ultra-broad spectral range (357–896 nm) single photon emission is observed using hBN with photostability and high brightness under ambient conditions [54].

The hBN is also beneficial in enhancing the device performance for other low-dimensional materials [55, 56]. The smooth and chemically inert surface has high optical surface phonon energy, and free of dangling bonds and charge traps, due to the strong in-plane bonding of the hexagonal lattice structure [57]. The hBN shows appealingly large bandgap and small lattice mismatch with graphene. By placing graphene on the hBN surface or sandwiching between two flakes, an increased carrier mobility is observed. Dean *et al.* fabricated high-quality mechanically exfoliated mono- and bilayer graphene devices on single-crystal hBN substrates, which demonstrated mobilities and carrier inhomogeneities that are almost an order of magnitude higher than devices on SiO_2 [55]. Wang *et al.* reported heterostructures made of graphene devices encapsulated by two hBN sheets [56]. Such encapsulation enabled high electronic performance, such as low-temperature ballistic transport over distances longer than 15 μm, and room-temperature mobility comparable to the theoretical phonon-scattering limit. Additionally, Dean *et al.* reported a similar device construct with hBN integrated in both the substrate and gate dielectric, which demonstrated significant improvements in quantum Hall measurements. Cui *et al.* demonstrated a van der Waals heterostructure device platform in which an atomically thin MoS_2 layer is encapsulated by hBN [58]. By dramatically reducing the interfacial impurities, intrinsic electron–phonon scattering is observed at high temperature, while substantially improved mobility is achieved at low temperature. The hBN can also work as barrier and spacer between two different 2D materials owing to its dielectric properties which result in tunneling effect and giving rise to new interfacial phenomena [59].

The graphene/hBN/graphene sandwich configurations have been employed in tunneling FET, in which h-BN serves as an insulating barrier for vertical tunneling electrons.

Molybdenum disulfide

The TMDCs are a family of layered materials composed in the form of MX_2,where M is transition metals (e.g., molybdenum, tungsten) bonded with chalcogen atoms X (e.g., sulfur, selenium). Each layer consists of a sandwiched structure where the transition metal atoms binds with the surrounding chalcogen atoms with covalent bonds. Among TMDCs, molybdenum disulfide (MoS_2) has gathered significant attention, particularly for its semiconducting nature in monolayer form.

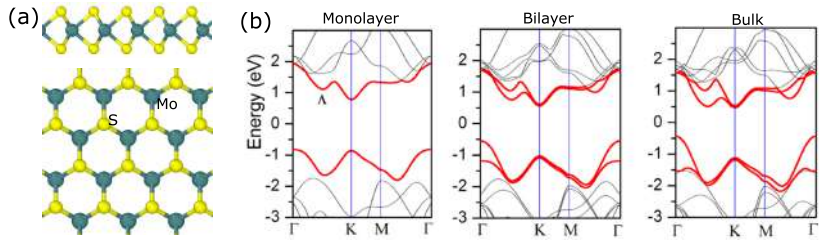

Fig. 1.3 (a) Lattice structure of MoS_2. (b) Band structures of monolayer, bilayer, and bulk MoS_2 [60].

Properties: Monolayer MoS_2 has a direct bandgap of approximately 1.8 eV, while bulk MoS_2 has an indirect bandgap of about 1.2 eV [61, 60]. This tunable bandgap with thickness is advantageous for optoelectronic applications [62, 63]. Similar to graphene, a mechanical flexibility also appears in MoS_2 with a Young's modulus of 270–330 GPa for different layer numbers according to experimental measurements.

Synthesis: Mechanical exfoliation is popular laboratory methods for obtaining monolayer or few-layer MoS_2 flakes. Mechanical exfoliation produces high-quality samples suitable for research. The CVD method is also widely used to produce high-quality, large-area MoS_2 films by decomposing molybdenum and sulfur precursors on substrates at high temperatures. This method allows for precise control over thickness and quality, making it suitable for electronic applications.

Applications Due to its unique properties, MoS_2 is applied across a variety of fields. The direct bandgap of MoS_2's in monolayer form makes it suitable for transistors, photodetectors, logic circuits, and flash memory devices [64, 65]. Its flexibility and tunable electronic properties are advantageous for next-generation electronics, including flexible displays and wearable devices.

1.3 Introduction of nanospacer materials

1.3.1 Introduction of carbon nanotubes

The CNTs are cylindrical nanostructures composed of carbon atoms arranged in a hexagonal lattice, similar to the structure of graphene but rolled into tubes. Their unique properties, which include exceptional strength, electrical conductivity, and thermal stability, have made them central to advancements in nanotechnology, electronics, and materials science.

The discovery of carbon nanotubes can be traced back to the late 20th century, with significant advancements in the 1990s. In 1991, Japanese scientist Sumio Iijima first observed multi-walled carbon nanotubes (MWCNTs) using transmission electron microscopy (TEM) while studying carbon materials produced in an electric arc discharge [1]. This breakthrough paved the way for further research into single-walled carbon nanotubes (SWCNTs), which were identified shortly after and exhibit unique properties distinct from their multi-walled counterparts. The discovery of CNTs marked a significant milestone in nanotechnology, as their properties opened up new possibilities for applications across various fields.

Properties of Carbon Nanotubes

CNTs are characterized by remarkable physical and chemical properties, which can be divided into the following categories:

Physical Properties: CNTs are known for their exceptional tensile strength, which is several times greater than that of steel, and high elasticity, which enables them to withstand extreme mechanical stress without breaking. Their high thermal conductivity is comparable to diamond, making them excellent materials for thermal management applications. Additionally, CNTs exhibit unique electrical properties that depend on their structure. While SWCNTs can be either metallic or semiconducting based on their chirality, MWCNTs generally conduct electricity due to the overlap of electronic bands across layers.

Chemical Properties: Chemically, CNTs are relatively inert due to the strong carbon-carbon bonds in their structure, which makes them resistant to most acids and bases. However, they can be functionalized through chemical modifications, such as oxidation or the addition of functional groups, to enhance their solubility and compatibility with other materials. This chemical inertness, combined with functionalization capabilities, has expanded the applicability of CNTs in composite materials, sensors, and biomedical devices.

Synthesis of Carbon Nanotubes

The arc discharge is the method used for the initial discovery of CNTs [1]. It involves creating an electric arc between graphite electrodes in an inert gas atmosphere. This high-temperature process vaporizes carbon atoms, which then condense to form CNTs. While efficient for producing high-quality CNTs, this method is less scalable and results in a mixture of CNTs with varying diameters and layers.

The CVD method is the most commonly used technique for large-scale CNT production. In this process, a carbon-containing gas (like methane or acetylene) is introduced into a chamber containing a catalyst substrate at high temperatures. The carbon atoms decompose on the catalyst surface and form CNTs. CVD is valued for its scalability and control over CNT structure, making it suitable for both SWCNTs and MWCNTs.

Applications of Carbon Nanotubes

The exceptional properties of CNTs have led to numerous applications across various fields:

Electronics: Due to their unique electrical properties, CNTs are considered for use in transistors, sensors, and flexible electronics. Their high conductivity and stability also make them ideal candidates for conductive films and transparent electrodes in displays and solar cells.

Energy Storage: CNTs are widely used in energy storage devices, such as batteries and supercapacitors, due to their high surface area and conductivity. Their role in electrode materials enhances energy density, charge rate, and cycle life, making them valuable in next-generation energy devices.

Composites and Structural Materials: CNTs are often integrated into polymers, metals, and ceramics to create lightweight, high-strength composites. These composites are used in aerospace, automotive, and sports equipment industries, where strength-to-weight ratio is crucial. The incorporation of CNTs enhances the mechanical properties, thermal stability, and durability of the composite materials.

Biomedical Applications: Functionalized CNTs are used in drug delivery, tissue engineering, and biosensors. Their ability to cross cell membranes and bind to biological molecules allows them to target specific cells, making them promising for targeted drug delivery and imaging. CNTs are also being investigated for use in neural interfaces and biocompatible scaffolds.

Environmental Engineering: CNTs' high surface area and functionalizability make them useful in water filtration and environmental remediation. They are effective at adsorbing con-

taminants and heavy metals from water, and CNT-based membranes are under development for desalination and air purification.

Carbon nanotubes, since their discovery, have revolutionized nanomaterials science. With remarkable mechanical strength, electrical conductivity, and chemical versatility, CNTs are integral to advancements in electronics, energy storage, composite materials, and biomedicine. Their synthesis methods, particularly CVD, enable scalable production for industrial applications, further driving innovation. As research continues, CNTs are expected to play an increasingly prominent role in developing advanced materials and solutions across diverse scientific and engineering fields.

1.3.2 Introduction of nanodiamonds

Similar to graphene and CNT, nanodiamonds (NDs) are another kind of nano-carbon allotrope. The ND particle also has a diamond-like lattice structure but with a size in the nanometer range. The diameter of NDs are typically 2–20 nm, although aggregation can lead to larger particles. The NDs share certain properties with bulk diamond, including hardness, optical transparency, thermal conductivity, and chemical inertness. The NDs is thermal stability up to 800 °C. Higher temperature will make surface carbon turns to sp^2 carbon-onion structure [66]. NDs exhibit unique characteristics due to their nanoscale dimensions and high surface-to-volume ratio. The large surface area, with defects and functional groups (like carboxyl, hydroxyl, and carbonyl groups), significantly impact their chemical reactivity, solubility, and dispersibility in various solvents. This surface functionality enables customization, making NDs versatile across different applications.

Synthesis: NDs are generally produced via high-energy processes, which allow for the formation of the diamond lattice at nanoscale dimensions.

The detonation method is widely used for its scalability and cost-effectiveness. The detonation nanodiamonds (DNDs) is also known as ultradispersed diamond (UDD). In this method, nanodiamonds are formed from the detonation of carbon-containing explosives (usually a mixture of TNT and RDX) in an oxygen-deficient chamber. The rapid pressure and temperature rise facilitate the transition of carbon to the diamond phase, resulting in nanoscale particles. The DNDs are usually aggregated and require post-synthesis purification to remove impurities and improve dispersibility [67–69].

High-Pressure High-Temperature (HPHT) method involves subjecting graphite or other carbon precursors to extreme pressures ($\sim$5 GPa) and temperatures ($\sim$ 1200°C). The controlled environment allows for the direct formation of NDs with higher purity and uniformity than those from detonation synthesis. HPHT synthesis can also incorporate the desired

doping elements to achieve specific properties. Additional methods such as microwave plasma chemical vapor deposition (CVD) are also reported.

Applications Nanodiamonds have found applications across a range of fields due to their unique combination of mechanical, thermal, and surface properties.

NDs have wide biomedical applications due to their biocompatibility and functionalizability including the drug delivery, bio-imaging, and tissue engineering. The surface of NDs can be modified to carry therapeutic molecules, allowing for controlled release and targeting. In addition, their optical properties enable NDs to serve as contrast agents in imaging techniques, while their low cytotoxicity enhances their suitability in biomedical applications.

NDs show extensive application in electronics and opto-electronics such as single photon source and electron emitting element. NDs are also being studied for the application in quantum computing due to their stable quantum states at room temperature. The hardness and low friction coefficient of NDs also make them effective additives in lubricants, where they reduce wear and friction between metal surfaces.

1.4 Previous research on graphene property modulation

1.4.1 Twisted multilayer graphene

In mulitilayer graphene, the AB stacking (Bernal stacking) always appears due to the fact that it is the most energy stable structure. The band structure becomes parabolic, which is different from the linear dispersion of monolayer graphene. By twisting the stacking order between adjacent layers, the change of atom arrangement cause the decrease of interlayer interaction in multilayer graphene. The twist mulilayer graphene, *i.e.* turbostratic graphene, has a band structure similar to the monolayer graphene with linear dispersion. The interlayer distance is also slightly different from the AB stacking. The twisted stacking also leads to the moiré pattern which is the origin of tremendous novel physical phenomena. The previous research reported the twisted stacked Gr to realize the monolayer band structure. However, twisted stacked Gr still has domains with AB and AA stacking [70].

1.4.2 Graphene intercalation

Intercalation is another widely reported method to modify the interlayer interaction with increased distance [71–77]. Metal atoms (Li and K) or small inorganic compound dimer ($MoCl_5$ and $AlCl_3$) are introduced between Gr layers by vapor deposition. The interlayer distance is increased, and the interlayer coupling is weakened. The density functional theory

calculations have predicted that double graphene with intercalation of $FeCl_3$ has a band structure resembles the monolayer Gr with linear dispersion [71, 72]. The decreased sheet resistance has been observed in multilayer graphene with intercalation of $FeCl_3$ [73] and $AlCl_3 - CuCl_2$ [77]. The charge transfer between the intercalation material and graphene layers induce doping effect [71, 75]. Novel physical behavior such as the quantum Shubnikov-de Haas oscillation are reported where the electrical conductivity changes periodically with the magnetic field [72].

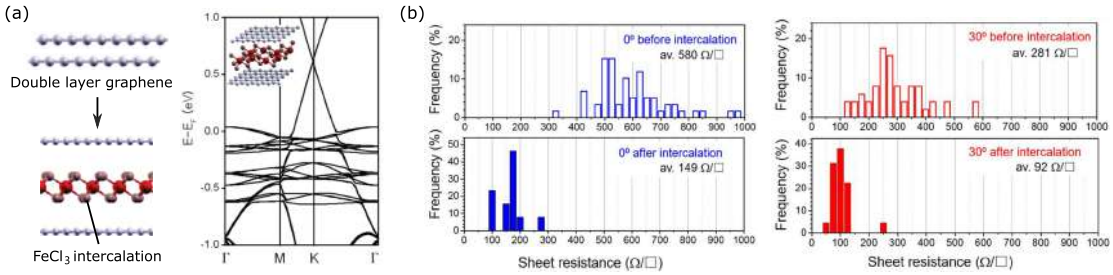

Fig. 1.4 Intercalation of multilayer graphene. (a) Schematic and band structure of $FeCl_3$ intercalation graphene. (b) The decrease of electrical conductivity in multilayer graphene before and after intercalation.

There are many limitations in the intercalation method. The alternative material is limited to metal atoms, ions, and inorganic compounds with small particles size. In the intercalation process, the multilayer graphene is first prepared and placed in vacuum chamber [77]. Then, the gas phase intercalation materials are introduced in the chamber by heating. The atoms or molecules will spontaneously insert into the graphene layers. The interlayer distance of AB stacking graphene is 0.34 nm, which makes large molecules hard to insert. Thus, the separation of interlayer distance is usually less than 1 nm [75–77]. The intercalation quality is not uniform. Araki *et. al.* has reported that the intercalation rate is sensitive to the stacking angle [77]. The intercalation is easier to happen in stacked Gr layers with a large twist angle [75, 77]. The chloride molecules and metal elements could induce doping on graphene layers [72]. A reaction condition is required with vacuum and heating for a relatively long time which cost energy [73, 75].

1.4.3 Graphene hybrid systems with other nanomaterials

The hybridization of graphene with nanomaterials such as CNTs has emerged as an effective strategy to reduce interlayer interactions, thereby enhancing the properties of graphene-based systems. Graphene, renowned for its atomic thickness, exceptional electrical and thermal conductivity, and remarkable mechanical stiffness, faces challenges such as layer

re-stacking, which limits its functional potential[40]. Incorporating CNTs into graphene structures addresses this issue by introducing a cross-linking effect that prevents re-stacking and increases porosity. This integration significantly improves mechanical robustness, electrical properties, and superelastic characteristics, broadening the applicability of graphene-CNT (Gr-CNT) hybrid systems [41, 78, 40].

Gr-CNT hybrids have demonstrated exceptional performance in various applications. Their porous structure and high surface area make them ideal as scaffolds and adsorbents for catalytic processes and water treatment [21, 37]. Additionally, the excellent thermal and electrical conductivity of these hybrids makes them suitable for use in supercapacitors [79], batteries [80], and thermal management systems [39]. The lightweight and flexible nature of Gr-CNT hybrids further enables their use in strain sensors, artificial muscles, and vibration dampers [43, 81].

Despite these advancements, most experimental methods for fabricating Gr-CNT composites rely on random mixing of liquid phases, which limits the control over layer numbers and uniform CNT insertion between graphene layers [82, 83]. This necessitates the development of new fabrication approaches with enhanced structural controllability. Theoretical and simulation studies have investigated the mechanical properties of Gr-CNT structures, including elastic constants and CNT deformation within graphene layers [84, 85]. However, systematic studies on critical factors such as the size and distribution of CNTs, which govern the microstructure and functionality of these hybrids, remain insufficient. Addressing these gaps could further advance the design and application of Gr-CNT systems and extend the research to other graphene-based hybrids with nanomaterials like hBN and boron nitride nanotube.

1.5 Motivation and challenges

In this dissertation, I proposed an alternative strategy to regulate interlayer interactions. The two nano carbon allotropes, carbon nanotubes and nanodiamond, are selected as the candidate of nanospacer.

Previous studies report randomly stacked graphene also exhibits a linear dispersion band structure. However, AB-stacked subdomains still exist within the moiré patterns of the stacked layers. Growing large-scale randomly stacked graphene through the CVD method remains a significant challenge. Intercalation is another approach to weakening interlayer interactions, but the range of materials that can be intercalated is typically limited to small molecules or metal atoms. The introduction of other elements may lead to doping effects and other alterations.

By introducing nanospacers between graphene layers, the interlayer spacing is increased. Density functional theory (DFT) simulations were conducted, and the figure shows the band structures of monolayer graphene, AB-stacked bilayer graphene, and AB-stacked graphene with an interlayer spacing of 5 Å. Increasing the interlayer spacing enables bilayer graphene to achieve a band structure with linear dispersion, similar to that of monolayer graphene. As a result, each layer in multilayer graphene exhibits properties comparable to monolayer graphene. Due to van der Waals forces, there is an attractive interaction between

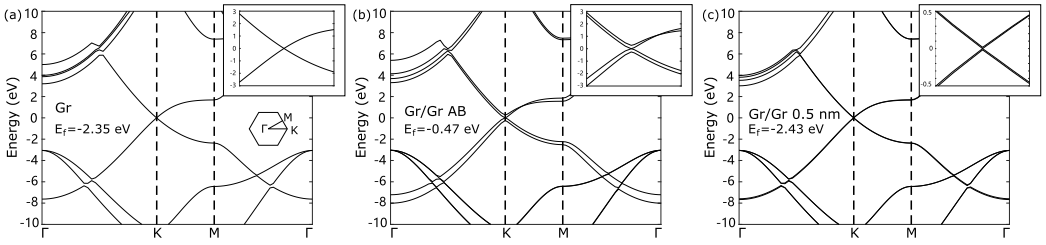

Fig. 1.5 Band structures of graphene layers from density functional theory. (a) Monolayer graphene. (b) AB-stacked double-layer graphene. (c) AB-stacked double-layer graphene with interlayer separation of 0.5 nm.

graphene layers. After introducing spacers, this attraction can cause graphene to bend and deform, bringing the interlayer distance closer again. Therefore, it is necessary to analyze the microscopic structure of the graphene and spacer stacking to ensure that the graphene layers are adequately separated.

The porous structure of graphene foam is a key factor contributing to its wide range of applications. Adding spacers can increase the surface ratio of graphene foam. Previous studies have reported experimental investigations into the effects of incorporating CNTs on the interlayer properties of graphene. However, research on the characterization of nanoscale structures and theoretical aspects remains limited. Gr-CNT composite foams are often used in strain sensors, but mechanical studies from the perspective of their microscopic structure are still insufficiently developed. Therefore, the mechanism of deformation behavior should be further studied.

1.6 Organization of the dissertation

The organization of this dissertation is the following:

In Chapter 1, I first introduced the graphene and the nanospacer materials, CNT and ND, from their properties to synthesis methods and applications. Then, I reviewed the previous methods for modulating graphene properties, with a particular focus on interlayer interaction

modulation. Finally, I proposed my strategy for modulating graphene interlayer interactions and discussed the motivation for constructing graphene stacking structures with nanospacer insertion.

In Chapter 2, the research methods are introduced. The sample preparation methods include two transfer methods, dry and wet transfer, for graphene stacking and the method for dispersion nanospacers between graphene layers. The characterization methods involve Raman spectrum and atomic force microscope (AFM). The microstructures of the stacking structures are also simulated by molecular dynamics (MD). The simulation method is briefly introduced with basic knowledge.

In Chapter 3, the insertion of CNT nanospacers into multilayer graphene is investigated. The Gr-CNT stacking structure is experimentally fabricated with the dry transfer method. Raman spectroscopy and AFM observation confirm the increase in interlayer distance and the reduction in interlayer interaction. The MD simulations are conducted to explore the microstructure of the Gr-CNT stacking structure, revealing two distinct interlayer configurations: separation and adhesion. The effect of CNT diameter, inter-tube distance, and arrangement style are systematically studied.

In Chapter 4, the NDs are employed as nanospacers for interlayer modulation. Both experimental fabrication and MD simulation demonstrate the separation of graphene layers and the suppression of interlayer interactions. Additionally, a theoretical model based on continuum mechanics is developed which enables the prediction of the relationship between ND parameters and the equilibrium configuration with reduced simulation time. The model also allows for the calculation of the critical inter-ND distance required for graphene layer separation.

In Chapter 5, the property modulations of CNT and ND spacers are systematically studied. First, additional MD simulations are performed to pursue deeper insights into the microscopic configurations of Gr-CNT stacking structures. Factors such as the number of CNT walls, applied loading pressure, and multilayer suspended configurations are investigated. The structure shows a multistable characteristic between the separation and adhesion configuration, which induces hysteresis loading-unloading curves. Second, a non-linear I-V curve is observed in the graphene-ND stacking system fabricated using the dry transfer method. The nonlinearity arises from the tunneling current through the ND spacers, demonstrating potential applications in physical neural network devices.

In Chapter 6, I recapitulate the major conclusions of this dissertation and provide a future perspective with further novel properties remaining unexplored and potential applications.

Chapter 2

Research methods

2.1 Sample preparation

2.1.1 Wet transfer of 2-dimensional materials

The monolayer graphene is grown using the CVD method on copper foil. The graphene should be first transferred to silicon (SiO_2/Si) or fused quartz (FQ) substrate for easier further manipulation and measurement. The CVD graphene from three manufacturers are tried, NTT basic research laboratories, Graphene Platform, and Grolltex. Monolayer graphene grows on both sides of copper foil (Gr/Cu/Gr).

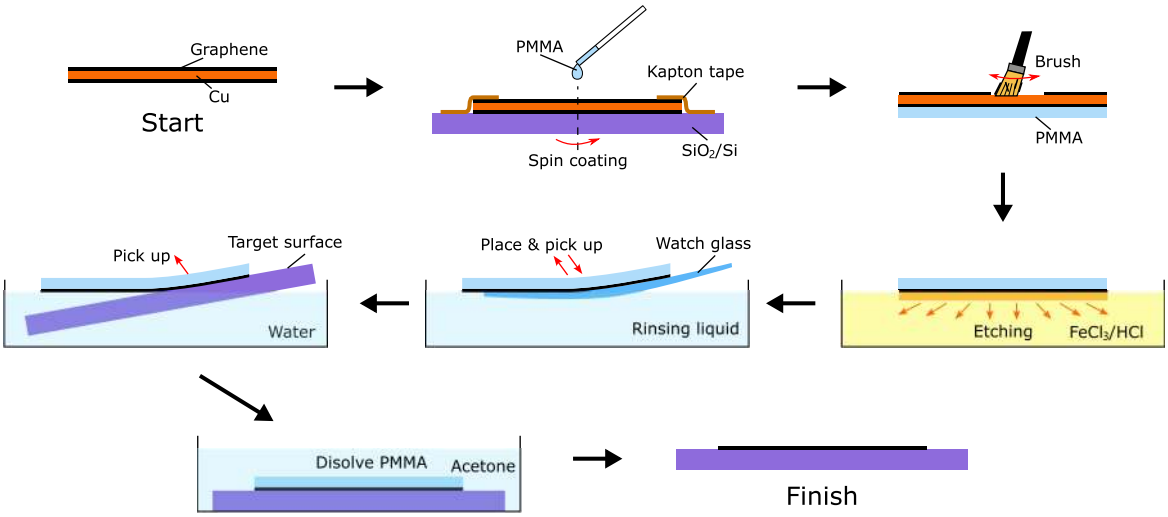

Fig. 2.1 The process of wet transfer from copper foil to silicon substrate.

The process of wet transfer from copper foil to silicon surface with 300 nm oxide layer is shown in Fig. 2.1 and details are described below:

1. **Cover one side of Gr/Cu/Gr with polymer:** Cut the Gr/Cu/Gr into small pieces (5−8 mm squares). Fix the four sides of Gr/Cu/Gr on the SiO_2/Si substrate with Kapton adhesive tape. Spin coating the Gr/Cu/Gr with polymethyl methacrylate (PMMA) and a spin rate of 2500 rpm for 50 s. The PMMA (950 PMMA A6, Kayaku Advanced Materials, Inc.) is dissolved in anisole at a concentration of 6 wt.%.

2. **Remove the graphene on the other side:** Prepare $FeCl_3$ solution by mixing 16 g $FeCl_3 \cdot 6H_2O$ powder and 90 ml deionized water. Gently brush the other side of the Gr/Cu/Gr with a brush dipped in $FeCl_3$ solution until the surface color turns dark. An alternative method is plasma etching with O_2 or Ar.

3. **Etching of copper foil:** Prepare the etching solution by mixing the concentrated HCl (36 %) and $FeCl_3$ solution in a 1:1 volume ratio in a petri dish. Place the PMMA/Gr/Cu on the surface of liquid. Place the petri dish in the fume hood and wait for 16 hours in the ambient condition. After the etching process, rinse the Gr/PMMA film in deionized water twice for 10 min, 9 % HCl for 2 h, and deionized water three times for 10 min. Use watch glass to transfer Gr/PMMA between different liquid surfaces.

4. **Pick up graphene film:** Treat the target surface using O_2 plasma cleaning (Low mode, 10 Pa, 40 s) to enhance the hydrophilicity. Pick up the Gr/PMMA file with the target substrate. Use a rubber dust blower and a needle tip to adjust the position of the graphene film to ensure it is at the center or needed place of the substrate. Place the sample onto 60 °C hotplate for 5 min to evaporate water.

5. **Remove PMMA layer:** After ensuring the water is fully drought, soak the sample into organic solvent in a Petri dish to remove the PMMA layer. The optional organic solvent includes acetone, 1-methyl-2-pyrrolidinone (NMP), and anisole. After soaking the sample, wait over 12 h for the dissolution. Heating the Petri dish on a 50 °C can accelerate the dissolution. Finally, wash the sample in acetone and 2-propanol (IPA) using a dropper, and blow away the remaining IPA with N_2 gun.

After wet transfer, PMMA residue may still remain. The sample can be further cleaned by H_2 annealing. The condition is 350 °C for 40 min, and the carrier gas is 150 sccm H_2/Ar (3%) with a total pressure of 8.6 kPa.

2.1.2 Dry transfer of 2-dimensional materials

The dry transfer is another method to move low-dimensional materials between different surfaces. The dry transfer system is shown in Fig. 2.2. The system consists of a microscope

for monitoring the position of material flakes, and two micrometer translation stages for adjusting the relative position (see Fig. 2.2a). One translation stage is for the sample substrate, placed beneath the microscope (see Fig. 2.2b). The stage can move in the horizontal x and y directions and rotate along the z-axis. A Peltier temperature controller is integrated into this stage to adjust the temperature. The other translation stage, designed for the movement of the polymer lens, is positioned beside the first stage. This stage can move in the horizontal x and y directions and along the z-axis with a stepper motor.

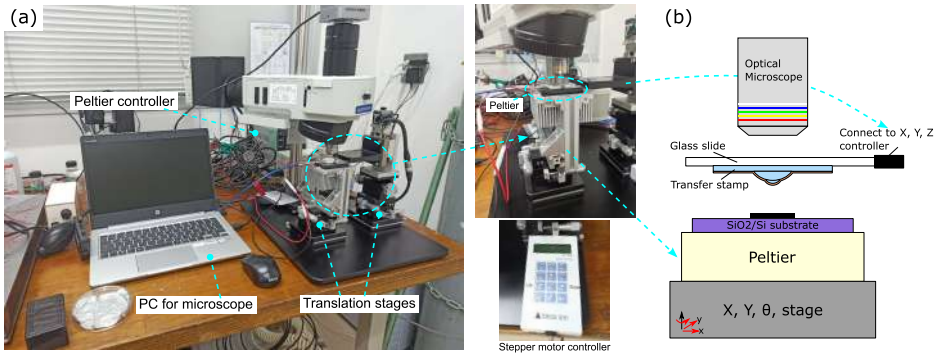

Fig. 2.2 (a) Dry transfer system for stacking low-dimensional material flakes. (b) Schematic diagram of the substrate and lens stages.

The polymer lens is the main tool for pickup and stacking materials. The fabrication process is as follows (see Fig. 2.3a):

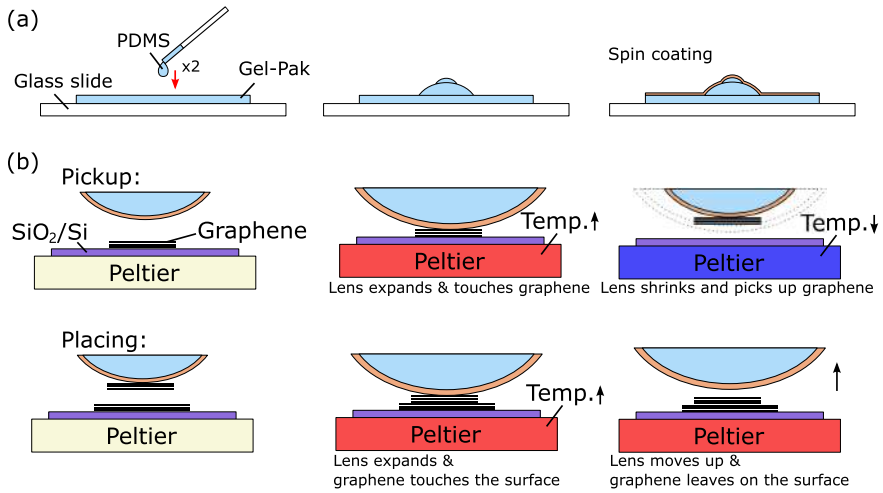

Fig. 2.3 (a) Fabrication process of dry transfer lens. (b) Process of dry transfer, pickup and placing.

1. **Polymer film:** Cut the glass slide into small pieces 11 mm $\times$ 9 mm. Clean the cut glass slide in ethanol and water once each in ultrasonic. Cut the Gel Pak silicone film

into 6 mm $\times$ 6 mm, remove the protective film on both sides and adhere it to the center of the cut glass slide.

2. **First polymer lens:** Prepare the polydimethylsiloxane (PDMS) mixture. Take 0.5 g of Dow Sylgard 184 base and 0.05 g of curing agent (mass ratio 10:1), mix, and stir thoroughly. Use a pipette tip to take a small amount of the mixture and drop it onto the surface of the silicone film. The droplet should be about 1–2 mm in diameter. Then, put the silicone film on a hotplate at 120 °C and heat for 10 min to cure the PDMS into a lens.

3. **Second polymer lens:** The size of the second lens is often smaller than that of the first lens. The lens size affects the contact area; a smaller lens only contacts the surrounding area of the target material flake, allowing precise pickup and stacking of the desired flake without affecting other parts. The small second lens is created with the help of the dry transfer stage. Place the film with the first lens on the Peltier stage, and fix a thin platinum wire ($\phi = 0.02$ mm) onto the motorized stage using a glass slide. Wet the tip of the platinum wire with liquid PDMS using a pipette to form a tiny droplet. Control the movement of the motorized stage to approach the lens surface. With the aid of a microscope, carefully drip the second droplet at the center of the first lens. Then, cure the PDMS droplet into the second lens with the same heating condition (120 °C, 10 min).

4. **Covering polymer spin-coating:** PDMS has low surface adhesion, so a more adhesive polymer covers it, such as poly(propylene carbonate) (PPC) or poly(methyl methacrylate) (PMMA). First, perform plasma treatment on the PDMS lens to enhance wettability; the treatment conditions are DC plasma (Fig. 2.4a), “Low" mode, with oxygen at 10 Pa for 1 min. Spin-coat a 15 w.t.% PPC anisole solution onto the treated lens surface, with parameters of 2000 rpm for 30 seconds. After spin-coating, heat on a hotplate at 75°C for 45 minutes to evaporate the solvent.

The pickup, placing, and stacking of low-dimensional material flakes are achieved through contact between the surface of the polymer lens and the flake. The dry transfer system (Fig. 2.2) allows precise control over the relative movement between the polymer lens and the material substrate, as well as the temperature of the substrate. The pickup and placing of the material are realized by adjusting the adhesive properties of the lens surface through temperature control. At higher temperatures (above the glass transition temperature), the surface polymer, such as PPC or PMMA, is in a viscoelastic state. The adhesion between the lens and the flake is weak, making it suitable for placing the material. Conversely, at lower

temperatures (below the glass transition temperature), the surface polymer is in a solid state. The lens and flake adhere strongly, making the lens effective for picking up the material.

The operation of the dry transfer is shown in Fig. 2.3b with detailed steps as below:

- **Pickup process:**

  1. Position the polymer lens carefully close to the target surface with the stepper motor and translation stage.
  2. Increase the temperature of the Peltier controller to the target value (e.g., $\sim 85°C$ for PPC polymer). Increasing temperature allows the lens to expand and make contact with the surface. Wait until the temperature stabilizes at the set value.
  3. Gradually lower the temperature to shrink the lens and pick up the flake. For mechanically exfoliated flakes, reduce the temperature to 10–15 °C. For CVD materials, reduce the temperature further to approximately 5 °C. Take care to avoid the formation of condensation on the surface at low temperatures.
  4. If the lens remains in contact with the sample surface after cooling, raise the lens using the stepper motor, ensuring the smallest step length is used.

- **Placing process:**

  1. Position the polymer lens near the target area using the stepper motor and translation stage. The position should be carefully confirmed for precise stacking.
  2. Increase the temperature of the Peltier controller to the target value, typically ~ 5 °C higher than the pickup temperature. Allow the lens to expand and make contact with the target area of the surface. Wait until the temperature stabilizes at the set value.
  3. Gradually raise the lens using the stepper motor, ensuring the smallest step length is applied. This process will reduce the contact area between the lens and the surface, leaving the flake to adhere to the surface.
  4. Reset the Peltier controller to room temperature and take the sample substrate. Residual polymer on the sample can be removed by washing with acetone for 10 minutes or through H_2 annealing.

2.1.3 Nanospacer dispersion

The dispersion of nanospacers was achieved using the spin-coating method. Since graphene is a hydrophobic material, selecting a solvent with suitable wettability is crucial to

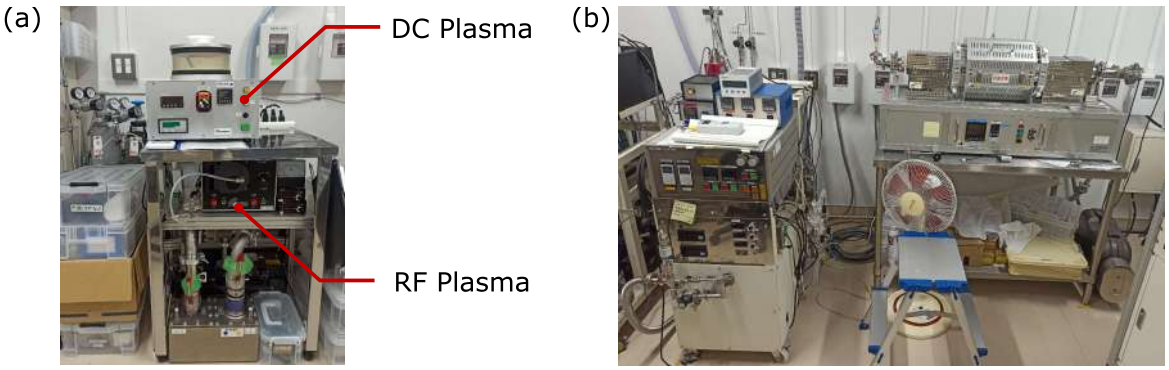

Fig. 2.4 Other experimental instruments. (a) Picture of DC plasma and RF plasma instruments. (b) Instrument for high temperature annealing process.

achieving a uniform dispersion. In this study, ethanol was used as the solvent for dispersing the nanospacers. Compared to water and NMP, ethanol has a lower surface tension, allowing the dispersion to spread more effectively and cover larger areas, thereby improving uniformity.

Before spin-coating, the nanospacer dispersion was sonicated in an ice-water bath for 60 min to minimize aggregation. The dispersion was then spin-coated onto the graphene surface at a speed of 3000 rpm for 180 s. After spin-coating, the sample was placed on a hot plate set to 90 °C for 3 minutes to ensure complete evaporation of the ethanol.

2.1.4 Reduced graphene oxide films with carbon nanotubes

By combining vacuum filtration and high-temperature reduction, reduced graphene oxide (rGO) films can be prepared. Introducing nanospacers into the suspension used for vacuum filtration allows the spacers to be inserted between graphene layers. The process consists of two steps. The first step makes graphene oxide (GO) film by vacuum filtration method. The second step reduces the GO to rGO by high temperature annealing. Compared to the layer-by-layer stacking of CVD graphene, this method enables the production of large-area multilayer graphene at a lower cost.

Here, the preparation process of the film is demonstrated using a GO-CNT stacking structure as an example.

Vacuum filtration method for GO film with nanospacer

1. First, aqueous suspensions of GO and CNT are mixed in a specific ratio (16:1). Shake the mixed solution on a shaker for 30 minutes to ensure thorough mixing. The CNT suspension used here has a concentration of 0.1 w.t.%, with an average tube diameter of 4 nm (ZEONANO 02DS-WA-RD). The GO suspension, prepared using

the modified Hummer's method, has a concentration of 0.1 w.t.% (provided by the Nishina Laboratory at Okayama University).

2. Take a filter membrane and fix it on the metal mesh of the filter flask. The filter membrane has a diameter of 25 mm (Merck).

3. Using a dropper, add the mixed suspension (approximately 10 drops) onto the filter membrane. Turn on the vacuum pump to reduce the pressure inside the flask. Under the pressure difference between inside and outside the filter flask, the suspension passes through the filter membrane, leaving GO and CNT on the surface of the membrane. Wait until the suspension is fully filtered. If frost appears on the surface of the membrane or if condensation forms on the outer wall of the filter flask, stop the vacuum filtration and allow the frost to melt before continuing. The frost can cause blockage and prevent the suspension from flowing downward. The solvent water beneath the filter membrane will evaporate under vacuum, removing heat from the upper liquid layer and causing frosting.

4. Once the initially added suspension is fully filtered, continue adding the same amount of suspension and wait for filtration. Repeat this process until all the prepared solution has been added and filtered.

5. Turn off the vacuum pump. Remove the filter membrane containing GO and CNT. Allow the dried filter membrane to be placed in 50°C acetone and heated for over 30 minutes until the white filter membrane is completely dissolved. Use a quartz substrate to collect the GO-CNT film and place it on a 50°C hotplate for drying.

High temperature reduction of GO

The GO films require high-temperature reduction using ethanol as the reducing agent. The high-temperature electrical furnace used for reduction is shown in Fig. 2.4b. In the reduction process, the flow rate of ethanol is 2 sccm, the flow rate of argon gas is 20 sccm, the reduction temperature is 1200°C, the reaction time is 1 hour, and the pressure is 0.3 Torr.

2.2 Measurement method

2.2.1 Raman spectrum

Raman spectra are used in our evaluation to analyze the crystallinity and layer number of the multilayer graphene grown by CVD method. The typical Raman spectra of monolayer

graphene is shown in Fig. 2.9. There are three characteristic peaks in this Raman spectra, from the left to the right are D band (1350 cm^{-1}), G band (1580 cm^{-1}) and 2D band (2700 cm^{-1}), respectively. The principles of Raman spectra in graphene can be understood by considering the origin of the different vibrational modes. Since graphene has two atoms in each unit cell, six phonon branches exist, including three acoustic (A) and three optical (O) phonons. Four of these phonons (two O and two A) are in-plane (i), and the other two phonons (one A and one O) are out-plane (o). If the vibration direction is perpendicular to or parallels with the carbon-carbon bonds, then the modes are classified as transversal (T) or longitudinal (L), respectively. The Raman bands of graphene are mainly due to the iLO and iTO vibration modes.

The G band is a first-order non-dispersive Raman scattering band, originated from the in-plane vibrations of sp^2 bonded carbon atoms in graphene. As shown in Fig. 2.5, by impinging the incident photon (blue arrow), an electron-hole pair is excited at the Γ-point of the first Brillouin zone. The electron-hole pair is scattered by the iTO or iLO phonons and recombines by emitting a photon (red arrow). The G band corresponds to the amount of graphene present.

The D-peak, the second-order dispersive Raman scattering is due to the breathing-like modes of six-atom rings as shown in Fig. 2.5. This band involves an iTO phonon around the K-point. In this case, the electron is inelastically scattered by an iTO phonon to the K′ point and then is elastically back-scattered to the K point by a defect for the momentum conservation. The D band appears in the presence of point defects or grain boundaries.

The G′ band, also known as 2D peak, is a second order Raman process originating from the in-plane breathing-like mode of the carbon rings like the D band. Fig. 2.5 shows a diagram of the Raman 2D process. Fig. 2.5 shows the double resonance process in which an electron–hole pair is created by an incident photon near the K point. The electron is inelastically scattered by a iTO phonon to the K′ point. Since the Raman process must conserve energy and momentum, the electron must scatter back to K before recombining with the hole. In the case of the G′ band the electron is back-scattered by a second iTO phonon. This process is known as double resonant (DR), because the incident or scattered photon and the first or second phonon scattering are resonant with electronic levels in the graphene. Alternatively, the G′ band process can also be triple resonant, which is shown in Fig. 2.5. In this case, both carriers are scattered by iTO phonons from near the K point to the K′ point and recombine by emitting a photon. The G′ band can be used to determine the number of graphene layers and the stacking structure in a flake.

The defect can be evaluated by the intensity ratio between G and D peak. A point defect is the simplest and most common type of defect that can be generated in a graphene lattice.

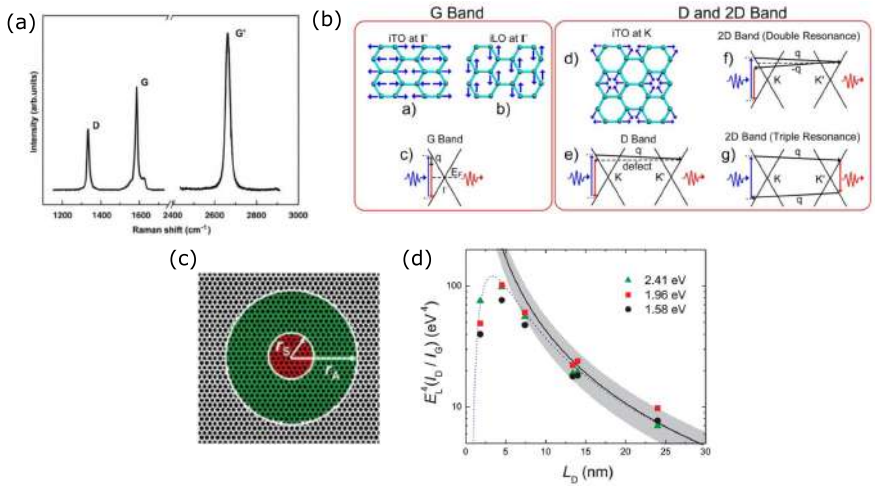

Fig. 2.5 The Raman of graphene.

The relation between the intensity of G band $I(\mathrm{G})$, D band $I(\mathrm{D})$ and the average distance between defects L_D can be written as

$$\frac{I(\mathrm{D})}{I(\mathrm{G})} = C_A \frac{r_A^2 - r_S^2}{r_A^2 - 2r_S^2} \left[e^{-\pi r_S^2/L_D^2} - e^{-\pi\left(r_A^2 - r_S^2\right)/L_D^2} \right]. \tag{2.1}$$

The r_S defines the radii of a circular area where the lattice structure is destroyed by the impact of the ion so the D band will not appear. On the other hand, the r_A defines the radii of a circular area where the structure is not destroyed by the ion so the D band is activated, as shown in Fig. 2.5. L_D is evaluated by scanning tunneling microscopy characterization. The parameter $C_A = 160E_L^{-4}$ where E_L is the laser energy of Raman spectrum. In present research, the 532 nm (2.33 eV) green laser is used. By considering $L_D \gg (r_A,\ r_S)$, $r_A = 3.1$ nm, and $r_S = 3.1$ nm, the Eq. 2.1 can be rewritten as

$$L_D^2\left(\mathrm{nm}^2\right) = \frac{4.3 \times 10^3}{E_L^4} \left(\frac{I(\mathrm{D})}{I(\mathrm{G})} \right)^{-1} \tag{2.2}$$

Fig. 2.5 shows the result of $E_L^4(I(\mathrm{D})/I(\mathrm{G}))$ versus L_D using different laser energies (1.58 eV, 1.96 eV, and 2.41 eV). From this plot, one can see that all the data with $L_A \geq 10$ nm fall on the same solid curve in Fig. 2.5. In terms of excitation laser wavelength $\lambda = 532$ nm, we have

$$L_D^2\left(\mathrm{nm}^2\right) = 1.8 \times 10^{-9} \lambda_L^4 \left(\frac{I(\mathrm{D})}{I(\mathrm{G})} \right)^{-1} \tag{2.3}$$

With L_D increasing (low defect density regime), $I(\mathrm{G})/\mathrm{I}(\mathrm{D})$ becomes larger which is in agreement with expectation.

2.2.2 Atomic force microscope

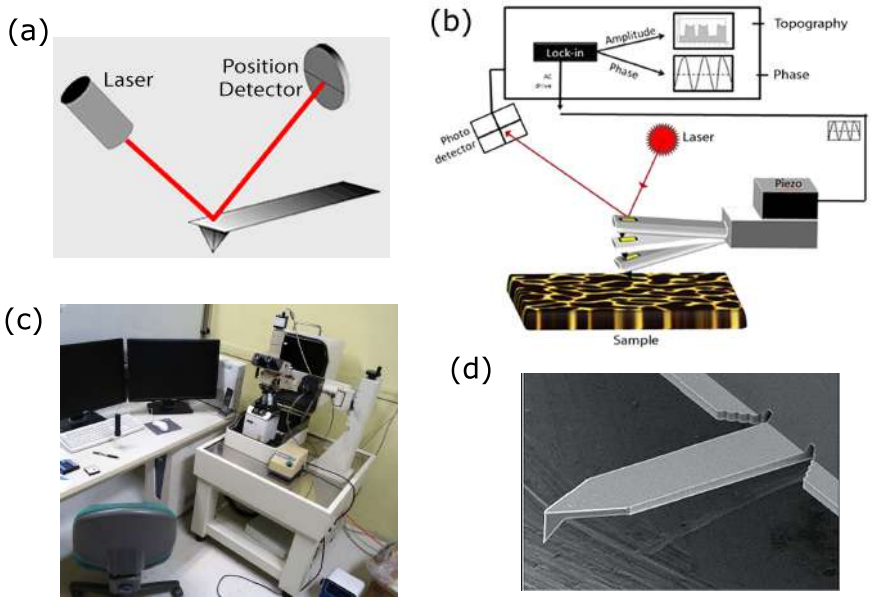

Fig. 2.6 Atomic force microscope (AFM) of present work. (a) Schematic diagram of AFM instrument. (b) Schematic diagram of dynamics force mode. (c) The AFM instrument in the present research. (d) The scanning electronic microscope image of an AFM probe.

Introduction of atomic force microscope

Atomic Force Microscopy (AFM) is a high-resolution imaging technique extensively used to characterize surface properties at the nanoscale. Unlike the Scanning Tunneling Microscope (STM), which is limited to imaging conducting or semiconducting surfaces, AFM can analyze almost any type of surface, including polymers, ceramics, composites, glass, and biological samples. AFM operates by scanning the sample surface with a sharp probe mounted on a flexible cantilever. The cantilever is deflected by the interaction forces between the cantilever's probe and the sample, such as van der Waals forces, electrostatic forces, or mechanical contact. These deflections are measured with sub-nanometer precision using a laser beam reflected off the cantilever onto a photodetector. AFM can generate detailed topographical height images of surfaces. Its versatility and non-destructive nature make it an essential tool in materials science, biology, and nanotechnology.

How the AFM works

AFM Probe Deflection: The interaction between the probe and the sample surface causes the cantilever to deflect. A laser beam deflection system measures this deflection by

reflecting a laser from the back of the reflective cantilever onto a position-sensitive detector (Fig. 2.6a). AFM probes are typically micro-fabricated from Si or Si_3N_4. The typical tip radius of an AFM probe ranges from several nanometers to tens of nanometers.

Measuring Forces: The force is calculated by measuring the deflection of the lever and using the known stiffness of the cantilever. Hooke's law gives:

$$F = -kz, \tag{2.4}$$

where F is the force, k is the stiffness of the lever, and z is the deflection of the cantilever. The AFM has a feedback loop using the laser deflection to control the force and tip position. As the tip interacts with the surface, the laser position on the photodetector is used in the feedback loop to track the surface for imaging and measuring.

Dynamic mode for AFM measurement

The dynamic force mode (DFM), also known as tapping mode or oscillating mode, is mainly used for measurements in this thesis (Fig. 2.6b). In DFM, the cantilever oscillates as it approaches the sample surface at a high frequency near resonance. The interaction force between the probe and the sample is reflected to changes of the cantilever's amplitude or frequency, which are maintained at a constant level while scanning the sample surface.

In this mode, the probe taps the surface, resulting in gentle interactions that help preserve the sharpness of the tip and minimize damage to the sample. This kind of interaction also minimizes torsional forces between the probe and the sample, which are especially intensified in static imaging mode. These features are especially advantageous for the measurement of soft or brittle materials, such as polymers or nanoparticles.

Additionally, phase imaging can be simultaneously obtained during DFM measurements. This technique provides additional information about the material properties of a sample beyond its topography. The phase image is generated by measuring the phase shift between the driving signal used for the cantilever's oscillation and its actual response. The phase shift offers valuable insights into the sample's mechanical properties, such as elasticity, stiffness, and adhesion.

In this thesis, the AFM/DFM measurements were conducted using the Hitachi High-Tech AFM5100N (Fig. 2.6c). The parameters of the probe are as follows (Fig. 2.6d): a resonant frequency of 150 kHz, a spring constant $k = 9$ N/m, and a tip radius of 7 nm (OMCL-AC200TS-R3 from Olympus).

2.2.3 Electrical characteristics analysis

The current-voltage characteristic curves were measured using an electrical performance analyzer equipped with a manual probe station. Electrodes were added by applying silver paste (Fujikura Kasei, DOTITE D-500) to the edges of the graphene. Due to the sample size of $\sim 300\mu m$, the silver electrode deposition process was conducted under a microscope. Using conductive glue to deposit silver electrodes is a simpler process, requiring no complex lithography or metal deposition steps. It does not affect the quality of the sample.

2.3 Molecular dynamics simulation

Molecular dynamics (MD) simulation is a computational technique used to study atomic and molecular behavior by solving Newton's equations of motion for systems of interacting particles. Through MD simulations, researchers gain insights into atomic-scale mechanisms that are challenging to observe experimentally, such as material structure, thermodynamics, and chemical reactions. These simulations have broad applications across fields, providing a deeper understanding of material properties like thermal and mechanical characteristics, defect formation, and fracture behavior, as well as protein folding and molecular interactions in biological systems. MD is also crucial for predicting nanoscale behavior, assisting in the design of new materials and nanostructures, and analyzing complex systems like liquids, gases, and amorphous solids. Additionally, it sheds light on processes like reaction dynamics and diffusion that are difficult to examine in laboratory settings. The MD simulation has been a powerful tool for the study of low-dimensional materials such as graphene, CNT and, MoS_2.

In MD simulations, a particle represents one or a group of atoms based on simplified assumptions. The interactions between particles are governed by potential energy functions, typically in the form of force fields. These force fields describe how atoms or molecules influence one another through bonded interactions (such as bond stretching, angle bending, and torsion) and non-bonded interactions including van der Waals forces and electrostatics. The forces acting on each particle are calculated from these potential energy functions, allowing the simulation to evolve over time according to Newton's second law:

$$F = -\nabla U = ma, \tag{2.5}$$

where F is the force on each atom, m is its mass, a its acceleration, and U the potential energy.

The MD process begins with initializing a system, defining atomic coordinates, velocities, and the thermodynamic ensemble (e.g., NVT, NPT). Integration algorithms, such as the Verlet or velocity-Verlet algorithms, are used to calculate the new positions and velocities of atoms at each time step, typically on the order of femtoseconds. These small time steps allow for the observation of atomic-scale events and time evolution of system properties over picoseconds to nanoseconds.

In our study, we use the AIREBO potential to simulate the interaction between carbon atoms of graphene and CNTs [86]. The AIREBO potential is a pair potential that incorporates the bond stretching, angle bending, and torsion of carbon bonds. The non-bond interaction is described by the Lennard-Jones potential. The famous open-source software, large-scale atomic/molecular massively parallel simulator (LAMMPS) [87], is used for MD simulation. The computation works utilized the computational resources of the Institute of Solid State Physics (ISSP) supercomputer center at the University of Tokyo.

Chapter 3

Reduction of interlayer interaction in multilayer graphene with carbon nanotube insertion

3.1 Background

The carbon nanotube is selected as the first candidate for the nanospacer. Compared with other nanospacers, the CNT is another allotrope of carbon with the same sp^2 hybridized structure as graphene, which does not introduce dopants from other elements. Numerous previous studies have reported that the graphene and CNT (Gr-CNT) composite system has excellent electronic properties and a high surface-to-volume ratio, which provides widespread potential applications in electronic devices [88–91, 81], energy storage [92, 79, 93], chemical catalyst [94, 95, 82, 96], and water treatment [21, 97]. In these systems, the microscopic structure, particularly the surface ratio and the ratio of single-layer graphene, plays a crucial role in determining performance. Therefore, in-depth investigations at the micro-scale are necessary.

Graphene is a material with excellent electrical, thermal, and optical properties [4, 98, 15, 11, 13] and broad prospects for applications [99–102, 14]. Monolayer graphene has a unique band structure with a linear electronic dispersion, which results in high carrier mobility [4, 98] and uniform light absorption of a wide range of wavelengths [15, 100]. Moreover, multilayer graphene shows high electrical and thermal conductance and light absorption with the increase of layer number [16, 103, 104]. The screening effect of multilayer graphene also prevents the degradation of the electronic transportation properties caused by the surrounding environment, including charge impurities and substrate roughness [104]. However, the

energetically favorable AB stacking in multilayer graphene leads to a strong interlayer interaction, which results in a parabolic electronic dispersion [105]. The intrinsic properties of monolayer graphene, including high carrier mobility, are undermined. Therefore, reducing interlayer interactions allows each layer to exhibit monolayer-graphene-like properties, thereby enhancing the overall material performance of multilayer graphene.

A feasible approach for suppressing interlayer interactions is to increase the interlayer distance. Theoretical analysis has proven that interlayer coupling decreases with the increase of interlayer distance [75, 106]. Experimental observations have shown that the intercalation of small molecules such as $MoCl_5$ and $AlCl_3$ into multilayer graphene reduces the interlayer interaction [75, 107]. Nanospacers such as NDs, CNTs, and nanofibers can also prevent restacking and reduce the interlayer interaction in graphene sponge structures [82, 83, 108].

The microstructure of the Gr-CNT composite system has a remarkable impact on properties. The addition of CNTs with a diameter of several nanometers can markedly increase the interlayer distance and reduce interlayer interaction [106]. Consequently, each graphene layer is remarkably separated and almost suspended. The benefits of suspended graphene include ultrahigh carrier mobility and ballistic transport [109, 99, 110–112]. However, the single-atom layer structure of graphene results in its low stiffness to bending deformation [113]. The adsorption interaction among graphene layers results in the bending of graphene and a decrease in interlayer distance [114, 84, 115, 116, 85]. Thus, negative factors, including strong interlayer coupling, electron scattering, and a decrease in the surface-to-volume ratio, will appear. Thus, investigating the real effect of CNT insertion on the microstructure of the graphene and CNT composite system is necessary to comprehensively understand and optimize their interaction. In previous experimental studies, the graphene and CNT composite system was usually fabricated through a random mixture of liquid phases, making it difficult to control the layer number and to ensure the CNT insertion between all graphene layers [82, 83]. Therefore, a new fabrication approach with enhanced structural controllability must be developed. In addition, the MD simulation was employed to investigate the mechanical properties of a multilayer graphene and CNT stacking structure, including elastic constants [84]. The deformation of CNT encapsulated by two graphene layers is also studied theoretically [85]. However, the influencing factors that determine the microstructure, such as the size and distribution of CNTs, have not been systematically studied.

In this study, I investigated the multilayer graphene stacking structure with CNT insertion through experiments and simulations. First, I experimentally fabricated such a Gr-CNT stacking structure using a dry transfer method. Highly controlled stacking structures with defined graphene layer numbers are achieved by alternately transferring monolayer graphene and depositing CNTs. Raman spectroscopy confirms a weak interlayer interaction, and the

AFM method verifies an increase in interlayer distance. Then, MD simulations were conducted to study the microstructure. A systematic investigation of the effect of CNT insertion on the interlayer distance was also conducted, including the CNT distance, diameter, and arrangement. A configuration transition from interlayer suspension to interlayer adsorption with increasing CNT distance was observed. The critical transition distance increases with CNT diameter. This study provides support for controlling the microstructure of the graphene and CNT composite system and enhancing the material properties.

3.2 Methods

Experimental methods. The Gr-CNT stacking structure was fabricated experimentally using the dry transfer method (Figure 3.1). The monolayer graphene was prepared on Cu foil by the CVD method [117, 118]. The graphene was transferred onto a silicon substrate (with 300 nm SiO_2 oxide layer) using the wet transfer method with a poly(methyl methacrylate) (PMMA) film [119, 120], as shown in Figure 3.1a. This step can make graphene on the silicon surface easier to be manipulated in subsequent experiments. Then, the CNT nanospacers were scattered on the graphene surface by spin coating the dispersion of CNT (Figure 3.1b). The CNT was synthesized by using the arc-discharge method and dispersed in ethanol with a concentration of 0.05 mg/mL (Meijo Nano Carbon, FH-P). The CNT is single walled with a diameter of 1–3 nm according to the manufacturer's information. The sample was placed on a hot plate of 90 °C to let ethanol evaporate. The areal density of the CNT was increased by repeated spin coating for designated times. The second graphene layer was picked up from the Si substrate, which is prepared by the same wet transfer method and covered onto the CNT nanospacer by using the dry transfer method using polymer stamps[121–123], as shown in Figure 3.1c. The successful transfer of the second layer can be confirmed by using an optical microscope (see Figure 3.2). A multilayer stacking structure can be fabricated by repeating the spin coating of CNT and graphene using a dry transfer process (Figure 3.1d). Raman spectroscopy was performed using a $\times 100$ objective lens with a laser excitation of 532 nm and a typical spot diameter of ~ 1 μm (Horiba, LabRAM HR-800). AFM measurements were conducted in the dynamic force mode (Hitachi High-Tech, AFM5100N).

Simulation method. I conducted MD simulations using LAMMPS program [87] to provide more details on the microstructure of Gr-CNT stacking and the influence of various parameters of CNTs. The simulation model is shown in Figure 3.4. Two parallelly aligned CNTs are encapsulated in two graphene layers (Figure 3.4a). The periodic boundary condition is added in the in-plane x and y directions to simulate the CNT array aligned at equal distances of infinite length. The width of the graphene layers and the length of CNTs are both $W = 6.7$

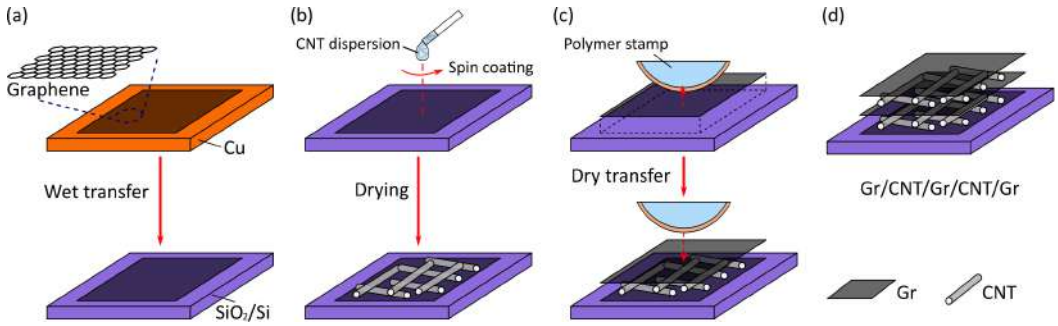

Fig. 3.1 Experimental process of making graphene (Gr) and CNT stacking structure. (a) The CVD graphene is first transferred from Cu foil to Si substrate. (b) The CNT nanospacer is distributed on graphene by spin-coating CNT dispersion. (c) The upper graphene layers are covered by using the dry transfer method. (d) Schematic diagram of the multilayer graphene/CNT stacking structure with three graphene layers (Gr/CNT/Gr/CNT/Gr).

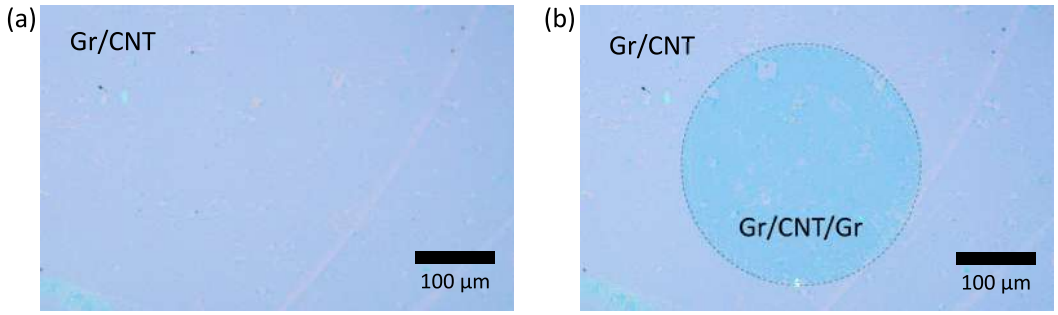

Fig. 3.2 (a) Optical microscope image of Gr/CNT on SiO_2/Si substrate. (b) Optical microscope image of Gr/CNT/Gr after dry transfer. The region in the dashed circle is covered by a second graphene layer.

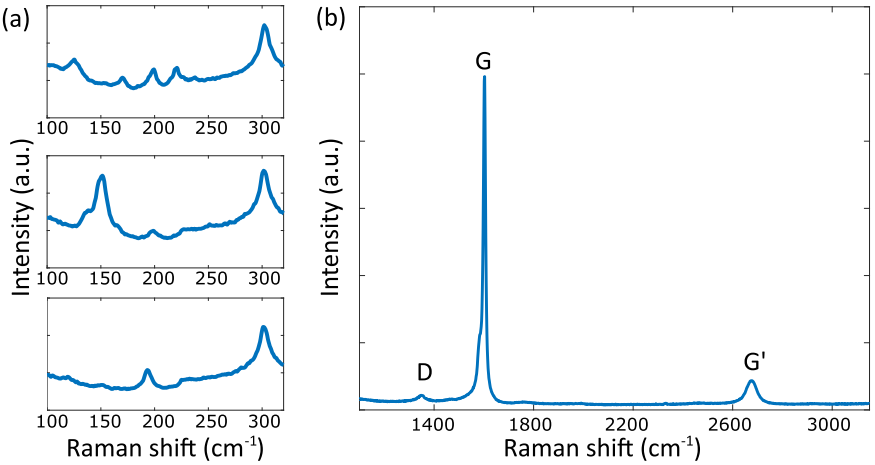

Fig. 3.3 Raman spectra of CNT. (a) The RBM signals of CNT on SiO_2/Si substrate on different points. The detected RBM mode peak positions ω_{RBM} range 125—198 cm^{-1}. Thus, the diameter d_{CNT} is 1.2—2.0 nm, according to the relation $\omega_{\mathrm{RBM}} = A/d_{\mathrm{CNT}} + B$, where $A = 217.8\ \mathrm{cm}^{-1} \cdot \mathrm{nm}$ and $B = 15.7\ \mathrm{cm}^{-1}$[124, 125]. (b) Raman spectrum of CNT including D, G, and G' peaks, The I(G')/I(G) of CNT is 0.07.

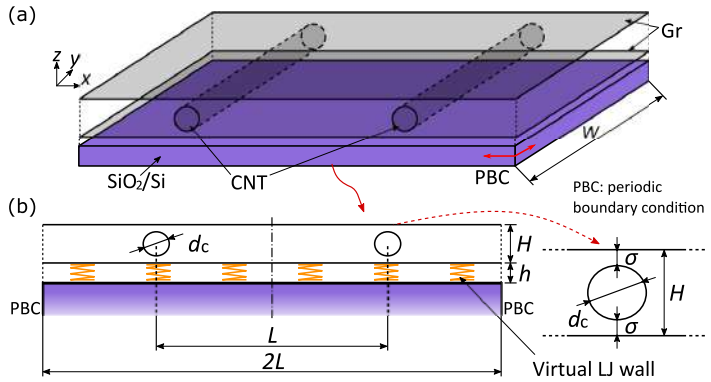

Fig. 3.4 Schematic representation of the simulation system in the three-dimensional view (a) and the front view (b). The system contains two graphene layers and two CNTs aligned in parallel with the y direction. The width of the graphene W, equal to the length of CNTs, is fixed. The length of graphene is $2L$ in the x direction. The systems with different CNT distances L and diameters d_{c} are simulated. The initial distance between the two graphene layers is $H = d_{\mathrm{c}} + 2\sigma$ as shown in the zoom-up figure. The in-plane x and y directions are set with periodic boundary conditions.

nm in the simulation system. The distance of the CNTs is L, and the length of the graphene layers is $2L$ (Figure 3.4b). The graphene interlayer distance of the initial configuration $H = d_c + 2\sigma$, where d_c is the diameter of the CNTs, and σ is the interlayer distance between graphene layers in graphite. Here, I took $d_c = 0.55$ nm, 0.68 nm, 1.08 nm, and 1.35 nm, and $L = 10$–70 nm. The AIREBO potential [86] is used to describe the internal short-range interactions of carbon atoms in a graphene layer or a nanotube. The short-range interaction energy varies with changes in C-C bond lengths and bond angles. This can describe the deformation of graphene and CNT and the resulting energy variation. The AIREBO potential is selected because it is widely used in the mechanical behavior of graphene and CNT with reasonable precision and efficiency and can be easily implemented in LAMMPS for quick results [14, 126–130]. Note that recently developed machine learning-based interatomic potentials [131, 132] could offer a promising alternative with proper validation in graphene and CNT systems. However, I consider the treatment of classical potential sufficient for the current simulations since no bond-breaking of C atoms that critically requires density functional theory accuracy is involved. To confirm the validity of the model, I simulated the pristine properties of graphene and CNT with the AIREBO and LJ potential. These properties are in accordance with experimental and density functional theory simulations. There is also long-range van der Waals (vdW) interactions between different graphene layers and CNTs. In MD simulation, the vdW interaction is described by the Lennard-Jones (LJ) potential

$$E_{\mathrm{LJ}} = 4\varepsilon \left(\frac{\sigma^{12}}{r^{12}} - \frac{\sigma^{6}}{r^{6}} \right) \tag{3.1}$$

where r is the distance between two atoms. The parameter $\varepsilon = 0.00284$ eV is the depth of the potential well, and $\sigma = 0.34$ nm is the zero-energy point and balance distance between graphene layers in graphite [86]. In inducing a vdW interaction between the upper and lower graphene, I set the cutoff radius for long-range interactions larger than the interlayer distance ($r_{\mathrm{cutoff}} = H + 0.3\sigma$). This process results in increased computational time for simulation. The lower graphene is constrained by a virtual LJ wall to simulate the adsorption effect of the SiO_2 layer on the Si substrate [133–135]. The energy of the wall-atom interaction is calculated as follows:

$$E_{\mathrm{sub}} = \frac{\Gamma_0}{\rho_a} \left[\frac{1}{2} \left(\frac{h_{\mathrm{equ}}}{h} \right)^{9} - \frac{3}{2} \left(\frac{h_{\mathrm{equ}}}{h} \right)^{3} \right] \tag{3.2}$$

where h is the distance between the carbon atom and the virtual LJ wall. The adhesion energy [136–138] is $\Gamma_0 = 0.45$ J/m^2, and the balance distance between graphene and SiO_2 substrate [139, 140] is $h_{\mathrm{equ}} = 0.42$ nm. The areal density of carbon atoms is $\rho_a = 38$ atom/nm^2. The

upper graphene layer is not constrained by such wall-atom interaction, and thus the evaluation of upper graphene deformation is not affected. The system is relaxed in the NVT ensemble at 300 K with a simulation timestep of 1 fs until the energy and configuration of the system reach equilibrium. Thus, the energy-favorable configuration is obtained.

3.3 Raman analysis of stacked graphene with CNTs

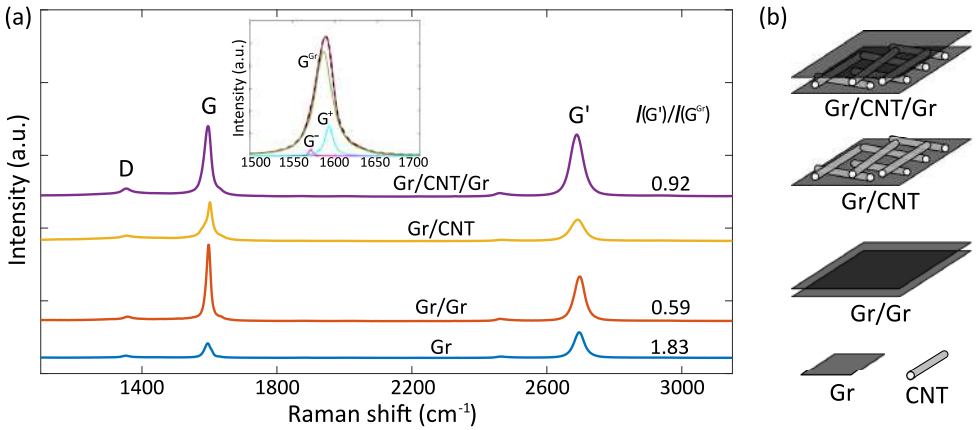

Fig. 3.5 (a) Raman spectrum of Gr (blue), Gr/Gr (red), Gr/CNT (yellow), and Gr/CNT/Gr (purple). Representative spectra obtained from a single measurement point are shown for each sample. The subgraph indicates that the G peak of Gr/CNT/Gr consists of G^{Gr} (at 1580 cm^{-1}) of graphene and G^{-} (at 1572 cm^{-1}) and G^{+} (at 1592 cm^{-1}) from single-walled CNTs. The intensity ratio of the G′ peak to G^{Gr} peak ($I(G')/I(G^{Gr})$) of Gr, Gr/Gr, and Gr/CNT/Gr is indicated. (b) Schematic of the corresponding systems, Gr/Gr, Gr/CNT, and Gr/CNT/Gr, in (a).

Raman spectroscopy first validates the weakening of the interlayer interaction of graphene by CNT insertion (Figure 3.5). Typical Raman spectra of monolayer graphene (Gr) exhibit the D peak ($\sim 1350\ cm^{-1}$), G peak ($\sim 1580\ cm^{-1}$), and G′ peak ($\sim 2700\ cm^{-1}$)[141]. The D peak is affected by crystal defects [141]. The intensity ratio of D peak to G peak ($I(D)/I(G)$) is 0.11 for monolayer graphene, with an estimated defect density of $2.44 \times 10^{-4}\ nm^{-2}$ [142]. The G peak intensity increases with the graphene layer number [143, 144]. The G′ peak relative intensity is sensitive to the graphene layer number and stacking order [145, 19]. For monolayer graphene, the intensity ratio of the G′ peak to the G peak ($I(G')/I(G)$) is generally 2–4 [145, 19, 146, 110]. The $I(G')/I(G)$ ratio decreases with the increase of the layer number for the AB stacking multilayer graphene due to the strong interlayer interaction and altered band structure with parabolic dispersion. A relatively high $I(G')/I(G)$ ratio can be observed in the random stacking multilayer graphene [147, 148, 141]. In random

stacking graphene, the interlayer interaction is weaker than the AB stacking graphene, and the interlayer distance is slightly larger [75]. The band structure of the random stacking graphene resembles the monolayer graphene with linear dispersion [105, 106]. The CNT also has the D peak, G peak, and G′ peak at similar positions. For single-walled CNTs, the G peak splits into two sub-peaks: G^- (at 1572 cm^{-1}) and G^+ (at 1592 cm^{-1}) [88]. A radial breathing mode (RBM) also appears between 100 cm^{-1} and 250 cm^{-1} [124, 125]. According to the RBM peak position ω_{RBM}, the diameter of CNT is estimated to be 1.2–2.0 nm. Note that the intensity of RBM signals for CNTs with diameters larger than 2 nm is weak and hardly observed. The diameter of CNT is consistent with the manufacturer's information. In the sample, the monolayer graphene shows $I(G')/I(G) = 1.83$, which is slightly lower than the typical value because of some multilayer islands on the CVD graphene and the doping from substrate impurities and PMMA residue. In the case of bilayer graphene (Gr/Gr), the $I(G')/I(G)$ ratio remarkably decreases to 0.59, which is consistent with the previous study [143, 147, 148]. The G′ peak is also lower than the G peak in monolayer graphene after adding CNTs (Gr/CNT). The G peak exhibits an asymmetric shape because of the overlapping of the G peak from graphene and split G^- and G^+ from CNTs. For the bilayer graphene/CNT stacking structure (Gr/CNT/Gr), the contribution from CNT should be removed when calculating $I(G')/I(G)$. A three-peak fitting approach can extract the graphene component in the G peak. The fitting result is shown in the subgraph of Figure 3.5a, and the intensity of the graphene G peak component is referred to as $I(G^{Gr})$. The CNT also shows a G′ peak at $\sim 2700 cm^{-1}$ (see Figure 3.3). The G′ to G ratio is ~ 0.07 for CNT on SiO_2/Si. The proportion of the G^- and G^+ peak within the G peak is remarkably smaller than that of the G^{Gr} peak ($I(G^+)/I(G^{Gr}) = 0.29$). Therefore, the G′ peak induced by the CNT is negligible in the total G′ peak of the stacking structure. The $I(G')/I(G^{Gr}) = 0.92$ of Gr/CNT/Gr is higher than that of two directly stacked graphene layers (Gr/Gr). This result demonstrates a reduction of interlayer interaction in the Gr/CNT/Gr structure because of the insertion of CNTs.

I further investigated the impact of CNT density and layer number on the interlayer interaction by Raman spectroscopy (Figure 3.6). The intensity ratio $I(G^{Gr})/I(Si)$ of the G peak to the substrate silicon peak at 520 cm^{-1} is used to indicate the layer number of graphene, and the interlayer interaction was evaluated by the $I(G')/I(G^{Gr})$. Multiple data points were obtained by measuring different sample positions. The average value and standard error were calculated, and the results are plotted in Figure 3.6. The increase of $I(G^{Gr})/I(Si)$ indicates the increase of layer number from Gr to Gr/Gr and trilayer graphene (Gr/Gr/Gr). The ratio does not increase linearly with the number of layers. Previous studies have found that in randomly stacking bilayer graphene [147, 148], a phonon resonance

enhancement and an increase in the G peak intensity are observed when the twist angle between the two layers $\sim 12^{\circ}$. The multilayer graphene is stacked from polycrystalline CVD graphene with randomly oriented grains, which is also random stacking. Thus, a further increase in $I(\mathrm{G^{Gr}})/I(\mathrm{Si})$ is observed. Comparing the Gr/Gr and Gr/CNT/Gr with different CNT densities, lower values of $I(\mathrm{G^{Gr}})/I(\mathrm{Si})$ appear with increasing density. Previous studies observed a weaker G peak in suspended graphene compared with graphene on a SiO_2/Si substrate [110, 149], which is attributed to the effect of substrate. CNTs increase the interlayer distance and make some part of the upper graphene nearly suspended. More CNT nanospacers separate more parts of graphene layers, and the average interlayer distance increases in the measured spots. The partial suspension of graphene contributes to the decrease in $I(\mathrm{G^{Gr}})/I(\mathrm{Si})$. Then, the high CNT density was kept, and the stacking structure of trilayer graphene and CNTs (Gr/CNT/Gr/CNT/Gr) as well as the Gr/Gr/Gr was also fabricated (Figure 3.6). The $I(\mathrm{G'})/I(\mathrm{G^{Gr}})$ ratio in the Gr/CNT/Gr/CNT/Gr is higher than that of the Gr/Gr/Gr, demonstrating the continued effectiveness of CNT insertion with increasing layer number.

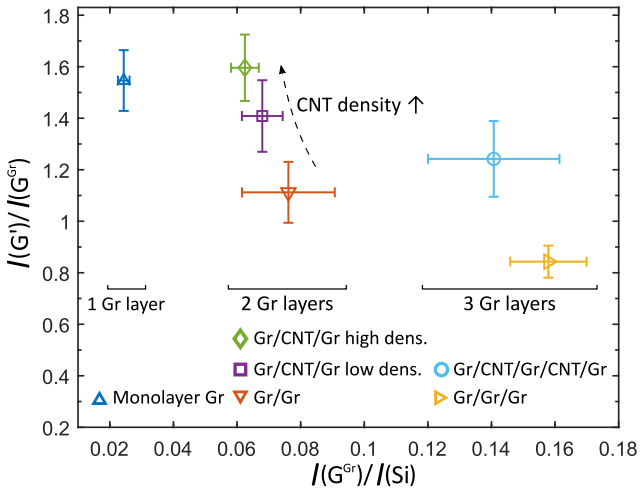

Fig. 3.6 Influence of CNT density and graphene layer number on $I(\mathrm{G'})/I(\mathrm{G^{Gr}})$ and $I(\mathrm{G^{Gr}})/I(\mathrm{Si})$. The average values and standard error bars of $I(\mathrm{G^{Gr}})/I(\mathrm{Si})$ and $I(\mathrm{G'})/I(\mathrm{G^{Gr}})$ are represented in the x-axis and y-axis, respectively. The results include monolayer graphene (blue triangle pointing upwards), Gr/Gr (red triangle pointing downwards), Gr/Gr/Gr (yellow triangle pointing to the right), Gr/CNT/Gr with low density (purple square), Gr/CNT/Gr with high density (green diamond), and Gr/CNT/Gr/CNT/Gr (cyan circle).

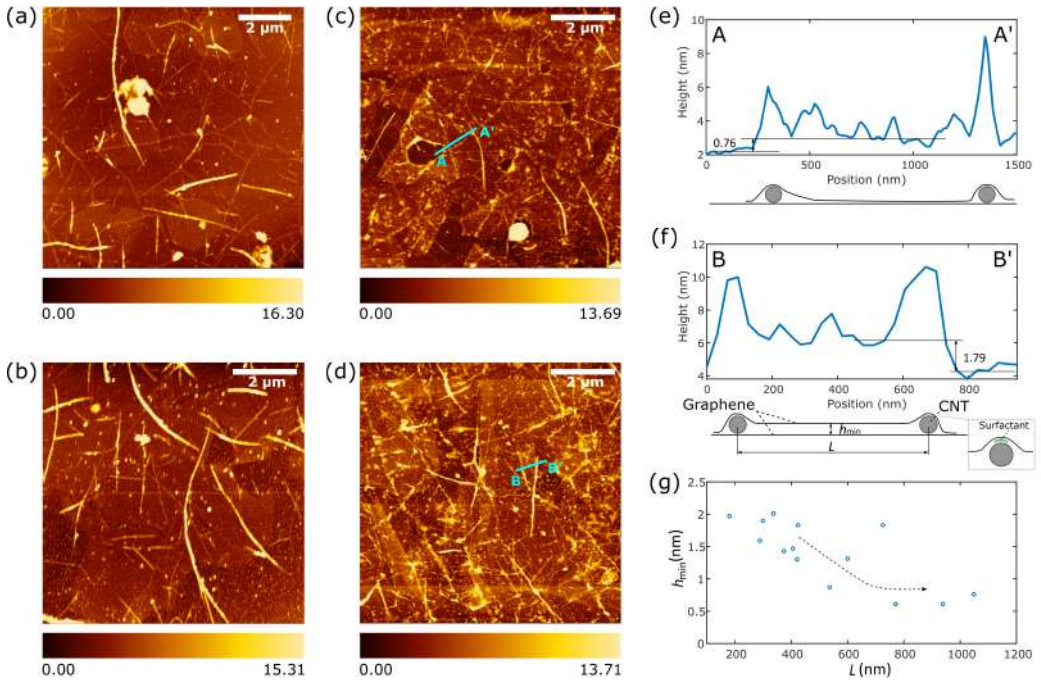

Fig. 3.7 AFM observation of Gr/CNT and Gr/CNT/Gr. (a, b) AFM images of Gr/CNT with low and high CNT densities. The areal density of CNT is evaluated to be 0.9 tube/μm^2 for low density and 3.14 tube/μm^2 for high density. (c, d) AFM images of Gr/CNT/Gr with low and high CNT densities. (e) Cross-sectional profile (A–A′) of Gr/CNT/Gr with a longer distance. The profile is selected from (c) with a lower CNT areal density. (f) Cross-sectional profile (B–B′) of Gr/CNT/Gr with a shorter distance. The profile is selected from (d) with a higher CNT areal density. The zoom-up figure illustrates the surfactant between graphene and CNT can form an additional peak and benefits the suspension. (g) The interlayer distance $h_{\min}$ between two graphene layers of different CNT distances L.

3.4 Nanostructure analysis with atomic force microscope

The insertion of CNT can reduce the interlayer interaction. The reduction can be attributed to the alteration of the microstructure by increasing the interlayer distance. The AFM measurement was employed to analyze the microstructure of the samples (Figure 3.7). The AFM images of the CNT distribution with low and high densities on Gr/CNT are shown in Figure 3.7a,b. The length of the CNTs ranges 1–4 μm, with a diameter of 2–8 nm. The measured diameter is higher than the parameters provided by the manufacturer. The surfactant is added when dissolving the CNTs in ethanol. The surfactant molecules adsorbed on the CNT can increase the measured diameter. The portion without adsorbed surfactant may lead to the attraction among CNTs, forming CNT bundles, which can also cause an increase in the measured diameter. The AFM images of the Gr/CNT/Gr with low and high densities are shown in Figures 3.7c and d, respectively. By comparing the cross-sectional images (Figures 3.7e,f), the two CNTs with a larger distance L show a lower thickness (h_{min}) of the region among CNTs. When the distance is $\sim$ 1000 nm, the height of the region among CNTs is 0.76 nm. When the distance between the CNTs is $\sim$ 600 nm, the height of the region is $\sim$ 1.79 nm, which is remarkably higher than the thickness of two graphene layers. Therefore, the upper layer of graphene is supported by the CNTs to form a partially suspended structure. Figure 3.7g illustrates the relationship between the distance of CNTs and the height of the upper-layer graphene, which was obtained through multiple analyses of AFM cross sections with the CNT distance of 190–1100 nm. As the distance between the CNTs increases, h_{min} gradually decreases. A theoretical study has reported that increasing the interlayer distance can weaken interlayer coupling and alter the band structure of multilayer graphene which is comparable with that of a single layer with linear dispersion [106]. CNTs induce the partial suspension of graphene, thereby increasing the interlayer distance. This finding explains the observed reduction of interlayer interactions in Raman spectroscopy.

3.5 Simulation of micro-structure with molecular dynamics

MD simulations of the Gr-CNT stacking structures can investigate the influencing factors of the CNT in detail and to study the microstructure comparatively with AFM observation. The MD simulation allows more convenient control of the CNT diameter and area density compared with the experiment. The intuitive microstructure figures can be output at a low cost compared with sample fabrication and AFM scanning. Graphene is assumed to be defect-free according to the Raman spectrum. The arrangement of CNTs was simplified to parallel aligned at equal distances. Simulating a random distribution of CNTs closer to the real

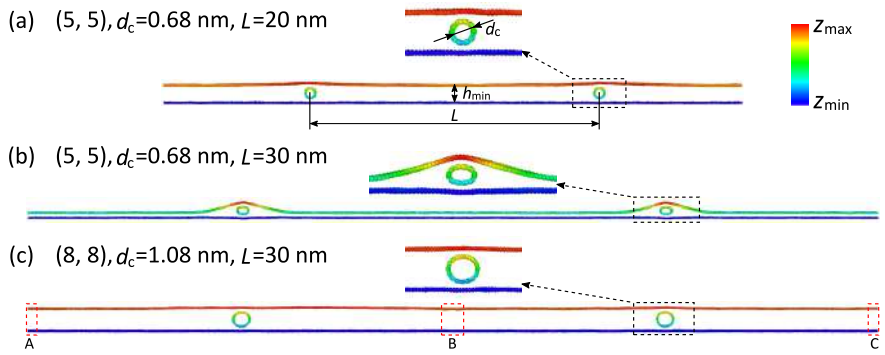

Fig. 3.8 Deformed configuration obtained by MD simulation of graphene/CNT stacking structure with different CNT diameters d_c and distances L. (a) The chirality index is (5, 5) and $d_c = 0.68$ nm, $L = 20$ nm. (b) The chirality index is (5, 5) and $d_c = 0.68$ nm, $L = 30$ nm. (c) The chirality index is (8, 8) and $d_c = 1.08$ nm, $L = 30$ nm. The zoom-up figures show the deformation of CNTs. The minimized interlayer distance h_{min} is calculated by averaging the distance at A, B, and C in the red dashed frames of (c). The color bar represents the z-coordinate of each atom, where z_{min} represented by blue corresponds to the minimum z-coordinate, and z_{max} represented by red corresponds to the maximum coordinate.

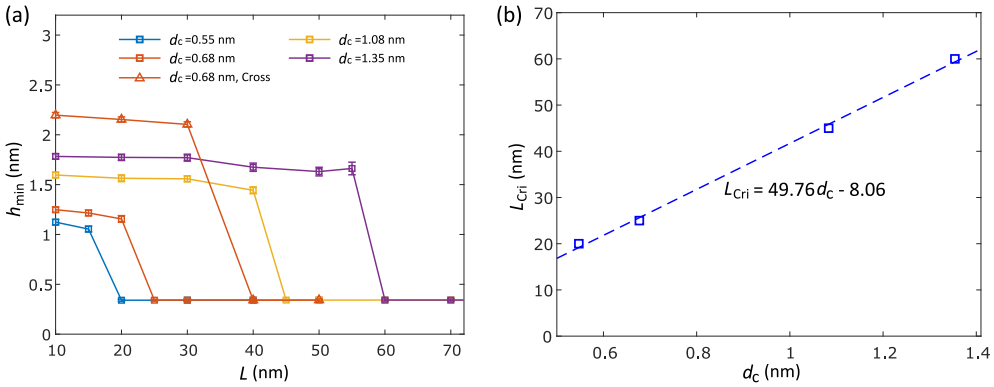

Fig. 3.9 (a) Effect of CNT diameter and distance on the minimum interlayer distance. The cases of parallel CNTs are plotted in lines with squares of blue ($d_c = 0.55$ nm), red ($d_c = 0.68$ nm), yellow ($d_c = 1.08$ nm), and purple ($d_c = 1.35$ nm). The cases of crossing CNTs with $d_c = 0.68$ nm are plotted in the red line with triangles. The error bar is the standard deviation of h_{min}, which is smaller than 0.08 nm. (b) Critical CNT distances (L_{cri}) where the adsorption configuration first appears as a function of the CNT diameter. The blue dashed line indicates the linear fitting result.

experiment requires a system with a larger size and a greater number of atoms, constrained by computational power and simulation time. Figure 3.8a–c shows three examples of the MD simulation with different CNT diameters d_c and CNT distances L ($d_c = 0.68$ nm, $L = 20$ nm, $d_c = 0.68$ nm, $L = 30$ nm, and $d_c = 1.08$ nm, $L = 30$ nm). In the first case (Figure 3.8a), the upper graphene is suspended among the CNTs, but it exhibits a slight curvature after relaxation, which is due to the vdW attraction between the layers. If the distance is increased to $L = 30$ nm (Figure 3.8b), the upper graphene is adsorbed on the lower graphene layer with evident bending deformation near the CNTs. The interlayer distance of the two graphene layers is 0.34 nm, which is close to the spacing of carbon layers in graphite. If the distance L is fixed and d_c increases to 1.08 nm (Figure 3.8c), then the upper graphene stays in suspension, which is similar to the first case.

Additional simulations were performed by varying the chirality indices, diameters, and distances between the CNTs (Figure 3.9). The final configurations are classified into two categories: upper graphene suspension and layer adsorption. The minimum interlayer distance $h_{\min}$ can be used to distinguish between the two configurations. It is calculated by averaging the distance between the graphene layers at the midpoint and two ends (Figure 3.8c). In the case of the same d_c when the distance L is small (Figure 3.9a), the $h_{\min}$ approaches the initial spacing H, indicating that the upper graphene layer remains suspended. As the CNT distance gradually increases and surpasses a critical value, the interlayer distance abruptly decreases to 0.34 nm, indicating the occurrence of interlayer adsorption. The system with the same CNT diameter and distance but different graphene width W and number of unit cell are simulated. The consistency of the result verifies the validity of periodic boundary conditions and the negligible influence of the specimen size. As the diameter d_c increases, the interlayer distance $h_{\min}$ in the suspended graphene configuration also increases. A large CNT diameter also increases the critical CNT distance (L_{cri}) at which the adsorption configuration appears (Figure 3.9b). The relation between d_c and L_{cri} is approximately linear. Linear regression is conducted to clearly show the relationship between d_c and L_{Cri} (dashed line in Figure 3.9b). In the experiments, CNTs are randomly distributed, and crossing CNTs are observed. Therefore, stacking structures with crossing CNTs were also simulated (triangles in Figure 3.9a). The model is shown in Figure 3.10. Compared with parallelly aligned CNTs, the crossing CNTs can increase the critical distance for configuration transition from suspension to adsorption.

The transition of configuration from suspension to adsorption configuration implies a change in potential energy. The total potential energy E_{pot} of the simulation system consists of several components:

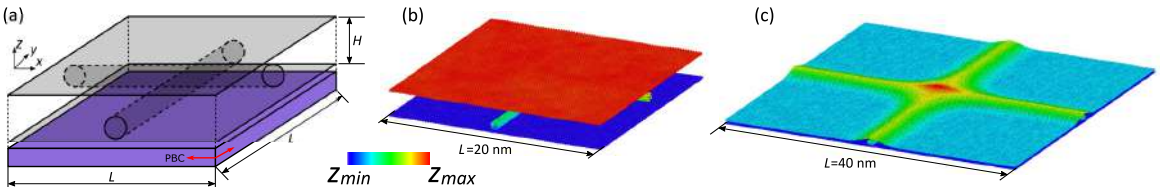

Fig. 3.10 (a) Schematic representation of the simulation system with crossing CNTs. The width and length of the graphene are both L. The initial interlayer distance $H = 2d_c + 3\sigma$. (b) Deformed configuration of the stacking structure with crossing CNT and $L = 20$ nm. (c) Deformed configuration of the stacking structure with crossing CNT and $L = 40$ nm. The color bar represents the z-coordinate of each atom, where $z_{\min}$ represented by blue corresponds to the minimum z-coordinate and $z_{\max}$ represented by red corresponds to the maximum coordinate.

$$E_{\text{pot}} = E_{\text{GrU}} + E_{\text{GrL}} + E_{\text{CNT}} + U_{\text{GrU-L}} + U_{\text{GrU-CNT}} + U_{\text{GrL-CNT}} \tag{3.3}$$

where E_{GrU} and E_{GrL} are the internal energy of upper and lower graphene layer described by the AIREBO potential. The CNT internal energy E_{CNT} includes the AIREBO potential for C-C bond and the LJ energy inside the CNT wall. The LJ interaction includes the components of $U_{\text{GrU-L}}$ (between upper and lower graphene), $U_{\text{GrU-CNT}}$ (between upper graphene and CNT), and $U_{\text{GrL-CNT}}$ (between lower graphene and CNT). Comparison is made for each component in Eq. 3.3 between the suspension and adsorption configuration of the system with the same d_{CNT} and L. A Δ operator acting on the particular energy represents the energy difference between the suspension (Sus) and adsorption (Ads) configuration (eg. $\Delta E_{\text{pot}} = E_{\text{pot, Sus}} - E_{\text{pot, Ads}}$). The suspension configurations for the cases with $L > L_{\text{Cri}}$ are obtained by extracting a frame at the initial stage of the simulation. The adsorption configurations for the cases with $L < L_{\text{Cri}}$ are obtained by adding a uniform force to atoms of upper graphene to induce adsorption. The force has no harmful effect on the output potential energy because the potential energy is only affected by the relative position coordinates of atoms. Each energy component for systems with different d_{CNT} and L was calculated (see Table 3.1).

Considering that the lower graphene layer remains nearly flat without remarkable deformation no matter whether the upper layer is suspended or adsorption, the difference for E_{GrL} is limited regardless of d_{CNT} and L (Table 3.1). The contact area between CNTs and graphene layers is minor compared with the whole graphene (see zoom-up pictures in Figure 3.8), which makes the change of $U_{\text{GrU-CNT}}$ and $U_{\text{GrL-CNT}}$ insignificant compared with $U_{\text{GrU-L}}$. Thus, the total potential energy E_{pot} and configuration of the system are primarily determined

by E_{GrU}, E_{CNT} and $U_{\text{GrU-L}}$ (see Figure 3.11), which writes

$$\Delta E_{\text{pot}} \approx \Delta E_{\text{GrU}} + \Delta E_{\text{CNT}} + \Delta U_{\text{GrU-L}} \tag{3.4}$$

Compared with the suspension configuration, the vdW energy decreases in the adsorption configuration, and the decreased value of energy becomes more significant with an increase in the size of graphene (see Figure 3.11 and Table 3.1). For larger L, more atoms are in the stable state of LJ interaction in the adsorption configuration. Upper graphene deformation leads to the bending of angles between C-C bonds and an increase of internal energy ($\Delta E_{\text{GrU}} > 0$). The collapse of CNTs also appears in adsorption configuration with an ellipse cross-section (see Figure 3.8b), which causes an extra increase of internal energy [85] ($\Delta E_{\text{CNT}} > 0$). Both ΔE_{GrU} and ΔE_{CNT} decreases lightly with an increase of L. The minor variations result from differences in the cross-sections of deformed CNTs and adjacent regions of upper graphene. For smaller L, the increase of $\Delta E_{\text{GrU}} + \Delta E_{\text{CNT}}$ is more significant than the decrease of $\Delta U_{\text{GrU-L}}$, making the suspension a more stable energy configuration ($\Delta E_{\text{pot}} < 0$). As L increases, the contribution of vdW interaction $\Delta U_{\text{GrU-L}}$ increases, leading to smaller energy for the adsorption configuration ($\Delta E_{\text{pot}} > 0$). Note that for $L = 20$ nm and $d_c = 0.68$ nm, the adsorption configuration is more energetically favorable ($\Delta E_{\text{pot}} > 0$) but the distance of the CNTs $L < L_{\text{Cri}}$. This is attributed to the presence of energy barriers during the configuration transition. In the simulation, the relaxation process starts with the suspension configuration as initial modeling. The upper graphene spontaneously approaches the lower one driven by vdW force. However, when the upper graphene undergoes a downward bending deformation, the increase of elastic energy exceeds the reduction in vdW energy which makes the intermediate configuration have higher potential energy ($E_{\text{pot, Inter}} > E_{\text{pot, Sus}}$ in Figure 3.11a). Consequently, the upper graphene reverts to the suspension configuration which is a local minimum (Figure 3.11b). The energy barrier will cause a metastable structure which requires further theoretical study. With increasing L, the upper graphene bending can induce a larger change in the vdW energy, and the energy barrier is overcome. The CNT deformation energy ΔE_{CNT} increases with its diameter d_c (purple arrows in Figure 3.11a). Larger $\Delta U_{\text{GrU-L}}$, *i.e.* larger L, is required to create an energetically favorable adsorption structure which contributes to increased L_{Cri}.

Experiments and MD simulations have simultaneously discovered that as the distance between CNTs increases, the structure transitions from an upper graphene layer suspension to an interlayer adsorption structure. The trend can qualitatively match, but the quantitative comparison has discrepancies. The critical length L_{cri} obtained by the MD simulation is 20–60 nm for CNTs with a diameter range of 0.55–1.35 nm. Based on the predictions from linear regression analysis, the critical length L_{cri} of CNTs with diameters ranging from 2–8

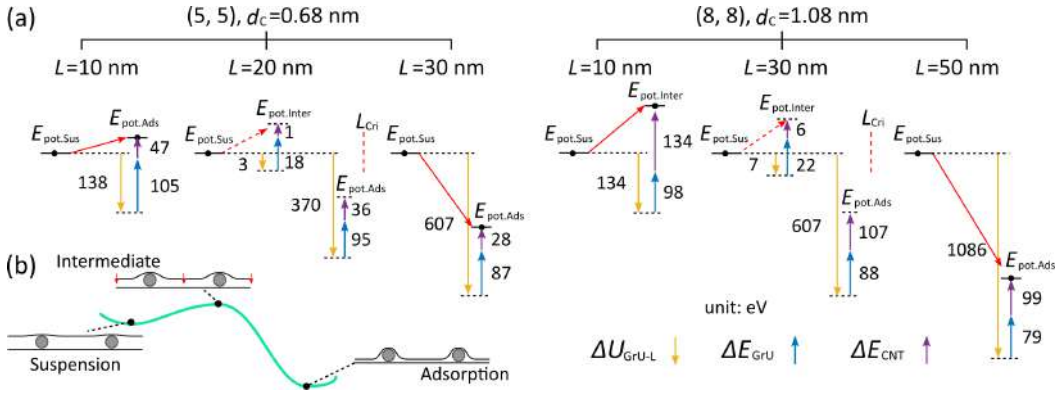

Fig. 3.11 (a) Comparison of the energy between suspension and adsorption for systems with different L and d_c. The yellow arrows represent the difference in graphene interlayer vdW energy $\Delta U_{\text{GrU-L}} = U_{\text{GrU-L, Sus}} - U_{\text{GrU-L, Ads}}$, while the blue and purple arrows represent the difference in energy of the upper graphene ΔE_{GrU} and CNT ΔE_{CNT}, respectively. The red arrows indicate the difference in total potential energy. The unit of energy is eV. (b) Schematic diagram of the energy barrier between the energy of suspension and adsorption configurations (corresponding to the two cases with intermediate state: $L = 20$ nm, $d_c = 0.68$ nm and $L = 30$ nm, $d_c = 1.08$ nm). The middle of upper graphene tends to deform downward (the intermediate state), but this deformation results in an overall increase of potential energy. As a result, the upper graphene returns to its suspension configuration, although the suspension configuration is a local minimum with larger energy than the adsorption configuration.

nm, which corresponds to the CNT diameters in the experiment, is estimated to be 90–390 nm. The experimental observations show graphene suspension with a CNT distance of 700 nm, which is larger than the prediction based on MD simulation. Several factors benefit the suspension of graphene in the experiment. In ethanol dispersion, the surfactant is added to promote CNT dissolution. The surfactant molecules mostly appear on the surface of CNTs to increase the affinity between CNT and ethanol solvent. After the heating and evaporation of ethanol solvent, some surfactants remain on the CNT surface. The surfactant molecules wrap the surface of CNTs by non-covalent interaction[150], which serves as spacers between carbon monolayers of graphene and CNTs. By comparing the AFM image (Figure 3.7f) and the MD simulation (Figure 3.8c), one can find an additional peak atop graphene around the CNT in the AFM cross-section while the configuration of upper graphene in MD simulation is almost flat. This could correspond to the surfactant between the graphene and the upper part of CNT, which increases the distance between CNTs and graphene layers σ (Figure 3.4b). Thus, the critical distance L_{cri} is increased. Moreover, the CNT is randomly distributed on the surface. The MD simulation indicates that crossing CNTs can increase the critical distance L_{cri} (see Figure 3.9a). The CNTs may also aggregate to form CNT bundles where the surfactant is not covered. This effect is similar to the increase of CNT diameter, leading to an increase in L_{cri}.

3.6 Conclusions

This chapter talks about the effect of CNT insertion to reduce the interlayer interaction in multilayer graphene. The stacking structure of graphene and CNT is experimentally fabricated. Raman spectroscopy and AFM measurement verify the reduction of interlayer interaction and increase of interlayer distance. In addition, MD simulations are conducted to systematically study the influencing factors. The Gr-CNT stacking structure exhibits two stable configurations: the upper-layer suspension and interlayer adsorption. The distance, diameter, and arrangement of the CNTs determine the selection of the stable structure. The present research contributes not only to the enhanced property of multilayer graphene but also to a comprehensive understanding of the microstructure of the Gr-CNT composite system to facilitate functional enhancement for wider application fields.

Table 3.1 Energy components of the three configurations (config.), suspension (sus.), adsorption (ads.) and intermediate (inter.) for systems with different L and d_c. The unit of energy is eV.

$d_c = 0.68$ nm							
Size L, config.	E_{pot}	$U_{\text{GrU-L}}$	$U_{\text{GrU-CNT}}$	$U_{\text{GrL-CNT}}$	E_{GrU}	E_{GrL}	E_{CNT}
10 nm, sus.	-90159.7	-1.3	-18.1	-17.7	-40789.5	-40791.3	-8541.86
10 nm, ads.	-90146.7	-139.3	-23.2	-19.7	-40685.0	-40790.5	-8488.98
20 nm, sus.	-170752.7	-3.8	-18.7	-17.6	-81082.7	-81088.7	-8541.1
20 nm, inter.	-170730.5	-6.6	-19.3	-18.3	-81064.6	-81081.8	-8539.78
20 nm, ads.	-170998.3	-373.4	-23.8	-19.3	-80987.6	-81089.3	-8504.95
30 nm, sus.	-252317.6	-3.2	-17.6	-17.6	-121864.0	-121877.2	-8538.04
30 nm, ads.	-252826.4	-610.6	-24.2	-20.7	-121777.2	-121883.5	-8510.18
$d_c = 1.08$ nm							
Size L, config.	E_{pot}	$U_{\text{GrU-L}}$	$U_{\text{GrU-CNT}}$	$U_{\text{GrL-CNT}}$	E_{GrU}	E_{GrL}	E_{CNT}
10 nm, sus.	-95460.0	-0.5	-24.5	-23.9	-40783.9	-40787.7	-13839.65
10 nm, ads.	-95400.2	-134.1	-42.6	-39.0	-40686.4	-40792.6	-13705.52
30 nm, sus.	-257635.8	-3.4	-27.5	-25.3	-121871.9	-121877.0	-13830.8
30 nm, inter.	-257606.1	-10.7	-30.2	-27.3	-121849.6	-121863.2	-13825.18
30 nm, ads.	-258080.3	-610.0	-43.4	-38.9	-121784.4	-121879.8	-13723.71
50 nm, sus.	-419784.2	-2.8	-24.3	-23.8	-202941.6	-202958.3	-13833.44
50 nm, ads.	-420736.7	-1088.8	-43.4	-38.8	-202862.5	-202968.4	-13734.75

Chapter 4

Nanodiamond Insertion on the Interlayer Interaction in Multilayer Stacking Graphene

4.1 Background

Graphene (Gr) is widely recognized for its excellent electrical [4, 98, 151], thermal [11], and optical properties [15], making it a material of great interest with enormous potential for practical applications across diverse fields, including optoelectronic devices [152, 153, 100], sensors [154], and energy storage devices [38]. Monolayer Gr with a one-atom-thick structure has a unique band structure characterized by gapless linear dispersion, resulting in high carrier mobility and a broad bandwidth light absorption [153]. With the increase of layer number, more benefits can be obtained from the multilayer structure such as high conductance and light absorption [16]. The screening effect also prevents the degradation of the electronic transport properties caused by the surrounding environment [104]. Moreover, twisted multilayer Gr can be obtained by changing the interlayer stacking angle. Interlayer coupling is tunable with the twisted structure creating the moiré superlattice and changing the band structure. Many novel phenomena such as superconducting states [155], ferromagnetic states, and van Hove singularity [156–158] could occur. However, the energetically favorable AB stacking in multilayer Gr leads to a strong interlayer interaction, which results in a parabolic electronic dispersion [105]. This strong interlayer coupling undermines the intrinsic properties of monolayer Gr.

The novel properties of multilayer Gr require a modified interlayer interaction and band structure. The change in interlayer distance and stacking angle could reduce interlayer

interactions, allowing each layer to exhibit monolayer-Gr-like properties, thereby enhancing the overall material performance of multilayer Gr. Intercalation is the widely reported method to increase the interlayer distance [71–77]. Metal atoms (Li and K) or small molecules ($MoCl_5$ and $AlCl_3$) are introduced between Gr layers by vapor deposition. The interlayer distance is increased, and the interlayer coupling is weakened. The tuned band structure resembles the monolayer Gr with linear dispersion [71]. Decreased sheet resistance [73, 77], doping effect [71], and quantum oscillation [72] are reported. However, the quality of intercalation is not uniform and sensitive to the stacking angle [77]. The intercalation is easier to happen in stacked Gr layers with a large twist angle [75, 77]. The alternative materials are limited to small molecules and metal atoms. The chloride molecules and metal elements could induce doping. Heating in a furnace with a relatively long reaction time is also required [73, 75].

The interlayer interaction can also be controlled by fabricating a nanospacer-inserted Gr stacking structure via transfer-based layer-by-layer assembly. Here, a nanospacer refers to a nanomaterial that separates the direct stacking of Gr layers. Spin coating facilitates the addition of nanospacers with the areal density easily controlled by adjusting the dispersion concentration. This method is applicable to larger nanomaterials other than small molecules. In previous work, carbon nanotubes (CNTs) are added between Gr layers [159]. The addition of CNTs with a diameter of several nanometers can increase the interlayer distance, and the upper Gr is partially suspended. Moreover, the interlayer interaction is reduced. However, CNTs tend to aggregate, forming bundle-like structures, which disrupt the uniform distribution on the Gr surface and hinder the effect of interlayer distance expansion. In improving the dispersibility of CNTs, surfactants are often added, which can introduce doping and contamination, thereby undermining the performance of Gr. Further research on other kinds of nanospacers is required for an optimal nanospacer. Thus, nanodiamond (ND) was selected as nanospacer, and its effect on interlayer interaction was investigated. The composition of two-dimensional Gr and zero-dimensional ND can be regarded as a mixed-dimensional heterostructure, where the material property is designable with the change of microstructure [160, 108]. Due to the spacing effect of NDs, the band structure of each Gr layer approaches that of the monolayer Gr with linear dispersion. The previous research reported the twisted stacked Gr to realize the monolayer band structure. However, twisted stacked Gr still has domains with AB and AA stacking [70]. By realizing monolayer band structure, the universal optical absorbance in a wide frequency region appears in multilayer Gr [161, 17] and paves the way for potential applications in the photonics and optoelectronic field. Previous research using scanning tunneling spectroscopy (STS) observed quantum tunneling properties of individual NDs [162]. By sandwiching Gr layers, the Gr/ND/Gr structure

can enable vertical conductive quantum tunneling electronic devices of micrometer. The 3-dimensional sponge of mixed Gr and ND also has potential applications in supercapacitors [163], catalysis [164], ion transport [165], and strain sensors [44]. The incorporation of NDs can modify the microstructure of the heterostructure, increase the effective surface area, and enhance material performance. The characteristic size of ND ($\sim$ 10 nm) prepared by detonation is larger than single-walled CNT (1–3 nm), which can form a larger interlayer space. Unlike the linear contact with CNT, the contact between ND and Gr is point-like, resulting in a smaller contact area and less impact on the intrinsic properties of the Gr material. The density of the dispersing liquid can also control the distribution density of ND on Gr. ND aggregation can be easily dissolved through ultrasonication [67–69].

In this work, the Gr and ND (Gr–ND) stacking structure was first experimentally fabricated by layer-by-layer wet transfer and spacer spin coating. Raman spectroscopy confirms a weak interlayer interaction, with an increase in the intensity ratio of the G′ peak to the G peak and a split of the G peak. Atomic force microscopy (AFM) verifies the increase in interlayer distance with upper Gr suspension. Molecular dynamics (MD) was used to simulate the microstructure and systematically elucidate the regularities and mechanisms of ND's influence on the interlayer distance. The high areal density and large diameter of NDs promote a larger interlayer distance with upper Gr suspension. Finally, a continuum model allows us to scale up simulations to match experimental conditions. A critical ND density above which the upper Gr suspension appears is predicted, which is qualitatively comparable to experimental observations. The selection of the final stable microstructure, between Gr suspension and interlayer adhesion, relies on which configuration has lower system energy.

4.2 Methods

4.2.1 Experimental Methods

The Gr–ND stacking structure was fabricated experimentally by using layer-by-layer transfer method (Figure 4.1) [159]. Monolayer Gr was prepared on Cu foil by chemical vapor deposition (CVD) [118, 117]. Gr was transferred onto a thermally oxidized silicon substrate (SiO_2/Si, with 300 nm SiO_2 oxide layer) using wet transfer with a polymethyl methacrylate (PMMA) film [119, 120] (Figure 4.1a). Then, ND nanospacers were scattered on the Gr surface by spin coating its dispersion (Figure 4.1b). High-purity ND (from Nippon Kayaku) was prepared by detonation and dispersed in ethanol with 2 w.t.%. The diameter of ND is 4–14 nm from AFM measurement [66]. ND impurities include Fe of 80 ppm, Zr of 2100 ppm, and Pd of 6–20 ppm. Hydrophilic functional groups of $-$OH and $-$COOH were

found on the ND surface, and no surfactant was added to the dispersion. The areal density of NDs was controlled by diluting the dispersion to different concentrations. Dispersions with 0.02 w.t.% and 0.2 w.t.% were prepared. Before spin coating, ND dispersion was treated by sonication for 60 min in ice water to prevent aggregation [68, 69]. Next, the second Gr layer was transferred atop using the same method. After each transfer, thermal annealing at 350 °C for 10 min in the air was conducted to remove the PMMA residue [166–168]. Raman spectroscopy was performed using a $\times 100$ objective lens with a laser excitation of 532 nm and a typical spot diameter of $\sim 1\ \mu$m (Horiba, LabRAM HR-800). AFM measurements were conducted in dynamic force mode (Hitachi High-Tech, AFM5100N).

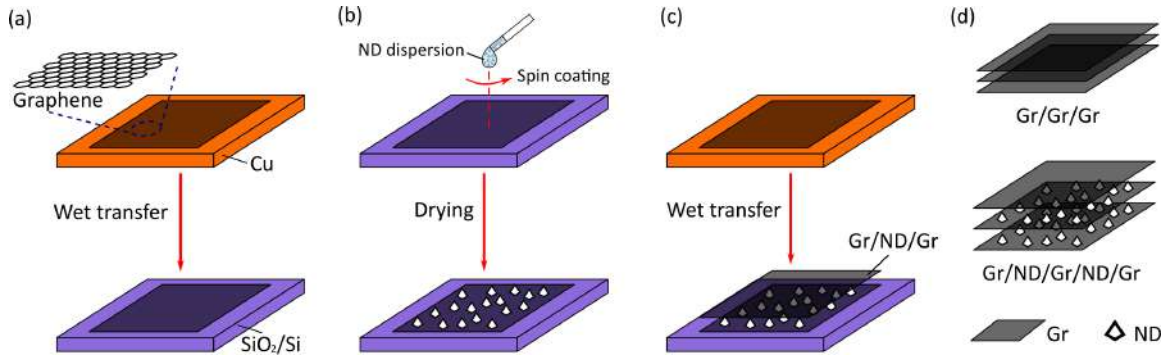

Fig. 4.1 Experimental process of making a graphene (Gr) and nanodiamond (ND) stacking structure. (a) Gr grown by chemical vapor deposition (CVD) is first transferred from Cu foil to SiO_2/Si substrate. (b) The nanospacer is distributed on Gr by spin-coating ND dispersion. (c) The upper Gr layers are covered using the same wet transfer method. (d) Schematic diagram of the triple–layer Gr (Gr/Gr/Gr) and multilayer Gr and ND (Gr–ND) stacking structure with three Gr layers (Gr/ND/Gr/ND/Gr).

4.2.2 Simulation and theoretical model

ND changes the microstructure by expanding the interlayer distance. Conducting theoretical analysis is necessary to comprehensively understand the mechanisms driving these changes. First, MD simulations were conducted using LAMMPS program [87] to provide more details on the microstructure of Gr–ND stacking and the influence of various ND parameters. The simulation model is shown in Figure 4.2. The NDs are encapsulated in the two Gr layers. Two types of boundary conditions were considered for Gr layers: the periodic boundary condition (PBC) and the free-edge boundary condition. The PBC simulates the situation in the center parts of large domains for the stacked Gr layers in real experiments. The cases with free-edge boundaries represent the environment near the edges and cracks of Gr layers. For PBC simulation cases, Gr was assumed to be defect-free, and the arrangement

of NDs was simplified to uniform in a square lattice with equal distance (Figure 4.2a). The PBC was added in the in-plane x and y directions to simulate the infinite area. Thus, the system can be divided into many unit cells with an ND inside (Figure 4.2a). In minimizing the simulation costs, only one unit cell was simulated (Figure 4.2b), which gives results consistent with those obtained from cases involving a larger number of unit cells, *i.e.* four NDs (Figure 4.7). Simulating a random distribution of NDs closer to the real experiment requires a system with a larger size and a greater number of atoms, constrained by computational power and simulation time. The distance L between NDs also equals the side length of the square Gr layer. A larger L indicates a lower areal density of NDs. The Gr interlayer distance of the initial configuration $H = d_{\mathrm{N}} + 2\sigma$ (Figure 4.2c), where d_{N} is the diameter of the NDs, and σ is the interlayer distance between Gr layers in graphite. Here, $d_{\mathrm{N}} = 1.0$ nm, 1.6 nm, and 2.0 nm, and $L = 5$–100 nm. The ND structure was obtained by selecting atoms within a sphere of diameter d_N from the bulk crystal. The modeled structure was relaxed in the NVT ensemble at 300 K for 1 ns to obtain a stable configuration. Then, the relaxed ND was used to model the Gr–ND structure. The deformation of ND was neglected, and a rigid body was set in the simulation thereafter. The rigid assumption for ND has a minor effect on the simulation. The AIREBO potential [86] describes the internal short-range interaction of carbon atoms in a Gr layer. The short-range interaction energy varies with changes in C–C bond lengths and bond angles. There are long-range van der Waals (vdW) interactions between different Gr layers and NDs. In MD simulation, the vdW interaction is described by the Lennard–Jones (LJ) potential,

$$E_{LJ} = 4\xi \left(\frac{\sigma^{12}}{r^{12}} - \frac{\sigma^{6}}{r^{6}} \right) \tag{4.1}$$

where r is the distance between two atoms. The parameter $\xi = 0.00284$ eV is the depth of the potential well, and $\sigma = 0.34$ nm is the minimum point and equilibrium distance between Gr layers in graphite [86]. In inducing a vdW interaction between the upper and lower Gr, the cutoff radius for long-range interactions was set larger than the interlayer distance ($r_{cutoff} = H + 0.3\sigma$). The lower Gr was constrained by a virtual LJ wall to simulate the adhesion effect of the SiO_2 layer on the SiO_2/Si substrate [159, 133–135]. The system was relaxed in the NVT ensemble at 300 K with a simulation timestep of 1 fs until the energy and configuration of the system reached equilibrium. Thus, the energetically stable configuration was obtained. In the experiment, the Gr layer has a finite size, and it contains edges as well as cracks induced by the wet transfer process, which serve as free edges. The atoms of upper Gr within 0.3 nm from the outermost sides were removed to stimulate the free edges while keeping the PBC for the simulation box. This method sets the free-edge boundary to the

upper Gr while the lower Gr is still in PBC. Then, the system was relaxed using the same method until equilibrium.

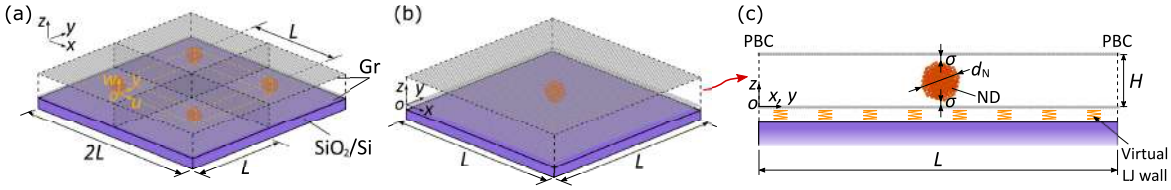

Fig. 4.2 Schematic representation of the simulation system. The system contains two square Gr layers and NDs sandwiched between them. (a) A system with four NDs arranged in the square lattice with equal distances of L. Thus, the system with a side length of $2L$ consists of four unit cells. A cube enclosed by orange dashed lines represents the system of the continuum model. The origin is set on the lower Gr, directly beneath an ND at the cube corner, and u, v, and w are the displacements in the x, y, and z directions, respectively. (b) The 3D view of a Gr/ND/Gr unit cell. The side length of the Gr is L, which equals the inter-ND distance. The origin point of molecular dynamics (MD) simulation is at the corner of the unit cell on the lower Gr layer. The in-plane x and y directions are set with periodic boundary conditions (PBC). (c) Side view of the unit cell in (b). The diameter of ND is d_{N}. The initial distance between the two Gr layers is $H = d_{\mathrm{N}} + 2\sigma$. The systems with different Gr sizes L and ND diameters d_{N} are simulated.

In this study, a continuum model was also developed on the basis of the elastic theory to expand simulation sizes and align with experimental scales. Although MD simulations can capture the microstructure of the Gr–ND system, computational costs limit the system's scale. For example, a system with $d_{\mathrm{N}} = 2.0$ nm and $L = 100$ nm contains approximately 770,000 atoms. Scaling up to match experimental conditions, such as $L = 500$ nm, would require approximately 19,000,000 atoms. Therefore, the continuum model bridges theoretical simulations to experimental scales. The detailed model derivation is presented in 4.5.

4.3 Raman analysis of stacked graphene with NDs

Raman spectroscopy first validates the reduction of the interlayer interaction of Gr by ND insertion (Figure 4.3). Typical Raman spectra of monolayer Gr exhibit the D peak (~ 1350 cm^{-1}), G peak (~ 1580 cm^{-1}), and G$'$ peak (~ 2700 cm^{-1}) [141]. The D peak results from the breathing mode of six-membered rings, and it is sensitive to crystal defects [141]. The G peak refers to optical phonons at the Brillouin zone center, corresponding to in-plane stretching vibrations of carbon atoms. This band becomes more intense with the increase of layer number because more carbon atoms contribute to this vibration mode [143, 144]. The G$'$ peak is the overtone of the D peak [141], but its intensity is not related

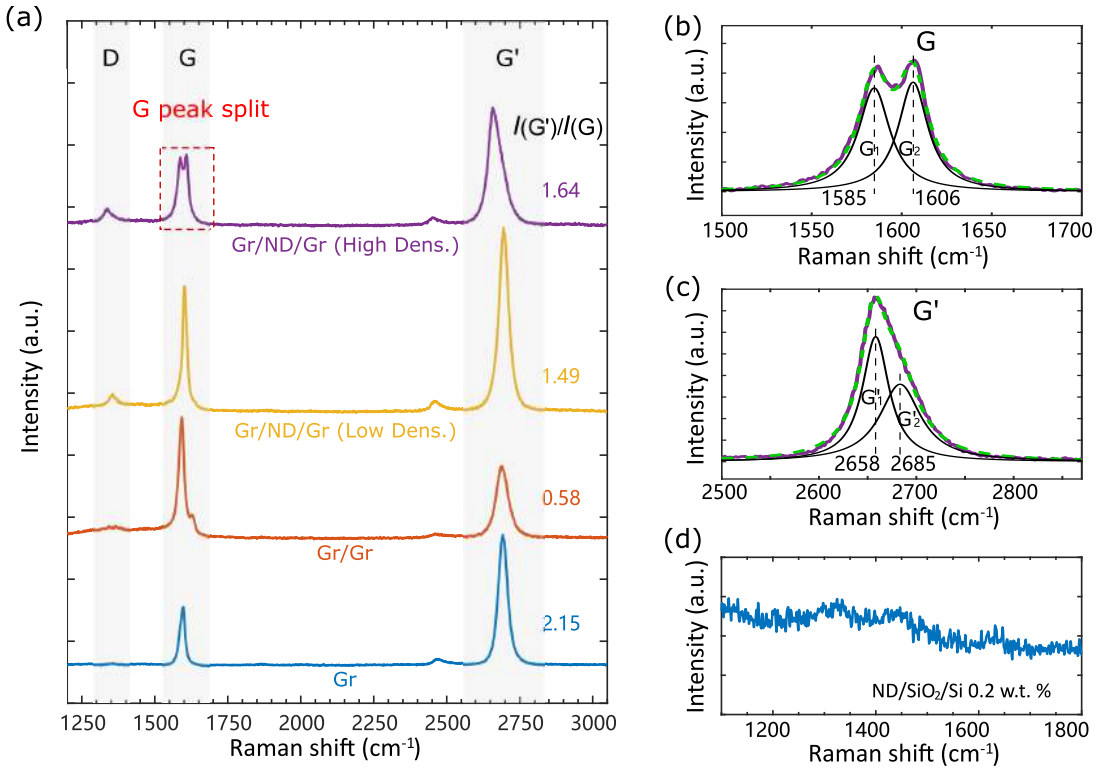

Fig. 4.3 (a) Raman spectra of Gr (blue), Gr/Gr (red), Gr/ND/Gr with low (yellow) and high area densities (purple). Representative spectra obtained from a single measurement point are shown for each sample. The split G peak (b) and asymmetric G′ peak (c) are fitted with two peaks, which are labeled as G_1 & G_2 and G'_1 & G'_2, respectively. (d) Raman spectrum of ND on SiO_2/Si substrate of 0.2 w.t.%. The minor signal from NDs verifies the negligible effect on the Raman spectrum of Gr-ND stacking structures.

to the defect. The relative intensity and peak shape are sensitive to the Gr layer number and stacking order [145, 19, 169]. For monolayer Gr, the intensity ratio of the G′ peak to the G peak ($I(\mathrm{G}')/I(\mathrm{G})$) is generally 2–4 with a single Lorentzian peak [145, 19, 146, 110]. Thermal annealing can decrease the $I(\mathrm{G}')/I(\mathrm{G})$ because of the doping effect [166–168]. The $I(\mathrm{G}')/I(\mathrm{G})$ ratio decreases with the increase of the layer number of the AB stacked multilayer Gr because of the strong interlayer interaction and altered band structure with parabolic dispersion. A relatively high $I(\mathrm{G}')/I(\mathrm{G})$ ratio can be observed in the randomly stacked multilayer Gr [141, 147, 148]. In randomly stacked Gr, the interlayer interaction is weaker than that of the AB stacked Gr, and the interlayer distance is slightly larger [75]. The band structure of the randomly stacked Gr resembles that of the monolayer Gr with linear dispersion [105, 106]. In the sample, the monolayer Gr shows $I(\mathrm{G}')/I(\mathrm{G}) = 2.15$, which is consistent with the typical value. The intensity ratio of the D peak to the G peak ($I(\mathrm{D})/I(\mathrm{G})$) is 0.06 for monolayer Gr, with an estimated defect density of $1.42 \times 10^2\ \mu\mathrm{m}^{-2}$ [142]. The $I(\mathrm{G})/I(\mathrm{Si})$ of bilayer Gr (Gr/Gr) doubles that of Gr with increased layer number. The $I(\mathrm{G}')/I(\mathrm{G})$ remarkably decreases to 0.58, and the G′ peak is symmetric which differs from those in Gr/Gr with AB stacking [145]. The decreased $I(\mathrm{G}')/I(\mathrm{G})$ indicates a strong interlayer interaction. In the present work, the Gr is polycrystalline, and the stacking direction is not controlled, resulting in the random stacking of Gr/Gr and the occurrence of a symmetric G′ peak [141]. The bilayer stacking structures with ND (Gr/ND/Gr) of two different areal densities are measured. For the one-point measurement of low-density Gr/ND/Gr, $I(\mathrm{G}')/I(\mathrm{G}) = 1.49$, which is higher than that of two directly stacked Gr layers. The high-density Gr/ND/Gr further increases the ratio $I(\mathrm{G}')/I(\mathrm{G}) = 1.64$. This result demonstrates a reduction in interlayer interaction in the Gr/ND/Gr structure because of ND insertion. The Raman signal from ND is faint, and it will not affect the measurement of Gr. The G peak shows a split (Figure 4.3b), with one peak located at approximately 1585 cm^{-1} (G_1) and the other at approximately 1606 cm^{-1} (G_2), with a difference of 21 cm^{-1}. A similar G split was reported and attributed to the different doping environments in intercalated Gr layers [71, 73]. The shape of the G′ peak is asymmetric for high-density Gr/ND/Gr (Figure 4.3c). The peak is the superposition of the signal from upper and lower Gr, which is fitted by two peaks (G'_1 and G'_2). A difference of $\sim 27\ \mathrm{cm}^{-1}$ is observed. Different doping environments and strains can induce different values of subpeak shifts and cause asymmetric G′ peak. Multi-point measurement is necessary to clarify the two factors, which will be discussed later.

Multi-point measurement of different positions in samples was further conducted (Figure 4.4a). The intensity ratio of the G peak normalized to the substrate silicon peak at 520 $\mathrm{cm}^{\check{}1}$ ($I(\mathrm{G})/I(\mathrm{Si})$) was used to evaluate the layer number of Gr. The increase in $I(\mathrm{G})/I(\mathrm{Si})$ indicates the increase of layer number from monolayer Gr to Gr/Gr and Gr/ND/Gr. Based on

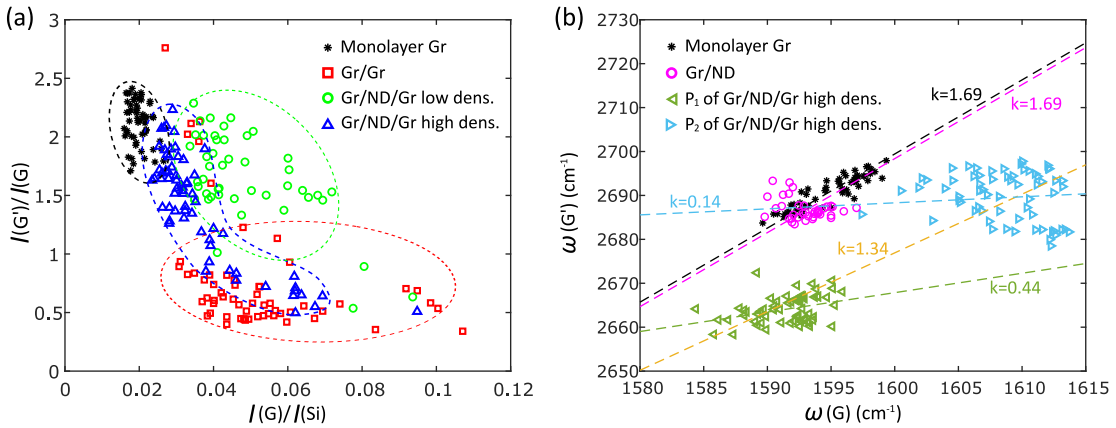

Fig. 4.4 (a) Distribution of $I(\mathrm{G}')/I(\mathrm{G})$ and $I(\mathrm{G})/I(\mathrm{Si})$ for monolayer Gr (black star), Gr/Gr (red square), and Gr/ND/Gr with low (green circle) and high densities (blue triangle). (b) Distribution of the G peak ($\omega(\mathrm{G})$) and G′ peak ($\omega(\mathrm{G}')$) positions. In particular, black stars represent Gr; magenta circles represent Gr/ND of high density, and green left-pointing triangles and cyan right-pointing triangles represent the fitted peaks (P_1 and P_2) from high-density Gr/ND/Gr. Dashed lines with the same colors as the points indicate the corresponding linear fitting of $\omega(\mathrm{G})$ versus $\omega(\mathrm{G}')$ with slopes $k = \partial\omega(\mathrm{G}')/\partial\omega(\mathrm{G})$. The yellow dashed line is fitted from points of P_1 and P_2, *i.e.* green and cyan triangles.

previous research, $I(\mathrm{G})/I(\mathrm{Si})$ increases linearly with the number of layers in the mechanically exfoliated multilayer Gr of AB stacking [170]. The $I(\mathrm{G})/I(\mathrm{Si})$ of monolayer Gr is ~ 0.02, but a wide distribution of 0.03–0.1 is obtained from Gr/Gr. In the present work, the multilayer Gr is stacked from polycrystalline CVD Gr with randomly oriented grains. Previous studies have found that in randomly stacking bilayer Gr [147, 171], a phonon resonance enhancement and an increase in G peak intensity are observed when the twist angle $\sim 12°$. The randomly stacking order causes the wide distribution of $I(\mathrm{G})/I(\mathrm{Si})$. Comparing Gr/Gr and Gr/ND/Gr with different ND densities, lower values of $I(\mathrm{G})/I(\mathrm{Si})$ were observed with the increase of density. Previous studies observed a weaker G peak in suspended Gr compared with Gr on a $\mathrm{SiO_2/Si}$ substrate, which is attributed to the effect of $\mathrm{SiO_2/Si}$ substrate interference enhancement [170, 149]. As the upper Gr supported by NDs is partially suspended, the interference enhancement of the Si substrate is weakened. The ND nanospacer of higher density separates larger parts of the Gr layers, which leads to a lower value of $I(\mathrm{G})/I(\mathrm{Si})$. The increase in $I(\mathrm{G}')/I(\mathrm{G})$ is observed in Gr/ND/Gr for low and high densities, which confirms the decreased interlayer interaction.

Multi-point measurement was conducted to analyze the G peak splitting and the effects of doping (Figure 4.4b). The G peak and G′ peak were fitted with two sub-peaks (Figure 4.3b,c). The sub-peaks with lower wavenumbers (P_1) are labeled as G_1 and G'_1, and the

sub-peaks with higher wavenumbers (P_2) are labeled as G_2 and G_2'. The peaks G_1 and G_1' are excited from the same Gr layer, whereas the peaks G_2 and G_2' are excited from the other layer. Linear regression analysis was conducted for the relation between the positions of the G peak ($\omega(G)$) and G′ peak ($\omega(G')$), and the fitted slope $k = \partial\omega(G')/\partial\omega(G)$ is shown in Figure 4.4b. Previous research demonstrated that k can separate the strain and charge doping in Gr [172]. Strain can induce $k = 2.02$, whereas charge doping can induce $k = 0.75$ [172]. The monolayer Gr conforms well to the linear relation with $k = 1.69$ (Figure 4.4b). Therefore, strain is the primary factor influencing the positions of the G and G′ peaks. The monolayer Gr with ND coating (Gr/ND) yields the same slope with a minor right shift comparing the monolayer Gr without ND. A feeble doping effect is induced by ND spreading on the Gr. The high-density Gr/ND/Gr sample shows evident peak shifts. By fitting the points of P_1 and P_2 together (yellow dashed line in Figure 4.4b), a downshift of $\omega(G)$ and $\omega(G')$ from P_2 to P_1 is induced by the strain with $k = 1.34$ [172]. Based on the simulation results in the later text, the upper Gr is suspended, and it can yield a bending and stretching deformation strain caused by vdW adhesion between two Gr layers, whereas the SiO_2/Si substrate constrains the deformation of the lower Gr. Stretching deformation will cause the downshift of G and G′ peak [173]. Thus, P_1 is the signal of upper Gr, and P_2 is excited by lower Gr. Based on the G peak shift between G_1 and G_2 ($\Delta\omega(G) = \omega(G_2) - \omega(G_1) = 17\ cm^{-1}$), the estimated strain in the upper Gr is 0.63% [173]. The Raman imaging is also conducted, but the spatial resolution is not sufficient to analyze the distribution of strain for upper Gr (see Figure S3). The tip-enhanced Raman spectroscopy will be a feasible solution with a resolution of nanoscale. By fitting P_1 and P_2 separately (green and blue dashed lines in Figure 4.4b), small slopes were obtained (0.44 for P_1 and 0.14 for P_2), indicating that both Gr layers are subject to strong doping effects. Such strong doping is attributed to annealing after transferring the second Gr. Annealing results in a tighter integration between Gr and ND, thereby making the doping effects more pronounced. The doping environment is different for the lower and upper Gr. The upper Gr is suspended and only doped by ND with $k = 0.44$, whereas the lower Gr is doped by ND and the SiO_2/Si substrate with a lower slope of $k = 0.14$.

4.4 Nanostructure analysis with atomic force microscope

The microstructural difference of ND insertion was studied to clarify the reduction of interlayer interaction. AFM was conducted to analyze the microstructure of the samples (Figure 4.5). The distribution of NDs on the Gr surface (Gr/ND) is first evaluated (Figures 4.5a,b). The distribution of ND is nearly random and uniform. The areal density of low-density ND is approximately $\sim 47.5\ /\mu m^2$. In the case of high ND density, the distribution

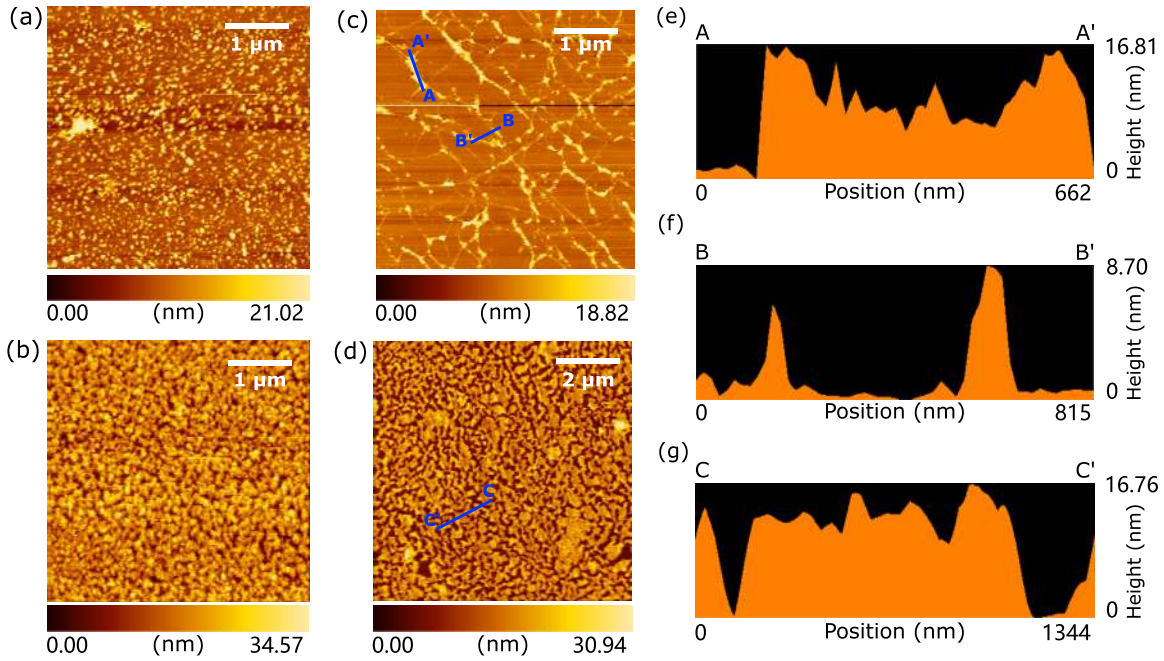

Fig. 4.5 AFM observation of Gr/ND and Gr/ND/Gr. (a, b) AFM images of Gr/ND with low (a) and high (b) ND densities. (c, d) AFM images of Gr/ND/Gr with low (c) and high (d) ND densities. (e, f) Cross-sectional profiles of Gr/ND/Gr along (e) and across (f) the wrinkle indicated by $A - A'$ and $B - B'$ in (c), respectively. The wrinkles are supported by low-density NDs. (g) Cross-sectional profile ($C - C'$) of Gr/ND/Gr with high-density NDs. Comparable morphologies of MD simulations are shown in Figure 4.6j-l.

of ND is so dense that AFM cannot separate two adjacent NDs. The areal density is assumed to be $\sim 475\ /\mu m^2$ because the concentration of ND dispersion is 10 times higher. For the most part, the NDs are monolayered with few areas of overlap. The AFM images of the Gr/ND/Gr with low and high densities are shown in Figures 4.5c and d, respectively. AFM indicates that low-density Gr/ND/Gr has a morphology with many wrinkles. The height of the wrinkles is ~ 18 nm, which matches the size of NDs. Figure 4.5e and f show the cross-sectional images along and across the wrinkles. In the cross-section along the wrinkled ridge, the upper Gr is supported by the NDs with a higher interlayer distance (Figure 4.5e). The cross-section perpendicular to the wrinkles reveals that the upper Gr adheres to the lower layer between them (Figure 4.5f). The AFM image of high-density Gr/ND/Gr shows a plateau-like morphology (Figure 4.5g). The increased ND density can provide better support to upper Gr. More parts of Gr are supported, and the plateau morphology appears. A theoretical study has reported that increasing the interlayer distance can weaken interlayer coupling and alter the band structure of multilayer Gr, comparable to that of a single layer with linear dispersion [106]. NDs induce the partial suspension of Gr, thereby increasing the interlayer distance. This finding explains the observed reduction of interlayer interactions in Raman spectroscopy (Figure 4.3 and 4.4). In high-density Gr/ND/Gr, the ND fully separates Gr layers with upper layer suspension. The $I(G')/I(G)$ obviously increases with G′ peak splitting. When the two layers of Gr are sufficiently separated, the stacking angle no longer significantly affects the interlayer interaction. The separated Gr layers have band structure resembles the monolayer Gr and benefit the application in photonics. In twisted stacked Gr, there are still domains with AB and AA stacking [70]. For low-density Gr/ND/Gr, there is also a relatively weak increase in the $I(G')/I(G)$. The NDs only support the Gr near the wrinkles. The supported area is smaller than the high-density Gr/ND/Gr. Hence, the effect of reduction in interlayer interaction is weaker with relatively lower $I(G')/I(G)$.

The support provided by NDs to Gr can be analogous to the pillar-supported Gr in previous work [174–176]. The nanopillars in previous works are obtained by lithography methods. Compared to nanopillars, the lateral spacing of NDs can be adjusted by simply changing the solution concentration for higher density. The NDs with different sizes are also comparable with the pillars of different heights. Previous work observed pseudomagnetic fields at Gr wrinkles using scanning tunneling spectroscopy (STS). AFM images show that wrinkles caused by low-density ND, with widths in the nanometer range, are also promising structures for such phenomena [177, 178]. Notably, defects [179, 180, 129, 181, 182] and thermal fluctuations [102] can also cause ripples. However, these differ from the wrinkles caused by ND in terms of geometric size and morphology. The height and width of wrinkles or ripples due to defects and thermal fluctuations are ~ 1 nm, which is smaller than the

typical size of wrinkles caused by ND. Wrinkles may also appear due to the capillary effect in wet transfer. The wrinkles have a height of 1–3 nm [102], which is smaller than the diameter of NDs. The spacing effect from wrinkles is minor. The dry transfer method is an alternative [159]. The choice of method depends on the specific requirements. The wet transfer method allows for larger sample areas of 1 cm with the disadvantage of PMMA residues and wrinkles. The dry transfer method permits operations on SiO_2/Si and can quickly achieve multilayer structures with a smaller sample area of $\sim 300\ \mu$m and fewer wrinkles.

4.5 Continuum Model

According to the MD simulation, deformation primarily occurs in upper Gr. The appearance of two different configurations is determined by the energy difference, mainly the deformation energy of Gr (corresponding to the AIREBO energy in MD simulations) and the interlayer vdW energy (LJ potential). For the suspension configuration, the upper Gr remains flat, resulting in lower deformation energy. A larger interlayer distance leads to an increase in vdW energy. In the adhesion configuration, considerable deformation occurs in the upper Gr, thereby increasing the deformation energy. However, the interlayer distance approaches 0.34 nm, and the vdW energy decreases to a minimum. In the continuum theory, the deformation energy matches the elastic energy and the interlayer vdW energy can be integrated into the adhesion energy. In investigating the energy-stable configurations determined by two energy components and bringing theoretical analysis closer to experimental scales, a continuum model was proposed based on the theory of elasticity.

The model is shown in Figure 4.2a. One unit cell with four NDs at the corner parts was investigated for an easier description of the boundary condition. The system is identical to the MD system after shifting by a length of L/2 in the x and y directions, and the origin is set on the lower Gr, directly beneath an ND at the cube corner (Figure 4.2a). The Gr is square with a side length of L, and the interlayer distance of the upper and lower Gr is equal to H in the initial configuration. The two adjacent sides in the in-plane direction are the x and the y axes. The direction vertical to the surface is the z direction. The u and v are the in-plane displacements, and w is the out-of-plane displacements, *i.e.* deflection. The interlayer distance is related to deflection by $h = w + H$ and the out-of-plane coordinate $z = h$.

The total energy U_{tot} of the system is expressed as follows:

$$\begin{aligned} U_{\mathrm{tot}} &= U_{\mathrm{ela}} + U_{\mathrm{vdW}}, \\ U_{\mathrm{ela}} &= U_{\mathrm{b}} + U_{\mathrm{m}}, \end{aligned} \tag{4.2}$$

where U_{vdW} is the integrated vdW energy that causes the interlayer adhesion. U_{ela} is the elastic energy from the upper Gr deformation, which has two components, bending energy U_{b} and membrane energy U_{m} [183, 184]. In the microscopic view, the membrane energy corresponds to the elongation and shortening of chemical bonds, and the bending energy corresponds to the rotation of chemical bonds and changes in bond angles.

According to the theory of two-dimensional (2D) membranes [113], the membrane energy U_{m} and bending energy U_{b} are expressed as follows:

$$\begin{aligned} U_m &= \int_S \frac{C_{2\mathrm{D}}}{2}\left[\nu\left(\mathrm{Tr}\varepsilon\right)^2 + \left(1-\nu\right)\varepsilon:\varepsilon\right]\mathrm{d}S, \\ U_b &= \int_S \frac{M_b}{2}\left[\nu\left(\mathrm{Tr}\kappa\right)^2 + \left(1-\nu\right)\kappa:\kappa\right]\mathrm{d}S, \end{aligned} \tag{4.3}$$

where the tensile strain ε describes the in-plane deformation of Gr, and the curvature κ describes the out-of-plane bending configuration. Here, “Tr" is the trace of a matrix and a colon, and “:" defines the double-dot product of two matrices. The strain tensor ε and curvature κ have a geometric relation with the in-plane displacement u, v and out-of-plane deflection w [183]. The strain tensor ε is expressed as follows:

$$\varepsilon = \begin{bmatrix} u_{,x} + \frac{1}{2}w_{,x}w_{,x} & \frac{1}{2}\left(u_{,y} + v_{,x}\right) + \frac{1}{2}w_{,x}w_{,y} \\ \frac{1}{2}\left(v_{,x} + u_{,y}\right) + \frac{1}{2}w_{,x}w_{,y} & v_{,y} + \frac{1}{2}w_{,y}w_{,y} \end{bmatrix}, \tag{4.4}$$

and the curvature κ writes

$$\kappa = -\begin{bmatrix} w_{,xx} & w_{,xy} \\ w_{,xy} & w_{,yy} \end{bmatrix}, \tag{4.5}$$

where a comma “," in subscript denotes a partial derivative. The elastic constants, 2D elastic modulus $C_{2\mathrm{D}}$, bending stiffness M_b, and Poisson’s ratio ν can be determined by experimental measurement [113, 13, 185] and first-principle simulation [184, 186]. Here, $C_{2\mathrm{D}} = 2241$ eV/nm^2 [13], $M_b = 1.44$ eV [184], and $\nu = 0.16$ [13].

The vdW energy of the upper Gr can be calculated by integrating the vdW energy density in the unit area

$$U_{\mathrm{vdW}} = \int_S \pi\rho_a^2\left[\frac{4\xi\sigma^{12}}{5h^{10}} - \frac{4\xi\sigma^6}{2h^4}\right]\mathrm{d}S. \tag{4.6}$$

The same ξ and σ are taken as MD simulation, and $\rho_a = 38.02/\mathrm{nm}^2$ is the areal density of C atoms in the Gr layers [184]. The integrand in the above formula describes the interaction among atoms per unit area of the upper Gr and the infinitely large lower Gr layer. Such energy expression is obtained by integration operations from the LJ pairwise potential in Eq. 5.1 using Hamaker summation [133]. Thus, Eq. 4.6 describes the total vdW energy between

the upper and lower Gr as a function of the distance h with $h = w + H$. The parameters are equivalent to the adhesion energy of 0.28 J/m^2 and interlayer distance of 0.34 nm, which are comparable to the value from experiment [187, 188].

With the disregard of ND deformation, the boundary condition is expressed as follows:

$$\begin{cases} u(0,\ y) = 0,\ u(L,\ y) = 0,\ v(x,\ 0) = 0,\ v(x,\ L) = 0, \\ w(0,\ 0) = 0,\ w(L,\ 0) = 0,\ w(0,\ L) = 0,\ w(L,\ L) = 0, \\ w_{,x}(0,\ y) = 0,\ w_{,x}(L,\ y) = 0,\ w_{,y}(x,\ 0) = 0,\ w_{,y}(x,\ L) = 0. \end{cases} \tag{4.7}$$

Displacement is expanded in the Fourier series,

$$\begin{aligned} u &= \sum_{m=1}^{M}\sum_{n=1}^{N} A_{mn} \sin(m\pi x/L) \sin(n\pi y/L), \\ v &= \sum_{m=1}^{M}\sum_{n=1}^{N} B_{mn} \sin(m\pi x/L) \sin(n\pi y/L), \\ w &= \sum_{m=1}^{M} C_{m0} (\cos(m\pi x/L) - 1) + \sum_{n=1}^{N} C_{n0} (\cos(n\pi y/L) - 1) \\ &\quad + \sum_{m=1}^{M}\sum_{n=1}^{N} C_{mn} (\cos(m\pi x/L) - 1)(\cos(n\pi y/L) - 1). \end{aligned} \tag{4.8}$$

The coefficients $A_{mn}, B_{mn}, C_{m0}, C_{n0}$, and C_{mn} are treated as variational parameters to minimize the energy. The order of the series is set to be $M = 20, N = 20$ considering the computational precision and efficiency. The energy minimization process on MATLAB utilizes the quasi-Newton method [189]. The calculation is conducted on a desktop PC instead of MD simulations in a supercomputer. The cases with different d_{N} and L are calculated to find the L_{cri}.

4.6 Simulation of micro-structure with molecular dynamics and continuum model

MD simulations of the Gr–ND stacking structure were conducted to investigate the influencing factors of ND in detail and to study the microstructure comparatively with AFM observation. MD simulation allows more convenient control of the diameter and area density compared with the experiment of NDs. The intuitive microstructure figures can be output at a low cost compared with sample fabrication and AFM scanning. Figure 4.6a-c shows three examples of MD simulation with different ND diameters d_{N} and inter-ND distance L. The

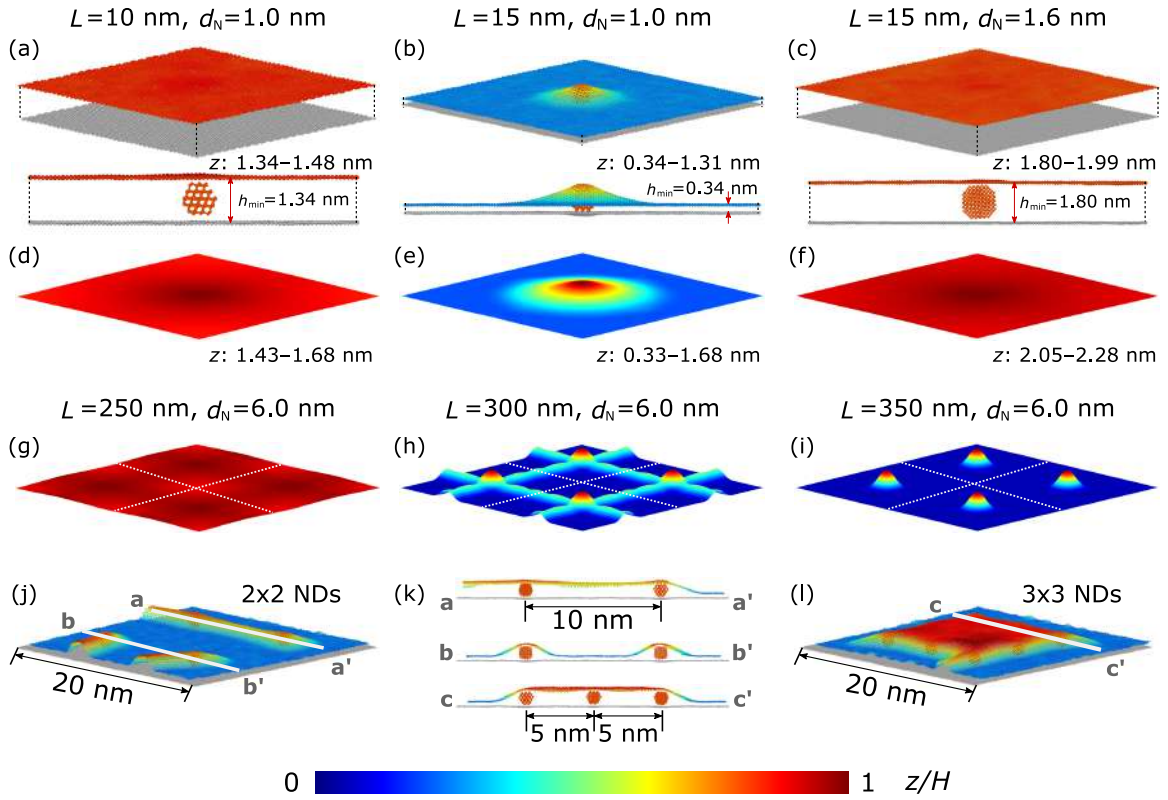

Fig. 4.6 Deformed configuration obtained by MD simulation (a–c) and continuum model (d–f) of the Gr–ND stacking structure with different ND diameters d_N and Gr side length (inter-ND distance) L. (a, d) $d_N = 1.0$ nm and $L = 10$ nm. (b, e) $d_N = 1.0$ nm and $L = 15$ nm. (c, f) $d_N = 1.6$ nm and $L = 15$ nm. The range of actual z-axis coordinates of the upper Gr layer is listed beside the figures. (g–i) Deformed configurations obtained by the continuum model for larger d_N. Four unit cells are plotted, indicated by the white dot lines. (j–l) Configurations of MD simulation with free edges. The sizes of the Gr layers are 20 nm, and d_N is 1.0 nm. (j) Four NDs are encapsulated with a distance of 10 nm. (l) Nine NDs are encapsulated with a distance of 5 nm, and the size of Gr is maintained at 20 nm. (k) The cross-sections $a - a'$ and $b - b'$ are captured from (j). The cross-section $c - c'$ is captured from (l). The wrinkle and plateau morphologies are comparable to the AFM images shown in Figure 4.5e–g. The color of the upper Gr layer represents the dimensionless z-coordinate z/H of each atom of upper Gr in MD simulations or each point in the model. The minimum z-coordinate ($z/H = 0$) is represented by blue, and the maximum z-coordinate ($z/H = 1$) is represented by red. The color bar is at the bottom of the figure.

areal density of ND can be calculated by $1/L^2$. The colors in Figure 4.6 represent the z-axis coordinates of the atoms. The coordinates are dimensionless to normalize the results for different ND diameters with z/H. In the first case with $d_N = 1.0$ nm and $L = 10$ nm (Figure 4.6a), the upper Gr is suspended with the support of the ND after relaxation, but it slightly decreases in the z-coordinate compared with the initial distance H with fluctuation, which is due to the vdW attraction between the layers. If the distance is increased to $L = 15$ nm and d_N keeps 1.0 nm (Figure 4.6b), then the upper Gr adheres to the lower layer with the yurt-like deformation covering the ND. The interlayer distance of the two Gr layers is 0.34 nm, which is close to the spacing of carbon layers in graphite. If the distance L is fixed and d_N increases to 1.6 nm (Figure 4.6c), then the upper Gr stays in suspension, which is similar to the first case. The consistent result of the system with one ND and four NDs confirms the validity of PBCs and the negligible influence of the size of supercells. Thus, the one-ND system is selected for further simulation to reduce the time cost.

During the relaxation process, deformation primarily occurs on the upper Gr layer, whereas the lower layer remains flat. The change in potential energy is primarily due to the deformation energy of the upper Gr layer and the variation in interlayer vdW energy [159]. Considering the two energy components, a continuum model was further developed based on the elastic theory. The model expands the simulation sizes and aligns with experimental scales with less computational costs. The results of the continuum model with the same L and d_N as the MD simulations are shown in Figure 4.6d–f. Similar morphologies were obtained from the two methods. The range of z-coordinates for the upper Gr obtained from the continuum model is slightly higher than that from MD simulations because the distance between the upper and lower Gr is fixed ($w = 0$) at the location above ND in the continuum model. However, Gr is not constrained in MD simulations, and the upper Gr experiences an overall downward displacement under the vdW interaction. The continuum model calculates the cases with d_N = 6.0 nm, which is comparable to ND in experiments (Figures 4.6g–i). For $L = 250$ nm in Figure 4.6g, the upper Gr is suspended with the support of NDs. With the increase of L to 300 nm, the suspended Gr initially adheres to lower Gr with the appearance of wrinkles (cyan ridges in Figure 4.6h). A single ND can influence and support the surrounding Gr. When the inter-ND distance is relatively small, the influence range of NDs overlaps, thereby creating wrinkle-like structures connecting the NDs. As the inter-ND distance L increases to 350 nm (Figure 4.6i), the influence range of NDs cannot overlap. The ND can only support the Gr around with a protrusion structure. The continuum model can also calculate the distribution of strain. For the suspension configuration, the upper Gr is almost flat and the deformation strain is negligible ($\varepsilon_{11} = 5 \times 10^{-7}$). In Raman spectroscopy, a strain of 6.3×10^{-3} is observed. The diameter of NDs is not completely identical in real

experiments which could cause undulations and deforms on suspended upper Gr. For the wrinkle and adhesion configurations, the local deformation of wrinkles and protrusions leads to the obvious concentrated strain of $\sim 9 \times 10^{-3}$ and $\sim 1.6 \times 10^{-2}$ respectively, which is higher than the value of suspended Gr.

To better reproduce the experiment, additional MD simulations were conducted with Gr of finite sizes and free edges. The configuration (Figures 4.6j–l) is qualitatively comparable to AFM observation (Figures 4.5c–g). The two cases presented in Figure 4.6j and l have the same free-edge boundaries and Gr sizes. The Gr/ND/Gr with four NDs yields an interlayer adhesion with wrinkles (Figure 4.6j), which resembles the AFM image of lower ND density (Figure 4.5c). The cross-sections along (a–a′) and across (b–b′) the wrinkles in Figure 4.6k resemble the cross-sections from the AFM image (Figures 4.5e and f). When nine NDs are in the system, *i.e.* higher ND density, a plateau-like morphology is observed, indicating upper Gr suspension (Figure 4.6l), which is consistent with the results shown in Figure 4.5d. The cross-section (c–c′) in Figure 4.6k also resembles the cross-section from the AFM image (Figure 4.5g).

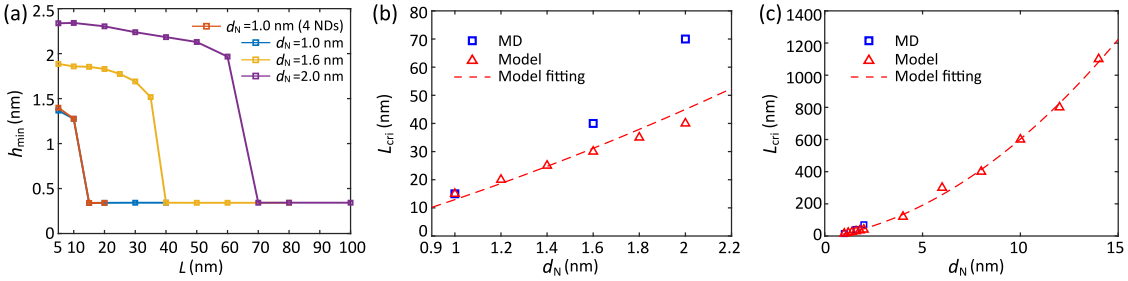

Fig. 4.7 (a) Effect of the ND diameter d_N and distance L on the minimum interlayer distance h_{min} by MD simulation. The Gr/ND/Gr with one ND are plotted as blue (d_N = 1.0 nm), yellow (d_N = 1.6 nm), and purple (d_N = 2.0 nm) squares with lines. The four-ND cases with d_N = 1.0 nm are plotted as red squares with lines. (b) The critical inter-ND distance (L_{cri}), where the adhesion configuration first appears, as a function of the ND diameter d_N. The blue squares and red triangles indicate the MD and continuum model results, respectively. (c) Prediction of L_{cri} from the continuum model for d_N in 1–14 nm (red triangles). The red dashed line is fitted with a quadratic function ($L_{cri} = 4.2d_N^2 + 19.5d_N - 10.8$) in (b) and (c).

Additional simulations were performed with different d_N and L (Figure 4.7). The final configurations are classified into two categories: upper Gr suspension and interlayer adhesion. The minimum interlayer distance h_{min} can be used to distinguish between the two configurations, which is calculated by averaging the distance between the Gr layers at the four corners. Comparing the cases of MD simulation with the same d_N (Figure 4.7a), h_{min} approaches the initial spacing H for small L, indicating that the upper Gr remains suspended. As L gradually

increases and surpasses a critical value, the interlayer distance abruptly decreases to 0.34 nm, indicating the occurrence of interlayer adhesion. The identical result of the systems with one ND and four NDs for $d_N = 1.0$ (red and blue squares in Figure 4.7a) further verifies the validity of PBC. The interlayer distance h_{min} in the suspended Gr configuration increases with the diameter d_N. A large ND diameter also increases the critical inter-ND distance (L_{cri}) at which the adhesion configuration appears (Figure 4.7b). The prediction of L_{cri} from the continuum model is lower than the MD simulation. The difference could be induced by the numerical method. In MD simulation, the relaxation process is conducted with thermal vibrations of atoms. No extra force is imposed on the system to stimulate the system if the relaxation falls into a local minimum. The prediction of L_{cri} for large NDs is shown in Figure 4.7c. The points fit well with the quadratic function in the larger section for d_N. Based on the predictions of the continuum model, the L_{cri} for $d_N = 4$–14 nm is approximately 134–1085 nm, which is equivalent to an ND areal density of 0.8–55.7 $/\mu m^2$. In the high-density sample of the experiment, the areal density is assumed ~ 475 $/\mu m^2$, thereby causing the suspension of upper Gr, which is consistent with the prediction of simulation. In the low-density case, the areal density (~ 47.5 $/\mu m^2$) falls in the predicted section where adhesion can appear. Moreover, during the wet transfer of the second Gr layer, the ND can re-disperse and aggregate in the liquid phase, which makes the ND areal density lower than the AFM measurement. The real density is lower than the critical density for suspension, thereby promoting the formation of a wrinkled morphology. The current model effectively explains the experimental results but is unable to simulate the structures of randomly distributed and varying numbers of ND. Rapid advancements in machine learning in recent years provide feasible approaches, such as physics-informed neural networks [190] and machine learning-based coarse-grained intermolecular potentials [191, 192]. These methods can enhance the scale and efficiency of simulations, enabling the modeling of randomly distributed and varying numbers of ND.

Finally, ND and CNT nanospacers were compared, with ND showing advantages in various aspects [159]. From an experimental perspective, the diameter of ND is 4–14 nm, which is larger than the diameter of single-walled CNT (1–3 nm) in the previous work. A larger spacer size promotes the expansion of the interlayer distance [159]. The split of the G peak is observed in Gr/ND/Gr, indicating the sufficient separation of Gr layers [73]. The G peak from ND is minor, whereas the CNT exhibits a prominent G peak [159]. The G peak of CNT interferes with the signal from Gr, complicating the analysis of Raman peaks. The calculation results demonstrate the advantage of using large ND spacers. A 3-nm-diameter CNT achieves an L_{cri} of 141 nm, whereas with a larger ND of $d_N = 14$ nm, the L_{cri} reaches 1085 nm based on the continuum model. The calculated microstructure indicates a point-type

contact between ND and Gr, resulting in a smaller contact area than the line-shape contact of CNTs. This reduced contact area leads to less influence on the properties of the supported Gr.

4.7 Conclusion

In this study, the effect of ND insertion on the interlayer interaction in multilayer Gr was investigated. The stacking structure of Gr and ND is fabricated by using the layer-by-layer method in the experiment. Raman spectroscopy verifies the reduction of interlayer interaction with the increase in the intensity ratio of the G' peak to the G peak and the split of the G peak. AFM measurement confirms the increase in the interlayer distance. In addition, MD simulations are conducted to systematically study the influencing factors. The Gr–ND stacking structure exhibits two stable configurations: the upper Gr suspension and interlayer adhesion. The areal density and diameter of the NDs determine the selection of a stable morphology. By considering the energy difference between the two configurations, a continuum model that extends the simulation size to experimental conditions was developed. The model predicts the suspension and wrinkled morphologies and a critical ND density, which are qualitatively comparable to the results in experiments. The results of this study contribute to the improved and novel properties of multilayer Gr to facilitate functional enhancement for wider application fields.

Chapter 5

Property modulation of multilayer graphene with nanospacer insertion

5.1 Preface for this chapter

This chapter mainly investigates the effects of inserting nanospacers on the material properties. For the Gr-CNT structure, the focus is on mechanical behavior, while for the Gr-ND structure, the emphasis is on electrical properties.

Given the widespread application of Gr-CNT structures in strain sensors, a comprehensive understanding of the structural changes in these sensors at the micro-scale remains elusive. To address this gap, we conducted both simulation and experimental studies, extending the investigations from Chapter 3 on Gr-CNT structures, with a focus on elucidating the structural changes under compressive stress. As for the electrical properties of the Gr-CNT stacked structure, since CNTs are conductive, we do not focus on them.

5.2 Mechanical hysteresis and multistable of multilayer graphene with carbon nanotube

5.2.1 Background

The fabrication of graphene (Gr) and carbon nanotube (CNT) hybrid systems is widely reported[41, 40, 43, 81, 91, 90, 89]. The Gr is a revolutionary material, notable for its atomic thickness, exceptional electrical and thermal conductivity, as well as remarkable mechanical stiffness [40]. Adding CNTs can prevent Gr layers from re-stacking and offer a cross-linking effect. Thus, the Gr and CNT (Gr-CNT) hybrid system has further improvement

on the mechanical robustness with enhanced porosity, electrical properties, and superelastic characteristics [41, 78, 42, 40, 81]. The excellent properties enable Gr-CNT hybrid systems to find widespread applications across various fields. The porous structure with a high surface area makes the Gr-CNT hybrid system an ideal scaffold and adsorbent material for catalytic processes and water treatment[21, 37, 97]. Its excellent thermal and electrical conductivity further broadens its applications in supercapacitors[78, 92, 79], batteries[80], and thermal management[39]. Additionally, the flexibility and lightweight nature of the hybrid system make it well-suited for use in strain sensors[42, 43, 40, 81], artificial muscles, and dampers[41].

The microstructure of Gr-CNT hybrid systems significantly influences properties such as porosity and flexibility. The adhesion between graphene layers causes the monolayers to draw closer, forming stacked multilayers with strong interlayer coupling. CNT nanospacers can help separate the Gr layers. However, the single-atom layer structure of Gr results in its low stiffness to bending deformation. When the quantity or density of CNT nanospacers is insufficient, the Gr layers may still bend and adhere. Thus, negative factors including AB stacking, electron scattering, and a decrease in the surface-to-volume ratio will appear. Hence, it is necessary to investigate the microstructure of the Gr-CNT hybrid systems to better understand and optimize their interaction.

In previous studies, molecular dynamics (MD) was employed to investigate the mechanical properties of multilayer Gr-CNT stacking systems. The models were reasonably simplified from 3D-sponge to stacking structure due to the limitation of computational burden for all full atom simulations. The elastic constants of the multilayer Gr-CNT stacking system were studied [84]. The deformation of CNT encapsulated by two Gr layers is also studied theoretically [85]. The coarse-grained method was also implemented to study the fracture behavior of 3D sponges [193]. However, the influencing factors which can determine the separation of Gr layers, have not been systematically studied. The hysteresis of the loading-unloading curve is widely observed in previous experiments [41, 42, 40, 194]. Yet the theoretical analysis is insufficient. In our previous work, we studied the Gr-CNT on SiO_2/Si substrate with experiment and MD simulation[159]. However, the loading and multistable characteristics are not studied. The previous substate-supported boundary condition is different from the sponge structure in which the Gr layers and CNTs are nearly suspended.

In this study, we investigated the microstructure of a Gr-CNT stacking system by MD simulation. The energy-stable configuration is simulated which is affected by CNT radius, inter-tube distance, and wall number. The press loading-unloading curvature indicates the hysteresis behavior. The energy analysis unveils the multistable inherent property of the Gr-CNT stacking system.

5.2.2 Molecular dynamics simulation method

The simulation model is shown in Figure 5.1. Two CNTs were encapsulated between two Gr layers. The CNTs are parallel aligned with an inter-tube distance of L. The length of the Gr layers $a = 2L$ and the width of graphene layers $W = 6.7$ nm. The Gr interlayer distance of the initial configuration $H = d_c + 2\sigma$, where d_c is the diameter of the CNTs and σ is the interlayer distance between Gr layers in graphite. The periodic boundary condition (PBC) is added in the in-plane x and y directions of the simulation box so that the model can simulate the CNTs array aligned at equal distances of infinite length. The adaptive intermolecular reactive empirical bond order (AIREBO) potential[86] is used to describe the short-range interactions between carbon atoms. The long-range van der Waals (vdW) interactions between graphene layers and CNTs are described by the Lennard-Jones (LJ) potential

$$E_{\mathrm{LJ}} = 4\varepsilon\left(\frac{\sigma^{12}}{r^{12}} - \frac{\sigma^{6}}{r^{6}}\right) \tag{5.1}$$

where r is the distance between two atoms. The parameter ε is the depth of the potential well, and σ means the distance when the energy E_{LJ} is zero. The minimization point $E_{\mathrm{LJ}} = -\varepsilon$ appears at $r = \sqrt[6]{2}\sigma$, and $E_{\mathrm{LJ}} \to 0$ when $r \to \infty$. The balance distance between Gr layers in graphite also equals σ. Here, we take $\varepsilon = 0.00284$ eV and $\sigma = 0.34$ nm[86]. In MD simulation a cutoff radius r_{cutoff} is necessary for long-range interaction to reduce the burden of computation. In order to induce vdW interaction between the upper and lower graphene, we set the cutoff radius larger than the interlayer distance ($r_{\mathrm{cutoff}} > H$). The system is relaxed in the NVT ensemble with a temperature of 300 K and a time step of 1 fs. The energy and configuration of the system are output every 1000 steps in the relaxation process until stable to obtain the energy-favorable configuration. The MD simulation is conducted in the open source software, large-scale atomic/molecular massively parallel simulator (LAMMPS)[87].

The compressing behavior is also studied with the loading-unloading process. The press is imposed by adding a uniform force F on each atom of graphene layers (Figure 5.1c), which can simulate uniform pressure loading on Gr layers. The pressure writes $P = F/S_0$, where $S_0 = 0.026$ nm^2 is the planar areas of a carbon atom in a Gr layer. The loading process is carried out incrementally, with the force F increased step by step by 0.0016 nN. After each increment, the system is relaxed for 100 ps to obtain a stable structure.

5.2.3 Experimental verification method

The mechanical behavior of multilayer stacked graphene films was experimentally investigated by nano-indentation method for verification. Multilayer graphene films, both with

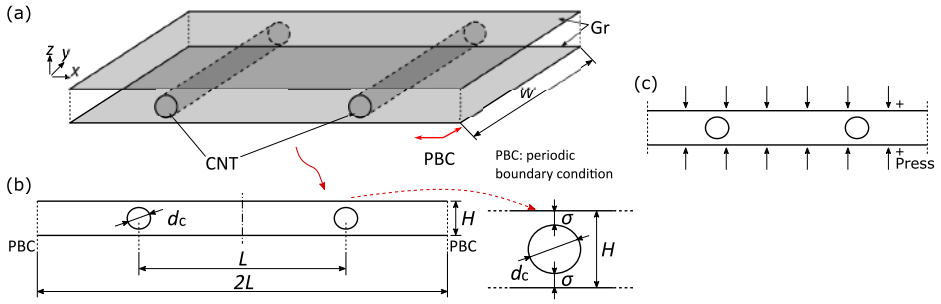

Fig. 5.1 Schematic representation of the simulation system in the three-dimensional view (a) and the front view (b). The system contains two graphene (Gr) layers and two carbon nanotubes (CNTs) aligned in parallel with the y direction. The width of the Gr is W, equal to the length of CNTs. The length of Gr is $2L$ in the x direction. The systems with different inter-tube distances L and diameters d_c are simulated. The initial distance between the two Gr layers is $H = d_c + 2\sigma$ as shown in the zoom-up figure. The in-plane x and y directions are set with periodic boundary conditions (PBCs). (c) The schematic of the loading press. The two sets of arrows indicate opposing forces being applied on the graphene layers.

and without CNTs, were fabricated and analyzed using the nanoindentation method. These films were prepared from graphene oxide (GO) suspension through a combination of vacuum filtration and high-temperature reduction. A 0.1 wt.% aqueous suspension of GO and a 0.1 wt.% aqueous suspension of CNTs (ZEONANO 02DS-WA-RD, average diameter 4 nm) were prepared. The GO and CNT suspensions were mixed at a mass ratio of 16:1 to form the GO-CNT suspension. Subsequently, GO and GO-CNT films were separately fabricated by vacuum filtering their respective suspensions. The filter membrane was removed by acetone and the GO and GO-CNT films were transferred on fused quartz substrates. The GO and GO-CNT films were reduced using a high-temperature reduction method with ethanol as the reducing agent. During the reduction process, ethanol and argon gases were introduced at flow rates of 2 sccm and 20 sccm, respectively. The reduction was conducted at a temperature of 1200°C for 1 hour under a pressure of 0.3 Torr.

The loading-unloading behavior of reduced GO (rGO) and rGO-CNT samples are measured by the indentation in the nanoscale. The nano-indentation experiment is realized by the AFM (Bruker, NanoWizard 3) combined with an inverted confocal microscope (Nikon, Ti2-E). By pressing the AFM probe downward to contact the sample and then lifting it upward, the loading-unloading curve of the sample surface can be obtained. On each sample surface, we performed force curve measurements at 32×2 points with a scanning area of 100×100 μm, obtaining the in-plane distribution of the force curves. The maximum indentation force is 300 nN. The work on AFM force curve measurements was carried out in collaboration with Assistant Professor Takahisa Matsuzaki and Nanami Sakurai.

5.2.4 Results and discussion

In hybrid systems of graphene and CNTs, it is always desirable for graphene to be fully dispersed into single layers. This increases the surface area ratio and enhances the performance of the material. The mixed ratio of the CNTs and graphene in the hybrid system significantly affects the microstructure, determining whether graphene can be adequately separated. Thus, we simulated the effect of inter-tube distance on the separation of graphene layers where a shorter inter-tube distance means a higher proportion of CNTs in the hybrid system. The CNTs with different diameters and wall numbers are also considered. The stable configurations after the relaxation of the Gr-CNT stacking structure are shown in Figure 5.2. In the first case with d_c = 0.68 nm and L = 10 nm (Figure 5.2a), the upper Gr is suspended between the CNTs. If the distance is increased to L = 20 nm (Figure 5.2b), then the graphene layers adhere together due to the vdW interaction. The interlayer distance of the two Gr layers is 0.34 nm, which is close to the spacing of carbon layers in graphite. If the distance L is fixed and d_c increases to 1.08 nm (Figure 5.2c), then the graphene layers are separated, which is similar to the first case. If the inter-tube distance L increases to L=35 nm (Figure 5.2d), the graphene layers also adhere with d_c = 1.08 nm. The vdW adhesion of the graphene layers induces pressure on the CNTs which makes the CNTs deform with ellipse cross sections. In Figure 5.2e, the CNTs are replaced by double-walled CNTs. The outer wall is the same as Figure 5.2c,d with chiral index (8, 8) and $d_c = 1.08$ nm. The inner wall is (3, 3) and d_c 0.41 nm. The double-walled CNT can separate the graphene layers. The deformation of the cross-section is also less obvious compared with the single-walled CNTs.

The stable configurations of the hybrid structure exhibit two distinct forms. The two configurations can be categorized into two types based on the final interlayer distance of the graphene, *i.e.*, separation and adhesion. The minimized interlayer distance $h_{\min}$ is calculated to distinguish between the separation and adhesion configurations (Figure 5.2). To quantitatively understand the impact of CNT parameters on the appearance of configurations, additional simulations with different CNT diameters d_c, CNT distances L, and wall numbers were conducted. For the case of the same d_c in Figure 5.3a, when the distance L is small, $h_{\min}$ approaches the initial spacing H, indicating that the graphene layers are fully separated. Thus, the interlayer distance $h_{\min}$ of separation configurations increases with the CNT diameter d_c (see different solid lines with circles in Figure 5.3a). As the inter-tube distance gradually increases and surpasses a critical value (L_{cri}), the interlayer distance abruptly decreases to 0.34 nm, indicating the occurrence of interlayer adhesion. A large CNT diameter can increase the critical inter-tube distance L_{cri} (Figure 5.3b). The vdW adhesion force decreases with increasing distance. In our initial configuration, the interlayer distance $H = d_c + 2\sigma$. Larger H can weaken the interlayer force and prevent the interlayer adhesion. It should be noted

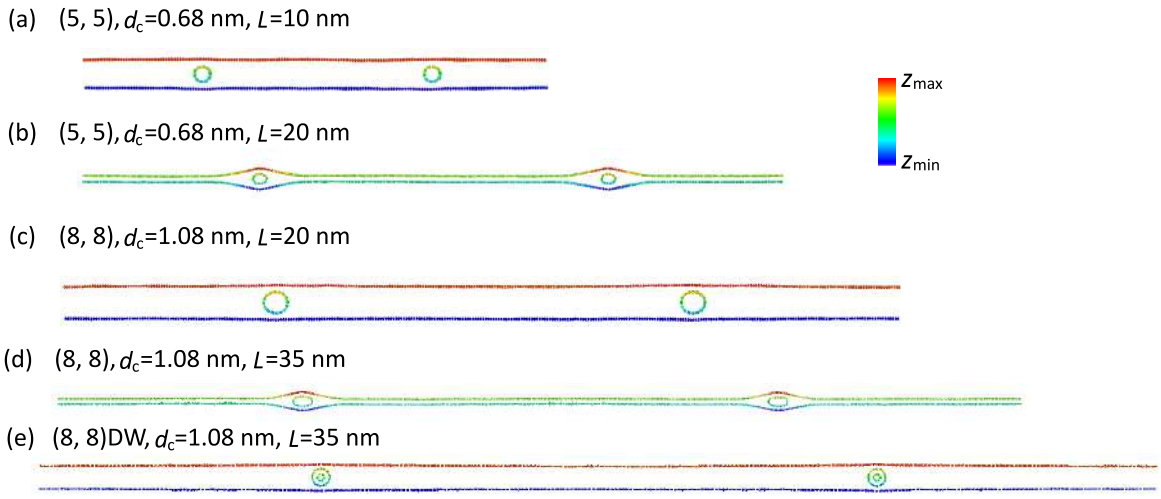

Fig. 5.2 Deformed configuration obtained by MD simulation of the Gr-CNT stacking structure with different CNT diameters d_c, distances L, and wall numbers. (a, b) The chiral index is (5, 5) with d_c = 0.68 nm. The inter-tube distances are L = 10 nm and 20 nm, respectively. (c, d) The chiral index is (8, 8) with d_c = 1.08 nm. The inter-tube distances are L = 20 nm and 35 nm, respectively. (e) The CNTs are double-walled with chiral index of (8, 8) and (3, 3). The inter-tube distance is L = 35 nm. The color bar represents the z-coordinate of each atom, where z_{min} represented by blue, corresponds to the minimum z-coordinate, and z_{max} represented by red, corresponds to the maximum coordinate.

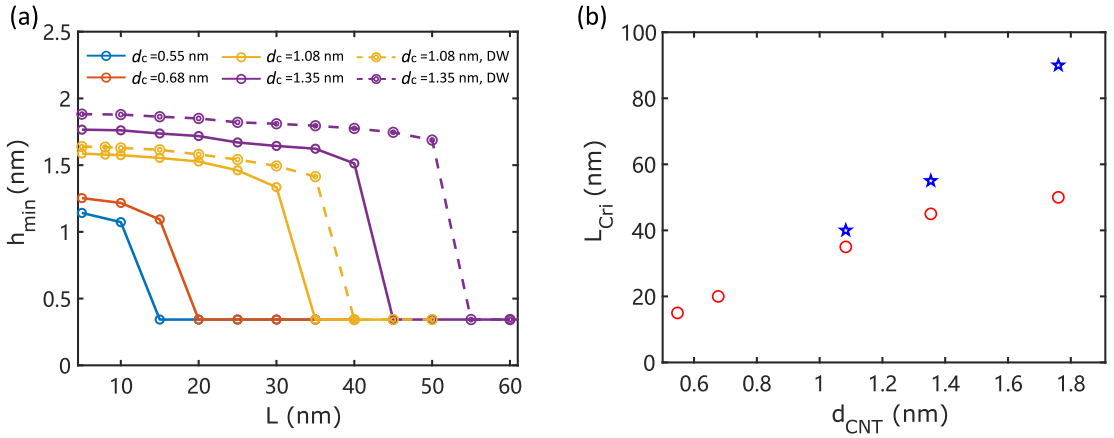

Fig. 5.3 (a) Effect of the CNT diameter d_c, distance L, and wall number on the minimum interlayer distance d_{min}. The cases of single-walled CNTs are plotted in lines with open circles of blue (d_c = 0.55 nm), red (d_c = 0.68 nm), yellow (d_c = 1.08 nm), and purple (d_c = 1.35 nm). The cases of double-walled CNTs are plotted in lines with circled circles of yellow (d_c = 1.08 nm) and purple (d_c = 1.35 nm). (b) Critical CNT distances (Lcri) as a function of the CNT diameter for single-walled (red circles) and double-walled (blue stars) CNTs.

that the increasing effect becomes less obvious. For CNTs with small d_c from 0.68 nm to 1.08 nm, the L_{cri} increases from 20 nm to 35 nm. Yet for larger d_c from 1.35 nm to 1.76 nm, the L_{cri} increases from 45 nm to 50 nm. Many previous studies have reported the collapse phenomena of single-walled CNTs which are spontaneous or induced by pressure. The collapse cross-section is energy stable for single-walled CNTs when the diameter is larger than a critical value [195–198]. The critical diameter for spontaneous collapse is 2-5 nm predicted by different models and methods [199–201]. The pressure-induced collapse is also reported [202]. The critical pressure of the collapse is $P \propto 1/d_c^3$ [203]. Thus, less pressure is required for CNTs with larger diameters. In the graphene-CNT system, the adhesion force of graphene layers between two CNTs is balanced by the supporting force of CNTs, which causes pressure on the CNTs. The increase of inter-tube distance L denotes a larger adhesion force and stronger pressure on CNTs. For CNTs with larger d_c, less pressure is required for the collapse of CNTs. Thus, the effect of large d_c becomes less obvious on increasing L_{cri}. The increased CNT wall number can further increase L_{cri} compared with the single-walled CNT of the same diameter. The double-walled CNTs can resist collapsing with larger critical pressure [195, 196]. The increment of L_{cri} between single-walled and double-walled CNTs is more obvious.

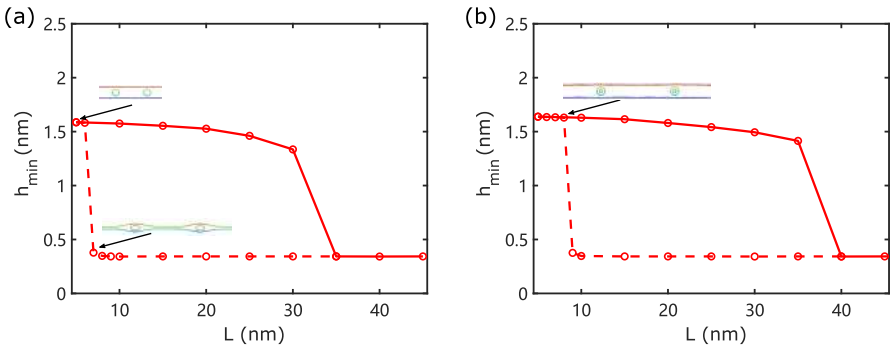

Fig. 5.4 The stable interlayer distance versus the inter-tube distance L from different initial configurations. The red solid lines with open circles are from suspended configurations and the red dashed lines with open circles are from adhesion configurations. (a) The CNTs are single-walled with chiral index (8, 8) and $d_c = 0.68$ nm. (b) The CNTs are double-walled with chiral index (8, 8) and $d_c = 0.68$ nm.

The energy-stable structure after relaxation can be sensitive to the initial configuration. The relaxation simulation with the initial adhesion configuration is also conducted (Figure 5.4). The adhesion structures were obtained by applying uniform pressing force on each graphene atom of the initial structures (the structure shown in Figure 5.1a). Then, the loading force was removed and the adhesion structure was relaxed with the same method in the 300 K NVT ensemble. The critical inter-tube distance L_{cri} decreases from 35 nm to 7 nm

(Figure 5.4a). This indicates that both adsorption and adhesion are stable configurations for graphene-CNT with $L \in (6, 35)$ nm. The double-walled CNTs also increase the critical inter-tube distance to 9 nm (Figure 5.4b). To separate the two distances, the critical value from the separation initial configurations is L_{cri1}, and the critical value from the adhesion initial configurations is L_{cri2}. For the cases with inter-tube distance L in $(L_{\text{cri1}}, L_{\text{cri2}})$, the multistable structure arise. The components of potential energy for different configurations are calculated to analyze the mechanism.

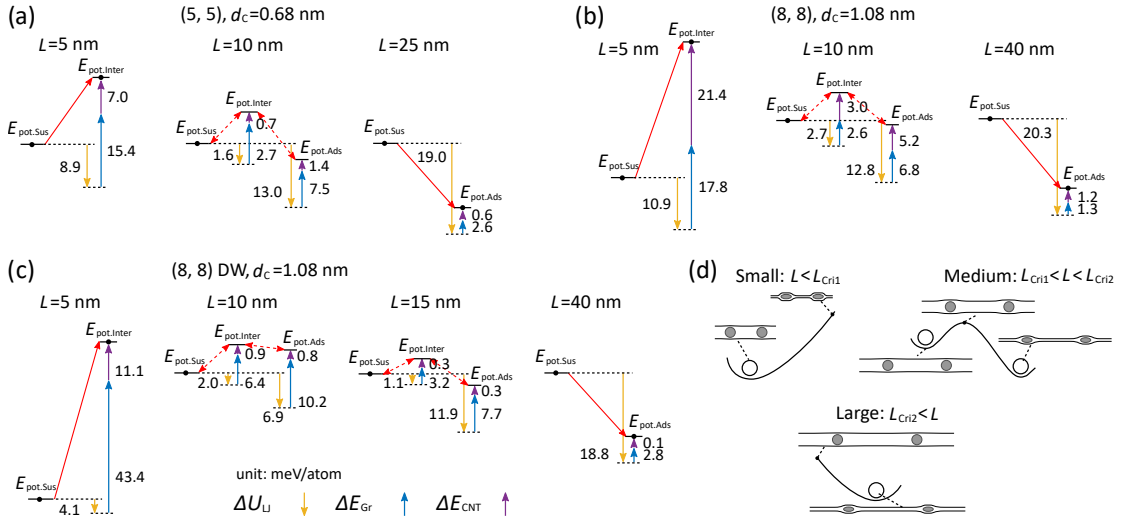

Fig. 5.5 Comparison of the energy between separation and adhesion for systems with different L and d_c. The yellow arrows represent the difference in vdW energy by LJ potential ΔU_{LJ}. The blue and purple arrows represent the difference in energy of the upper Gr ΔE_{Gr} and CNT ΔE_{CNT}, respectively. Red arrows indicate the difference in total potential energy. The unit of energy is eV/atom. (a) $d_c = 0.68$ nm, and $L = 5$, 10 and 25 nm. (b) $d_c = 1.08$ nm, and $L = 5$, 10 and 40 nm. (c) Double-walled CNT with outer tube diameter $d_c = 1.08$ nm, and $L = 5$, 10, 15 and 40 nm. (d) Schematic diagram of the energy difference between the energy of separation and adhesion configurations for different L.

The potential energy of the system determines the stable configuration. The total potential energy E_{pot} of the simulation system consists of several components:

$$E_{\text{pot}} = E_{\text{Gr}} + E_{\text{CNT}} + U_{\text{LJ}} \tag{5.2}$$

where E_{Gr} is the internal energy of the two Gr layers described by the AIREBO potential. The CNT internal energy E_{CNT} includes the AIREBO potential for the C-C bond and the LJ energy inside the CNT wall. The LJ interaction U_{LJ} includes the components of $U_{\text{GrU-L}}$ (between upper and lower Gr), $U_{\text{GrU-CNT}}$ (between upper Gr and CNT), and $U_{\text{GrL-CNT}}$ (between lower Gr and CNT). The variation in interlayer vdW energy $U_{\text{GrU-L}}$ constitutes the major part

since the contact area between CNTs and graphene layers is minor compared with the whole graphene, which makes $U_{\text{GrU-CNT}}$ and $U_{\text{GrL-CNT}}$ insignificant.

Each energy difference in Eq. 5.2 between the separation (Sep) and adhesion (Adh) configurations is calculated for the system with the same d_{CNT} and L. A Δ operator acting on the particular component represents the energy difference between the two configurations (eg. $\Delta E_{\text{pot}} = E_{\text{pot, Adh}} - E_{\text{pot, Sep}}$). Thus, the total potential energy E_{pot} and configuration of the system are primarily determined by E_{GrU}, E_{CNT} and $U_{\text{GrU-L}}$ (see Figure 5.5), which writes

$$\Delta E_{\text{pot}} \approx \Delta E_{\text{Gr}} + \Delta E_{\text{CNT}} + \Delta U_{\text{LJ}} \tag{5.3}$$

The adhesion configuration has a lower vdW potential energy than the separation configuration ($\Delta U_{\text{LJ}} < 0$) because the potential energy decreases with the interlayer distance h. The value of energy difference becomes more significant with an increase in the size of Gr, *i.e.* $\Delta U_{\text{LJ}} \propto L$ (see Figure 5.5). The deformation of Gr layers leads to the bending of angles between C-C bonds and an increase of internal energy ($\Delta E_{\text{Gr}} > 0$). In the adhesion configuration, the pressure from Gr layers causes the deformation of CNTs with an ellipse cross-section, which causes an extra increase of internal energy ($\Delta E_{\text{CNT}} > 0$).

The comparison of energy components for different L and d_c are shown in Fig. 5.5a. For a small inter-tube distance $L < L_{\text{cri1}}$, the increase of $\Delta E_{\text{GrU}} + \Delta E_{\text{CNT}}$ is more significant than the decrease of ΔU_{LJ}, making the separation a more stable energy configuration ($\Delta E_{\text{pot}} < 0$). As the inter-tube distance L increases, the lower vdW energy of the adhered Gr layers becomes more obvious ($\Delta U_{\text{LJ}} \propto L$), leading to smaller energy in the adhesion configuration ($\Delta E_{\text{pot}} < 0$). Thus, for a large distance $L_{\text{cri2}} < L$ (Fig. 5.5d), the adhesion configuration is more energy-stable regardless of the initial configuration. In the medium distance $L_{\text{cri1}} < L < L_{\text{cri2}}$, an intermediate configuration appears with a potential barrier that blocks the transition between the two configurations. During the transition from separation to adhesion, the approaching between Gr layers causes the decrease of U_{LJ} and the bending of Gr layers increases E_{Gr} and E_{CNT}. The total potential energy will increase initially ($E_{\text{pot,sep}} < E_{\text{pot,inter}}$), which means the transition will not happen spontaneously. The transition from adhesion to separation is also inert ($E_{\text{pot,adh}} < E_{\text{pot,inter}}$) due to the strong vdW adhesion between Gr layers.

The deformations of Gr layers and CNT cause the energy difference ΔE_{Gr} and ΔE_{CNT}. The increment of ΔE_{CNT} is larger for the CNT with a larger diameter (comparing Fig. 5.5 a and b). Larger ΔU_{Gr}, *i.e.* larger L, is required to overcome the energy barrier, which causes the increase of L_{Cri}. The double-walled CNT is harder to collapse the graphene than the single-walled CNT, but the deformation of the Gr layers becomes harder. The ΔE_{Gr} mainly contributes to the energy barrier (Fig. 5.5 c), while the ΔE_{CNT} is minor. The total value of

ΔE_{Gr} and ΔE_{CNT} of double-walled CNT is larger than the single-walled case which causes the increase of L_{Cri}.

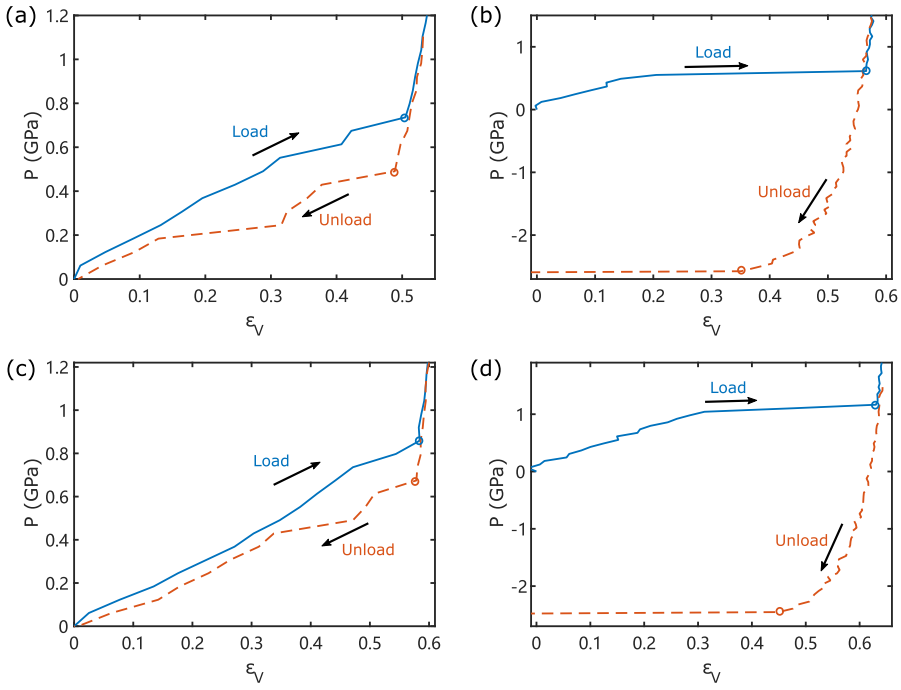

Fig. 5.6 Loading-unloading curvature of graphene-CNT stacked structures, indicated by the pressure P and the volume of the space between Gr layers. The loading and unloading curves are represented by solid blue lines and dashed red lines, respectively. The critical points of the graphene separation are shown by hollow circles. (a) d_c=0.68 nm, $L = 5$ nm. (b) d_c=0.68 nm, $L = 10$ nm. (c) d_c=1.08 nm, $L = 5$ nm. (d) d_c=1.08 nm, $L = 10$ nm.

The graphene-CNT hybrid structure is superelastic materials with ultra-compressibility and hysteresis loading curvature [41, 42, 40]. We further investigated the loading-unloading properties of the graphene-CNT structure under vertical pressure force. The structures that have separation configurations after relaxation are simulated. The loading press is imposed by adding a uniform force on each atom of graphene layers (Figure 5.1c). The deformation is indicated by volume strain ε_V. The initial volume of space between Gr layers is V_0, and the deformed volume in the loading process is V. The volume strain is defined as $\varepsilon_V = (V_0 - V)/V_0$. The hysteresis behavior is observed for the structure with d_c=0.68 nm and $L = 5$ nm (Figure 5.6a). The interlayer distance h_{min} decreases gradually as the pressure increases from 0. When the interlayer distance approaches 0.34 nm, the graphene layers adhere together. A further increase in pressure cannot induce much decrease in the interlayer distance because of the repulsive term in the vdW force (Eq. 5.1). The pressure is unloaded by decreasing the force on each graphene atom. The interlayer distance increases

as the graphene layers separate. However, the critical value of the imposed force during the unloading process where the graphene layer separates is lower than that of the loading process (hollow circles in Figure 5.6a). For the case with d_c=0.68 nm and $L = 10$ nm (Figure 5.6b), the loading force increases, making the graphene layers adhere at the critical point. The critical loading force is lower than the case with d_c=0.68 nm and $L = 5$ nm. Moreover, the unloading curvature is different from the previous case. The graphene separation does not appear even when the loading force is zero. The negative force value, *i.e.* a peeling force is required to separate the graphene layers. For the cases with larger CNT diameters $d_c =$ 1.08 nm (Figure 5.6c,d), the hysteresis also appears for the shorter inter-tube distance. The critical force value is larger than in Figure 5.6a. A similar peeling force is also required for the case with d_c=1.08 nm and $L = 10$ nm.

The experiments were conducted to observe the loading-unloading curves of the stacked structures. Pure rGO and rGO-CNT composite samples were prepared using vacuum filtration followed by high-temperature reduction. The press loading process was achieved via nano-indentation using AFM. Firstly, Figure 5.7(a) shows the surface morphology of rGO and rGO-CNT samples. Compared to the rGO sample, certain regions in the rGO-CNT sample exhibit increased height due to the separation caused by CNTs. This uneven distribution is attributed to CNT aggregation behavior. In regions with higher CNT density, the rGO layers are more separated. Figures 5.7(b) and (c) display the force curves at a single point for rGO and rGO-CNT samples, respectively. For the rGO sample, the loading and unloading curves overlap, while for the rGO-CNT sample, the curves do not coincide. This behavior is similar to the characteristics observed in loading-unloading curves from MD simulations. During the loading process, a greater force is required, whereas the force applied during unloading is smaller, leading to higher work done during loading compared to the energy released during unloading. The difference in external work done during the loading and unloading processes demonstrates the energy dissipation. On a macroscopic scale, similar energy dissipation phenomena have been observed in rGO-CNT foams used for strain sensors and energy-absorbing structures. By comparing the two types of samples, we infer that the introduction of CNTs induces this dissipation phenomenon. The area enclosed by the loading and unloading curves in the AFM measurements is defined as the dissipation energy. Figure 5.7(d) shows the dissipation energy distribution obtained from multi-point measurements across the sample surface. The histogram in Figure 5.7(e) presents the statistical distribution of dissipation energy at various observation points. The results indicate that higher dissipation energy is observed in the rGO-CNT sample, suggesting that the inclusion of CNTs is responsible for this dissipation phenomenon.

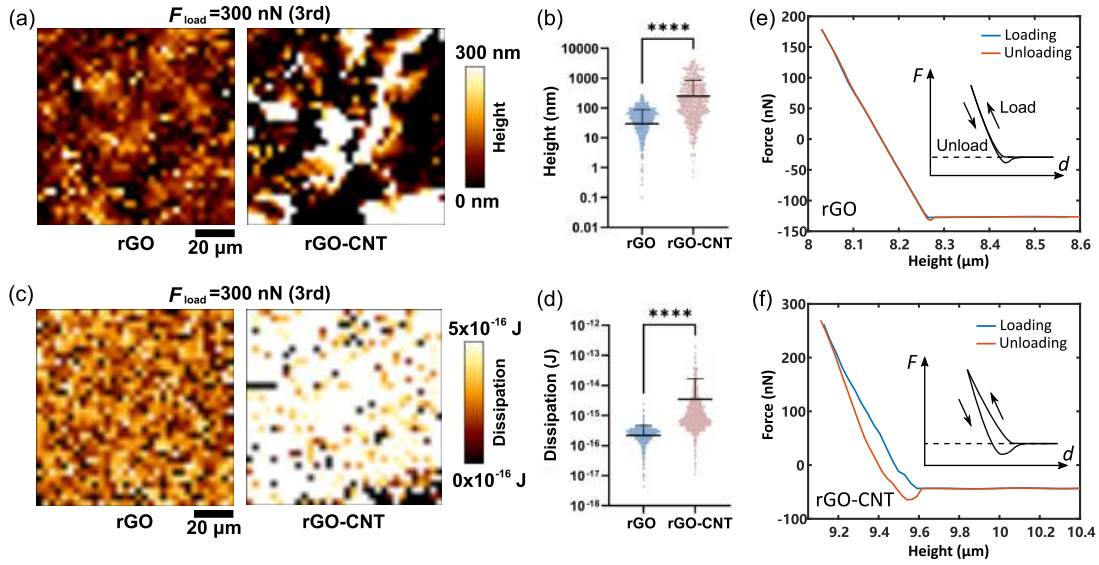

Fig. 5.7 (a) AFM surface images of rGO and rGO-CNT samples from the third time measurement with loading force of 300 nN. (b) Histogram of the height distribution for rGO and rGO-CNT samples. (c) Dissipation energy mapping for rGO and rGO-CNT samples. (d) Histogram of dissipation energy distribution for rGO and rGO-CNT. (e, f) Force curves from the loading-unloading process for rGO and rGO-CNT samples, with loading and unloading curves shown in blue and red, respectively.

5.2.5 Conclusion

In summary, we study the microstructure of the Gr-CNT stacking system using MD simulation. Two different energy-stable configurations, *i.e.*, separation and adhesion, exist. Larger CNT radius, shorter inter-tube distance, and multi-wall number can benefit the separation of Gr layers. The press loading-unloading curvature indicates the hysteresis behavior. Energy analysis unveils that multistable characteristics of the structure cause hysteresis. Our research contributes to a better understanding of the microstructure of Gr-CNT hybrid systems to facilitate function enhancement for wider application fields.

5.3 Nonlinear electrical property of graphene-nanodiamond stacking system

5.3.1 Background

Reservoir computing (RC) requires key characteristics such as nonlinearity, high dimensionality, and short-term memory to process time-series data effectively. Physical reservoir

systems, which leverage various physical phenomena, have been proposed to meet these requirements. To enhance their performance, it is essential to explore diverse physical systems and understand their operating principles.

In this context, nanostructures like carbon nanotubes (CNTs), hexagonal boron nitride (h-BN), and graphene have emerged as promising materials for RC applications. Previous studies have demonstrated physical reservoirs based on 2D and 3D CNT networks. In this part, the graphene and nanodiamond (Gr-ND) stacking structure is studied. The structures aim to leverage the high carrier mobility of graphene for improved conductivity, while utilizing the tunneling current through ND to introduce the necessary nonlinear current-voltage characteristics for RC.

5.3.2 Experiment design

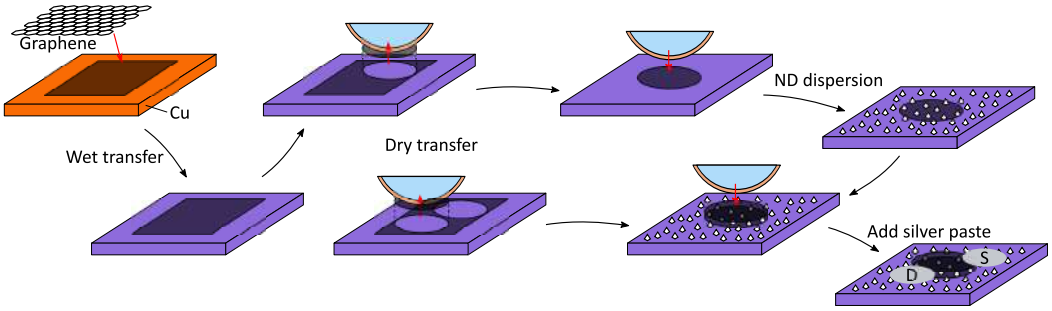

Fig. 5.8 The fabrication process of graphene-ND device.

The graphene-ND stacking structure was fabricated using the dry transfer method (Figure 5.8). Monolayer graphene was synthesized on a Cu foil substrate via chemical vapor deposition (CVD)[117, 118]. It was then transferred onto a silicon substrate with a 300 nm SiO_2 oxide layer using the wet transfer method with a poly(methyl methacrylate) (PMMA) support film [119, 120]. This step facilitated subsequent manipulations of the graphene on the silicon surface. The size of the wet-transferred graphene was approximately 5 mm. To scale down the device size, the dry transfer method [121–123] was used to pick up a graphene flake with a size of approximately 500 μm and place it on a new Si substrate. ND nanospacers were then deposited onto the graphene surface via spin coating. The ND was synthesized using the detonation method and dispersed in ethanol at a concentration of 0.2 wt.% (Nippon Kayaku). Spin coating was performed at 3000 rpm for 180 s, followed by heating the sample on a hot plate at 90 °C for 3 min to evaporate the ethanol. The second graphene layer was picked up from the same wet-transferred graphene on the Si substrate (Figure 5.8) and transferred onto the ND nanospacers using the dry transfer method. Finally,

electrodes were added by applying silver paste (Fujikura Kasei, DOTITE D-500) to the edges of the graphene.

5.3.3 Experimental results and analysis

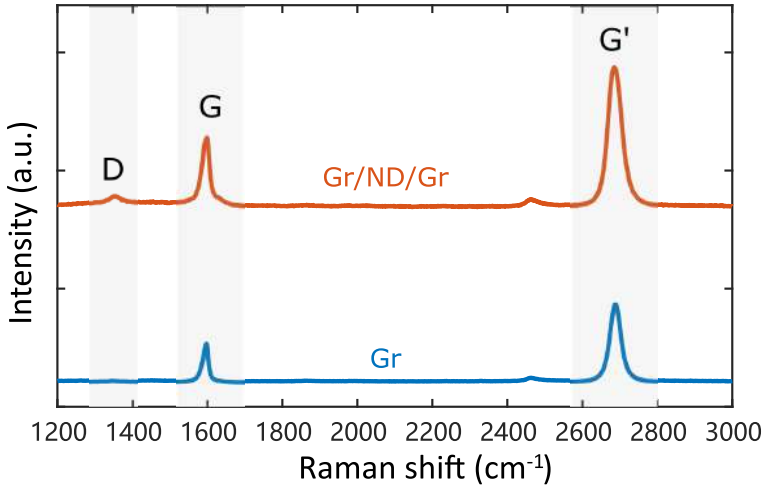

Fig. 5.9 Raman spectra of monolayer graphene (Gr) and graphene-ND stacking structure (Gr/ND/Gr).

Raman spectra confirm the decrease of interlayer interaction in the graphene-ND stacking structure with the $I(G')/I(G)$ approach 2.0 (Fig. 5.9).

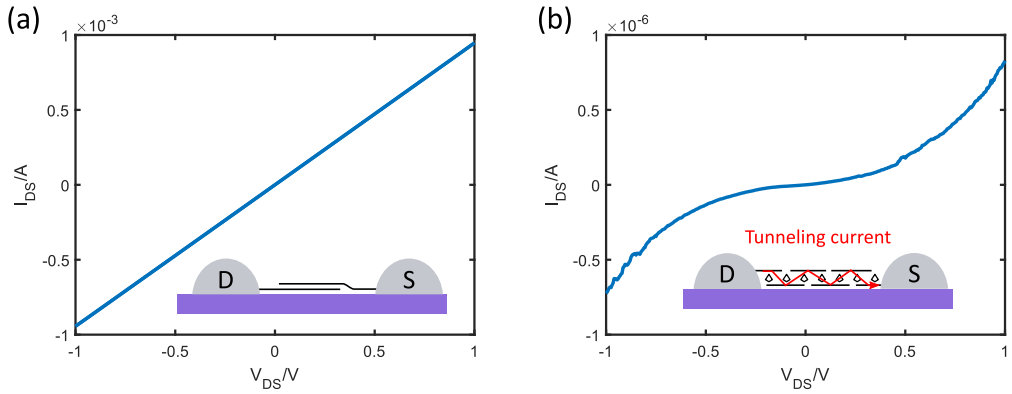

Fig. 5.10 Current-voltage (I-V) curve of double layer graphene (a) and graphene-ND (b).

The non-linear current-voltage (I-V) curve is observed which is different from the directly stacked double layer graphene (Fig. 5.10). The nonlinear current is attributed to the tunneling current between two graphene layers through nanodiamonds. Ideally, the current should

flow only in-plane within each graphene layer without any interlayer transport. However, due to the damage to graphene caused by the dry transfer process, a continuous pathway for graphene cannot be formed from one end of the electrode to the other, hindering efficient in-plane conduction. Consequently, the current undergoes interlayer transport through the nanodiamonds. The energy band diagram of the Gr/ND/Gr system is shown in Figure 5.11. The bottom of the conduction band of nanodiamonds is higher in energy than the Dirac point of graphene. This energy barrier hinders the electron flow from one graphene layer to the other, leading to the observed nonlinear current-voltage characteristics.

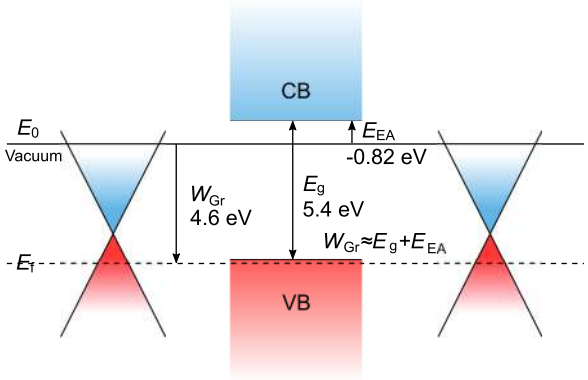

Fig. 5.11 Schematic model of the energy band structure of Gr/ND/Gr system.

5.3.4 Conclusions

The non-linear I-V curve is observed in the graphene-ND stacking system fabricated using the dry transfer method. The nonlinearity arises from the tunneling current through the ND spacers, demonstrating potential applications in physical neural network devices.

Chapter 6

Conclusion and future perspective

6.1 Conclusion

In this dissertation, the interlayer interaction modulation in multilayer graphene (Gr) using carbon nanotube (CNT) and nanodiamond (ND) spacers was systematically investigated through experiments and theoretical simulations.

In Chapter 3, the impact of CNT insertion on the interlayer interaction in multilayer Gr was studied. Experimentally, the Gr-CNT stacking structure was successfully fabricated. Raman spectroscopy and AFM measurements confirmed a reduction in interlayer interaction and an increase in interlayer spacing. MD simulations revealed two stable configurations for the Gr-CNT system: upper-layer suspension and interlayer adsorption. The CNT diameter, distance, and arrangement, were found to influence the energy-stable configurations. This research enhances the understanding of the Gr-CNT composite microstructure and paves the way for improved properties in multilayer Gr for broader applications.

In Chapter 4, the effect of ND insertion on interlayer interaction in multilayer Gr was examined. The Gr-ND stacking structures were constructed using a layer-by-layer fabrication method. Raman spectroscopy indicated a reduction in interlayer interaction, evidenced by the increase of G' to G peak intensity ratio and G peak splitting, while AFM measurements confirmed increased interlayer spacing. MD simulations identified two stable configurations for the Gr-ND system: upper-layer suspension and interlayer adhesion. The areal density and size of the NDs were found to dictate the system's morphology. A continuum model was developed to extend the simulation scale, accurately predicting the critical ND density and associated morphologies observed experimentally. These findings provide valuable insights into the microstructure and functionality of Gr-ND systems for enhanced material properties.

In Chapter 5, the modulation effect of properties for CNT and ND spacers were systematically investigated. For the Gr-CNT system, further MD simulations explored factors such as

CNT wall number, applied pressure, and multilayer configurations. The system exhibited multistable behavior between separated and adhered configurations, resulting in hysteresis in the loading-unloading curves. For the Gr-ND system, a nonlinear current-voltage (I-V) relationship was observed, attributed to tunneling current through the ND spacers, which highlights its potential for applications in physical neural networks.

Overall, the present work advances the understanding of interlayer interaction modulation in multilayer graphene systems, providing novel insights and laying the foundation for their functional enhancement and wider application in advanced materials and devices.

6.2 Future perspective

This study unveils the principles governing the microstructure of Gr-CNT systems from the perspective of interlayer interaction, providing a fundamental understanding for research on 3D Gr-CNT sponge structures. By employing multiscale approaches such as coarse-grained, direct simulations of 3D materials can be achieved. This is an area worthy of further exploration. Moreover, simulations of Gr-CNT structures can be extended to hBN-CNT or Gr-BNNT systems to investigate topics such as microstructural changes and the effects of CNT collapse on electronic structures.

For the Gr-ND system, the application of the non-linear I-V relationship in neural network devices will be further studied. The separation of the graphene layer has linear dispersion which affects the optical properties such as the absorbance. Optical and optoelectronic properties will be further studied in the stacking structure. The wrinkles induced by low-density ND can induce novel phenomena such as pseudo-magnetic fields which need further exploration.

References

[1] Sumio Iijima. Helical microtubules of graphitic carbon. *nature*, 354(6348):56–58, 1991.

[2] K. S. Novoselov, A. K. Geim, S. V. Morozov, D. Jiang, Y. Zhang, S. V. Dubonos, I. V. Grigorieva, and A. A. Firsov. Electric Field Effect in Atomically Thin Carbon Films. *Science*, 306(5696):666–669, October 2004.

[3] Andre K Geim and Konstantin S Novoselov. The rise of graphene. *Nature materials*, 6(3):183–191, 2007.

[4] K. S. Novoselov, A. K. Geim, S. V. Morozov, D. Jiang, M. I. Katsnelson, I. V. Grigorieva, S. V. Dubonos, and A. A. Firsov. Two-dimensional gas of massless Dirac fermions in graphene. *Nature*, 438(7065):197–200, November 2005.

[5] Taisuke Ohta, Aaron Bostwick, J. L. McChesney, Thomas Seyller, Karsten Horn, and Eli Rotenberg. Interlayer Interaction and Electronic Screening in Multilayer Graphene Investigated with Angle-Resolved Photoemission Spectroscopy. *Physical Review Letters*, 98(20):206802, May 2007.

[6] Isabella Gierz, Christian Riedl, Ulrich Starke, Christian R. Ast, and Klaus Kern. Atomic Hole Doping of Graphene. *Nano Letters*, 8(12):4603–4607, December 2008.

[7] M. Sprinkle, D. Siegel, Y. Hu, J. Hicks, A. Tejeda, A. Taleb-Ibrahimi, P. Le Fèvre, F. Bertran, S. Vizzini, H. Enriquez, S. Chiang, P. Soukiassian, C. Berger, W. A. De Heer, A. Lanzara, and E. H. Conrad. First Direct Observation of a Nearly Ideal Graphene Band Structure. *Physical Review Letters*, 103(22):226803, November 2009.

[8] S. Y. Zhou, G.-H. Gweon, J. Graf, A. V. Fedorov, C. D. Spataru, R. D. Diehl, Y. Kopelevich, D.-H. Lee, Steven G. Louie, and A. Lanzara. First direct observation of Dirac fermions in graphite. *Nature Physics*, 2(9):595–599, September 2006.

[9] A. H. Castro Neto, F. Guinea, N. M. R. Peres, K. S. Novoselov, and A. K. Geim. The electronic properties of graphene. *Reviews of Modern Physics*, 81(1):109–162, January 2009.

[10] S. V. Morozov, K. S. Novoselov, M. I. Katsnelson, F. Schedin, D. C. Elias, J. A. Jaszczak, and A. K. Geim. Giant Intrinsic Carrier Mobilities in Graphene and Its Bilayer. *Physical Review Letters*, 100(1):016602, January 2008.

[11] Alexander A. Balandin, Suchismita Ghosh, Wenzhong Bao, Irene Calizo, Desalegne Teweldebrhan, Feng Miao, and Chun Ning Lau. Superior Thermal Conductivity of Single-Layer Graphene. *Nano Letters*, 8(3):902–907, March 2008.

[12] Suchismita Ghosh, Wenzhong Bao, Denis L. Nika, Samia Subrina, Evghenii P. Pokatilov, Chun Ning Lau, and Alexander A. Balandin. Dimensional crossover of thermal transport in few-layer graphene. *Nature Materials*, 9(7):555–558, July 2010.

[13] Changgu Lee, Xiaoding Wei, Jeffrey W. Kysar, and James Hone. Measurement of the elastic properties and intrinsic strength of monolayer graphene. *Science*, 321(5887):385–388, 2008.

[14] Deji Akinwande, Christopher J. Brennan, J. Scott Bunch, Philip Egberts, Jonathan R. Felts, Huajian Gao, Rui Huang, Joon-Seok Kim, Teng Li, Yao Li, Kenneth M. Liechti, Nanshu Lu, Harold S. Park, Evan J. Reed, Peng Wang, Boris I. Yakobson, Teng Zhang, Yong-Wei Zhang, Yao Zhou, and Yong Zhu. A review on mechanics and mechanical properties of 2D materials—Graphene and beyond. *Extreme Mechanics Letters*, 13:42–77, May 2017.

[15] Kin Fai Mak, Matthew Y. Sfeir, Yang Wu, Chun Hung Lui, James A. Misewich, and Tony F. Heinz. Measurement of the Optical Conductivity of Graphene. *Physical Review Letters*, 101(19):196405, November 2008.

[16] Shou-En Zhu, Shengjun Yuan, and G. C. A. M. Janssen. Optical transmittance of multilayer graphene. *EPL (Europhysics Letters)*, 108(1):17007, October 2014.

[17] Kin Fai Mak, Long Ju, Feng Wang, and Tony F. Heinz. Optical spectroscopy of graphene: From the far infrared to the ultraviolet. *Solid State Communications*, 152(15):1341–1349, August 2012.

[18] Daniel R. Dreyer, Sungjin Park, Christopher W. Bielawski, and Rodney S. Ruoff. The chemistry of graphene oxide. *Chem. Soc. Rev.*, 39(1):228–240, 2010.

[19] Z. H. Ni, H. M. Wang, J. Kasim, H. M. Fan, T. Yu, Y. H. Wu, Y. P. Feng, and Z. X. Shen. Graphene Thickness Determination Using Reflection and Contrast Spectroscopy. *Nano Letters*, 7(9):2758–2763, September 2007.

[20] Sukang Bae, Hyeongkeun Kim, Youngbin Lee, Xiangfan Xu, Jae-Sung Park, Yi Zheng, Jayakumar Balakrishnan, Tian Lei, Hye Ri Kim, Young Il Song, Young-Jin Kim, Kwang S. Kim, Barbaros Özyilmaz, Jong-Hyun Ahn, Byung Hee Hong, and Sumio Iijima. Roll-to-roll production of 30-inch graphene films for transparent electrodes. *Nature Nanotechnology*, 5(8):574–578, August 2010.

[21] Ferdinando Tristán-López, Aaron Morelos-Gómez, Sofía Magdalena Vega-Díaz, María Luisa García-Betancourt, Néstor Perea-López, Ana L. Elías, Hiroyuki Muramatsu, Rodolfo Cruz-Silva, Shuji Tsuruoka, Yoong Ahm Kim, Takuya Hayahsi, Katsumi Kaneko, Morinobu Endo, and Mauricio Terrones. Large Area Films of Alternating Graphene–Carbon Nanotube Layers Processed in Water. *ACS Nano*, 7(12):10788–10798, December 2013.

[22] Yi Zhang, Luyao Zhang, and Chongwu Zhou. Review of Chemical Vapor Deposition of Graphene and Related Applications. *Accounts of Chemical Research*, 46(10):2329–2339, October 2013.

[23] Songfeng Pei and Hui-Ming Cheng. The reduction of graphene oxide. *Carbon*, 50(9):3210–3228, August 2012.

[24] Dmitriy A. Dikin, Sasha Stankovich, Eric J. Zimney, Richard D. Piner, Geoffrey H. B. Dommett, Guennadi Evmenenko, SonBinh T. Nguyen, and Rodney S. Ruoff. Preparation and characterization of graphene oxide paper. *Nature*, 448(7152):457–460, July 2007.

[25] S. Y. Zhou, G.-H. Gweon, A. V. Fedorov, P. N. First, W. A. De Heer, D.-H. Lee, F. Guinea, A. H. Castro Neto, and A. Lanzara. Substrate-induced bandgap opening in epitaxial graphene. *Nature Materials*, 6(10):770–775, October 2007.

[26] Wei Gao, Neelam Singh, Li Song, Zheng Liu, Arava Leela Mohana Reddy, Lijie Ci, Robert Vajtai, Qing Zhang, Bingqing Wei, and Pulickel M. Ajayan. Direct laser writing of micro-supercapacitors on hydrated graphite oxide films. *Nature Nanotechnology*, 6(8):496–500, August 2011.

[27] Jian Lin, Zhiwei Peng, Yuanyue Liu, Francisco Ruiz-Zepeda, Ruquan Ye, Errol L. G. Samuel, Miguel Jose Yacaman, Boris I. Yakobson, and James M. Tour. Laser-induced porous graphene films from commercial polymers. *Nature Communications*, 5(1):5714, December 2014.

[28] Michael G. Stanford, Kaichun Yang, Yieu Chyan, Carter Kittrell, and James M. Tour. Laser-Induced Graphene for Flexible and Embeddable Gas Sensors. *ACS Nano*, 13(3):3474–3482, March 2019.

[29] Ruquan Ye, Dustin K. James, and James M. Tour. Laser-Induced Graphene: From Discovery to Translation. *Advanced Materials*, 31(1):1803621, January 2019.

[30] Ming Liu, Xiaobo Yin, Erick Ulin-Avila, Baisong Geng, Thomas Zentgraf, Long Ju, Feng Wang, and Xiang Zhang. A graphene-based broadband optical modulator. *Nature*, 474(7349):64–67, June 2011.

[31] F. Bonaccorso, Z. Sun, T. Hasan, and A. C. Ferrari. Graphene photonics and optoelectronics. *Nature Photonics*, 4(9):611–622, September 2010.

[32] Jian Zhao, Peixuan Ji, Yaqi Li, Rui Li, Kaimin Zhang, Hao Tian, Kaicheng Yu, Boyue Bian, Luzhen Hao, Xue Xiao, Will Griffin, Noel Dudeck, Ramiro Moro, Lei Ma, and Walt A. De Heer. Ultrahigh-mobility semiconducting epitaxial graphene on silicon carbide. *Nature*, 625(7993):60–65, January 2024.

[33] Wenjing Yuan and Gaoquan Shi. Graphene-based gas sensors. *Journal of Materials Chemistry A*, 1(35):10078, 2013.

[34] Shixin Wu, Qiyuan He, Chaoliang Tan, Yadong Wang, and Hua Zhang. Graphene-Based Electrochemical Sensors. *Small*, 9(8):1160–1172, April 2013.

[35] Qiyuan He, Shixin Wu, Zongyou Yin, and Hua Zhang. Graphene-based electronic sensors. *Chemical Science*, 3(6):1764, 2012.

[36] Beibei Zhan, Chen Li, Jun Yang, Gareth Jenkins, Wei Huang, and Xiaochen Dong. Graphene Field-Effect Transistor and Its Application for Electronic Sensing. *Small*, 10(20):4042–4065, October 2014.

[37] Wenchao Wan, Ruiyang Zhang, Wei Li, Hao Liu, Yuanhua Lin, Lina Li, and Ying Zhou. Graphene–carbon nanotube aerogel as an ultra-light, compressible and recyclable highly efficient absorbent for oil and dyes. *Environmental Science: Nano*, 3(1):107–113, 2016.

[38] Maher F. El-Kady, Yuanlong Shao, and Richard B. Kaner. Graphene for batteries, supercapacitors and beyond. *Nature Reviews Materials*, 1(7):16033, May 2016.

[39] Peng Lv, Xiao-Wen Tan, Ke-Han Yu, Rui-Lin Zheng, Jia-Jin Zheng, and Wei Wei. Super-elastic graphene/carbon nanotube aerogel: A novel thermal interface material with highly thermal transport properties. *Carbon*, 99:222–228, April 2016.

[40] Jannatul Dil Afroze, Liyong Tong, Md Jaynul Abden, Ziwen Yuan, and Yuan Chen. Hierarchical honeycomb graphene aerogels reinforced by carbon nanotubes with multifunctional mechanical and electrical properties. *Carbon*, 175:312–321, April 2021.

[41] Kyu Hun Kim, Youngseok Oh, and M. F. Islam. Graphene coating makes carbon nanotube aerogels superelastic and resistant to fatigue. *Nature Nanotechnology*, 7(9):562–566, September 2012.

[42] Jinhui Li, Weixin Li, Wangping Huang, Guoping Zhang, Rong Sun, and Ching-Ping Wong. Fabrication of highly reinforced and compressible graphene/carbon nanotube hybrid foams via a facile self-assembly process for application as strain sensors and beyond. *Journal of Materials Chemistry C*, 5(10):2723–2730, 2017.

[43] Haizhou Liu, Ying Xu, Xiaodong Zhao, Dong Han, Fei Zhao, and Qiaowen Yang. Lightweight leaf-structured carbon nanotubes/graphene foam and the composites with polydimethylsiloxane for electromagnetic interference shielding. *Carbon*, 191:183–194, May 2022.

[44] Zizhao Xu, Yuna Himura, Chikako Ishiguro, Taiki Inoue, Yuta Nishina, and Yoshihiro Kobayashi. Improved performance of strain sensors constructed from highly crystalline graphene with nanospacer. *Japanese Journal of Applied Physics*, 63(1):015001, January 2024.

[45] Soumyabrata Roy, Xiang Zhang, Anand B. Puthirath, Ashokkumar Meiyazhagan, Sohini Bhattacharyya, Muhammad M. Rahman, Ganguli Babu, Sandhya Susarla, Sreehari K. Saju, Mai Kim Tran, Lucas M. Sassi, M. A. S. R. Saadi, Jiawei Lai, Onur Sahin, Seyed Mohammad Sajadi, Bhuvaneswari Dharmarajan, Devashish Salpekar, Nithya Chakingal, Abhijit Baburaj, Xinting Shuai, Aparna Adumbumkulath, Kristen A. Miller, Jessica M. Gayle, Alec Ajnsztajn, Thibeorchews Prasankumar, Vijay Vedhan Jayanthi Harikrishnan, Ved Ojha, Harikishan Kannan, Ali Zein Khater, Zhenwei Zhu, Sathvik Ajay Iyengar, Pedro Alves Da Silva Autreto, Eliezer Fernando Oliveira, Guanhui Gao, A. Glen Birdwell, Mahesh R. Neupane, Tony G. Ivanov, Jaime Taha-Tijerina, Ram Manohar Yadav, Sivaram Arepalli, Robert Vajtai, and Pulickel M.

Ajayan. Structure, Properties and Applications of Two-Dimensional Hexagonal Boron Nitride. *Advanced Materials*, 33(44):2101589, November 2021.

[46] G. Cassabois, P. Valvin, and B. Gil. Hexagonal boron nitride is an indirect bandgap semiconductor. *Nature Photonics*, 10(4):262–266, April 2016.

[47] Joshua D. Caldwell, Igor Aharonovich, Guillaume Cassabois, James H. Edgar, Bernard Gil, and D. N. Basov. Photonics with hexagonal boron nitride. *Nature Reviews Materials*, 4(8):552–567, July 2019.

[48] Kenji Watanabe, Takashi Taniguchi, and Hisao Kanda. Direct-bandgap properties and evidence for ultraviolet lasing of hexagonal boron nitride single crystal. *Nature Materials*, 3(6):404–409, June 2004.

[49] Yoichi Kubota, Kenji Watanabe, Osamu Tsuda, and Takashi Taniguchi. Deep ultraviolet light-emitting hexagonal boron nitride synthesized at atmospheric pressure. *Science*, 317(5840):932–934, 2007.

[50] Li Song, Lijie Ci, Hao Lu, Pavel B. Sorokin, Chuanhong Jin, Jie Ni, Alexander G. Kvashnin, Dmitry G. Kvashnin, Jun Lou, Boris I. Yakobson, and Pulickel M. Ajayan. Large Scale Growth and Characterization of Atomic Hexagonal Boron Nitride Layers. *Nano Letters*, 10(8):3209–3215, August 2010.

[51] Soo Min Kim, Allen Hsu, Min Ho Park, Sang Hoon Chae, Seok Joon Yun, Joo Song Lee, Dae-Hyun Cho, Wenjing Fang, Changgu Lee, Tomás Palacios, Mildred Dresselhaus, Ki Kang Kim, Young Hee Lee, and Jing Kong. Synthesis of large-area multilayer hexagonal boron nitride for high material performance. *Nature Communications*, 6(1):8662, October 2015.

[52] Dillon Wong, Jairo Velasco, Long Ju, Juwon Lee, Salman Kahn, Hsin-Zon Tsai, Chad Germany, Takashi Taniguchi, Kenji Watanabe, Alex Zettl, Feng Wang, and Michael F. Crommie. Characterization and manipulation of individual defects in insulating hexagonal boron nitride using scanning tunnelling microscopy. *Nature Nanotechnology*, 10(11):949–953, November 2015.

[53] Gaoqiang Deng, Yuantao Zhang, Ye Yu, Xu Han, Yang Wang, Zhifeng Shi, Xin Dong, Baolin Zhang, Guotong Du, and Yang Liu. High-Performance Ultraviolet Light-Emitting Diodes Using n-ZnO/p-hBN/p-GaN Contact Heterojunctions. *ACS Applied Materials & Interfaces*, 12(5):6788–6792, February 2020.

[54] Gabriele Grosso, Hyowon Moon, Benjamin Lienhard, Sajid Ali, Dmitri K. Efetov, Marco M. Furchi, Pablo Jarillo-Herrero, Michael J. Ford, Igor Aharonovich, and Dirk Englund. Tunable and high-purity room temperature single-photon emission from atomic defects in hexagonal boron nitride. *Nature Communications*, 8(1):705, September 2017.

[55] C. R. Dean, A. F. Young, I. Meric, C. Lee, L. Wang, S. Sorgenfrei, K. Watanabe, T. Taniguchi, P. Kim, K. L. Shepard, and J. Hone. Boron nitride substrates for high-quality graphene electronics. *Nature Nanotechnology*, 5(10):722–726, October 2010.

[56] L. Wang, I. Meric, P. Y. Huang, Q. Gao, Y. Gao, H. Tran, T. Taniguchi, K. Watanabe, L. M. Campos, D. A. Muller, J. Guo, P. Kim, J. Hone, K. L. Shepard, and C. R. Dean. One-Dimensional Electrical Contact to a Two-Dimensional Material. *Science*, 342(6158):614–617, November 2013.

[57] Jhao-Wun Huang, Cheng Pan, Son Tran, Bin Cheng, Kenji Watanabe, Takashi Taniguchi, Chun Ning Lau, and Marc Bockrath. Superior Current Carrying Capacity of Boron Nitride Encapsulated Carbon Nanotubes with Zero-Dimensional Contacts. *Nano Letters*, 15(10):6836–6840, October 2015.

[58] Xu Cui, Gwan-Hyoung Lee, Young Duck Kim, Ghidewon Arefe, Pinshane Y. Huang, Chul-Ho Lee, Daniel A. Chenet, Xian Zhang, Lei Wang, Fan Ye, Filippo Pizzocchero, Bjarke S. Jessen, Kenji Watanabe, Takashi Taniguchi, David A. Muller, Tony Low, Philip Kim, and James Hone. Multi-terminal transport measurements of MoS2 using a van der Waals heterostructure device platform. *Nature Nanotechnology*, 10(6):534–540, June 2015.

[59] L. Britnell, R. V. Gorbachev, R. Jalil, B. D. Belle, F. Schedin, A. Mishchenko, T. Georgiou, M. I. Katsnelson, L. Eaves, S. V. Morozov, N. M. R. Peres, J. Leist, A. K. Geim, K. S. Novoselov, and L. A. Ponomarenko. Field-Effect Tunneling Transistor Based on Vertical Graphene Heterostructures. *Science*, 335(6071):947–950, February 2012.

[60] Xiaofeng Fan, C.-H. Chang, W. T. Zheng, Jer-Lai Kuo, and David J. Singh. The Electronic Properties of Single-Layer and Multilayer MoS_2 under High Pressure. *The Journal of Physical Chemistry C*, 119(19):10189–10196, May 2015.

[61] Eugene S. Kadantsev and Pawel Hawrylak. Electronic structure of a single MoS2 monolayer. *Solid State Communications*, 152(10):909–913, May 2012.

[62] Branimir Radisavljevic and Andras Kis. Mobility engineering and a metal–insulator transition in monolayer MoS2. *Nature Materials*, 12(9):815–820, September 2013.

[63] Zhihao Yu, Zhun-Yong Ong, Songlin Li, Jian-Bin Xu, Gang Zhang, Yong-Wei Zhang, Yi Shi, and Xinran Wang. Analyzing the Carrier Mobility in Transition-Metal Dichalcogenide MoS_2 Field-Effect Transistors. *Advanced Functional Materials*, 27(19):1604093, May 2017.

[64] B. Radisavljevic, A. Radenovic, J. Brivio, V. Giacometti, and A. Kis. Single-layer MoS2 transistors. *Nature Nanotechnology*, 6(3):147–150, March 2011.

[65] Dominik Lembke, Simone Bertolazzi, and Andras Kis. Single-Layer MoS_2 Electronics. *Accounts of Chemical Research*, 48(1):100–110, January 2015.

[66] Mengyue Wang, Keisuke Nakamura, Michiharu Arifuku, Noriko Kiyoyanagi, Taiki Inoue, and Yoshihiro Kobayashi. Growth of Single-Walled Carbon Nanotubes from Solid Carbon Nanoparticle Seeds via Cap Formation Engineering with a Two-Step Growth Process and Water Vapor Supply. *ACS Omega*, 7(4):3639–3648, February 2022.

[67] A. Krüger, F. Kataoka, M. Ozawa, T. Fujino, Y. Suzuki, A.E. Aleksenskii, A. Ya. Vul', and E. Ōsawa. Unusually tight aggregation in detonation nanodiamond: Identification and disintegration. *Carbon*, 43(8):1722–1730, July 2005.

[68] M. Ozawa, M. Inaguma, M. Takahashi, F. Kataoka, A. Krüger, and E. Ōsawa. Preparation and Behavior of Brownish, Clear Nanodiamond Colloids. *Advanced Materials*, 19(9):1201–1206, May 2007.

[69] K. Turcheniuk, C. Trecazzi, C. Deeleepojananan, and V. N. Mochalin. Salt-Assisted Ultrasonic Deaggregation of Nanodiamond. *ACS Applied Materials & Interfaces*, 8(38):25461–25468, September 2016.

[70] Nguyen N. T. Nam and Mikito Koshino. Lattice relaxation and energy band modulation in twisted bilayer graphene. *Physical Review B*, 96(7):075311, August 2017.

[71] Da Zhan, Li Sun, Zhen Hua Ni, Lei Liu, Xiao Feng Fan, Yingying Wang, Ting Yu, Yeng Ming Lam, Wei Huang, and Ze Xiang Shen. FeCl $_3$ -Based Few-Layer Graphene Intercalation Compounds: Single Linear Dispersion Electronic Band Structure and Strong Charge Transfer Doping. *Advanced Functional Materials*, 20(20):3504–3509, October 2010.

[72] Namdong Kim, Kwang S. Kim, Naeyoung Jung, Louis Brus, and Philip Kim. Synthesis and Electrical Characterization of Magnetic Bilayer Graphene Intercalate. *Nano Letters*, 11(2):860–865, February 2011.

[73] Wei Liu, Jiahao Kang, and Kaustav Banerjee. Characterization of FeCl $_3$ Intercalation Doped CVD Few-Layer Graphene. *IEEE Electron Device Letters*, 37(9):1246–1249, September 2016.

[74] Keith Share, Adam P. Cohn, Rachel E. Carter, and Cary L. Pint. Mechanism of potassium ion intercalation staging in few layered graphene from in situ Raman spectroscopy. *Nanoscale*, 8(36):16435–16439, 2016.

[75] Hiroki Kinoshita, Il Jeon, Mina Maruyama, Kenji Kawahara, Yuri Terao, Dong Ding, Rika Matsumoto, Yutaka Matsuo, Susumu Okada, and Hiroki Ago. Highly Conductive and Transparent Large-Area Bilayer Graphene Realized by MoCl $_5$ Intercalation. *Advanced Materials*, 29(41):1702141, November 2017.

[76] Daniel T. Larson, Stephen Carr, Georgios A. Tritsaris, and Efthimios Kaxiras. Effects of lithium intercalation in twisted bilayer graphene. *Physical Review B*, 101(7):075407, February 2020.

[77] Yuji Araki, Pablo Solís-Fernández, Yung-Chang Lin, Amane Motoyama, Kenji Kawahara, Mina Maruyama, Yanlin Gao, Rika Matsumoto, Kazu Suenaga, Susumu Okada, and Hiroki Ago. Twist Angle-Dependent Molecular Intercalation and Sheet Resistance in Bilayer Graphene. *ACS Nano*, 16(9):14075–14085, September 2022.

[78] Jiuke Mu, Chengyi Hou, Hongzhi Wang, Yaogang Li, and Qinghong Zhang. Graphene-carbon nanotube papers for energy conversion and storage under sunlight and heat. *Carbon*, 95:150–156, December 2015.

[79] Yaling Wang, Yan Zhang, Guolong Wang, Xiaowei Shi, Yide Qiao, Jiamei Liu, Heguang Liu, Anandha Ganesh, and Lei Li. Direct Graphene-Carbon Nanotube Composite Ink Writing All-Solid-State Flexible Microsupercapacitors with High Areal Energy Density. *Advanced Functional Materials*, 30(16):1907284, April 2020.

[80] Shuting Peng, Lichang Wang, Ziqiang Zhu, and Kai Han. Electrochemical performance of reduced graphene oxide/carbon nanotube hybrid papers as binder-free anodes for potassium-ion batteries. *Journal of Physics and Chemistry of Solids*, 138:109296, March 2020.

[81] Kedong Shang, Tingting Yang, Chuanfei Guo, Xiaobo Pu, Yong Zhang, Xulei Lu, Changliu He, Jian Zhou, Lei Wu, Bingjun Yu, Liang Jiang, and Linmao Qian. Interfacial Enhanced 1D–2D Composite toward Mechanically Robust Strain Sensors. *Advanced Materials Interfaces*, 9(30):2201201, October 2022.

[82] Dengsong Zhang, Tingting Yan, Liyi Shi, Zheng Peng, Xiaoru Wen, and Jianping Zhang. Enhanced capacitive deionization performance of graphene/carbon nanotube composites. *Journal of Materials Chemistry*, 22(29):14696, 2012.

[83] Zizhao Xu, Shingo Nakamura, Taiki Inoue, Yuta Nishina, and Yoshihiro Kobayashi. Bulk-scale synthesis of randomly stacked graphene with high crystallinity. *Carbon*, 185:368–375, November 2021.

[84] Vaidehi Menon and Alper Buldum. Mechanical properties of graphene-CNT van der Waals heterostructures: a molecular dynamics study. *Nanotechnology*, 31(45):455707, November 2020.

[85] Tianyan Xu and Jinwu Jiang. On the configuration of the graphene/carbon nanotube/graphene van der Waals heterostructure. *Physical Chemistry Chemical Physics*, 25(6):5066–5072, 2023.

[86] Steven J. Stuart, Alan B. Tutein, and Judith A. Harrison. A reactive potential for hydrocarbons with intermolecular interactions. *The Journal of Chemical Physics*, 112(14):6472–6486, April 2000.

[87] Aidan P. Thompson, H. Metin Aktulga, Richard Berger, Dan S. Bolintineanu, W. Michael Brown, Paul S. Crozier, Pieter J. In 'T Veld, Axel Kohlmeyer, Stan G. Moore, Trung Dac Nguyen, Ray Shan, Mark J. Stevens, Julien Tranchida, Christian Trott, and Steven J. Plimpton. LAMMPS - a flexible simulation tool for particle-based materials modeling at the atomic, meso, and continuum scales. *Computer Physics Communications*, 271:108171, February 2022.

[88] Geraldine L. C. Paulus, Qing Hua Wang, Zachary W. Ulissi, Thomas P. McNicholas, Aravind Vijayaraghavan, Chih-Jen Shih, Zhong Jin, and Michael S. Strano. Charge Transfer at Junctions of a Single Layer of Graphene and a Metallic Single Walled Carbon Nanotube. *Small*, 9(11):1954–1963, June 2013.

[89] Yongping Liao, Kimmo Mustonen, Semir Tulić, Viera Skákalová, Sabbir A. Khan, Patrik Laiho, Qiang Zhang, Changfeng Li, Mohammad R. A. Monazam, Jani Kotakoski, Harri Lipsanen, and Esko I. Kauppinen. Enhanced Tunneling in a Hybrid of Single-Walled Carbon Nanotubes and Graphene. *ACS Nano*, 13(10):11522–11529, October 2019.

[90] Yuanda Liu, Fengqiu Wang, Xiaomu Wang, Xizhang Wang, Emmanuel Flahaut, Xiaolong Liu, Yao Li, Xinran Wang, Yongbing Xu, Yi Shi, and Rong Zhang. Planar carbon nanotube–graphene hybrid films for high-performance broadband photodetectors. *Nature Communications*, 6(1):8589, October 2015.

[91] Iskandar N. Kholmanov, Carl W. Magnuson, Richard Piner, Jin-Young Kim, Ali E. Aliev, Cheng Tan, Tae Young Kim, Anvar A. Zakhidov, Giorgio Sberveglieri, Ray H. Baughman, and Rodney S. Ruoff. Optical, Electrical, and Electromechanical Properties of Hybrid Graphene/Carbon Nanotube Films. *Advanced Materials*, 27(19):3053–3059, May 2015.

[92] Dingshan Yu, Kunli Goh, Hong Wang, Li Wei, Wenchao Jiang, Qiang Zhang, Liming Dai, and Yuan Chen. Scalable synthesis of hierarchically structured carbon nanotube–graphene fibres for capacitive energy storage. *Nature Nanotechnology*, 9(7):555–562, July 2014.

[93] Dingshan Yu and Liming Dai. Self-Assembled Graphene/Carbon Nanotube Hybrid Films for Supercapacitors. *The Journal of Physical Chemistry Letters*, 1(2):467–470, January 2010.

[94] Yangyang Xu, Peilin Deng, Guangda Chen, Jinxi Chen, Ya Yan, Kai Qi, Hongfang Liu, and Bao Yu Xia. 2D Nitrogen-Doped Carbon Nanotubes/Graphene Hybrid as Bifunctional Oxygen Electrocatalyst for Long-Life Rechargeable Zn–Air Batteries. *Advanced Functional Materials*, 30(6):1906081, February 2020.

[95] Yanguang Li, Wu Zhou, Hailiang Wang, Liming Xie, Yongye Liang, Fei Wei, Juan-Carlos Idrobo, Stephen J. Pennycook, and Hongjie Dai. An oxygen reduction electrocatalyst based on carbon nanotube–graphene complexes. *Nature Nanotechnology*, 7(6):394–400, June 2012.

[96] Chenyi Shi, Jiaoran Meng, and Chunhui Deng. Facile synthesis of magnetic graphene and carbon nanotube composites as a novel matrix and adsorbent for enrichment and detection of small molecules by MALDI-TOF MS. *Journal of Materials Chemistry*, 22(38):20778, 2012.

[97] Zefang Yin, Chaojie Cui, Hang Chen, Duoni, Xiang Yu, and Weizhong Qian. The Application of Carbon Nanotube/Graphene-Based Nanomaterials in Wastewater Treatment. *Small*, 16(15):1902301, April 2020.

[98] Inanc Meric, Melinda Y. Han, Andrea F. Young, Barbaros Ozyilmaz, Philip Kim, and Kenneth L. Shepard. Current saturation in zero-bandgap, top-gated graphene field-effect transistors. *Nature Nanotechnology*, 3(11):654–659, November 2008.

[99] J. Scott Bunch, Arend M. Van Der Zande, Scott S. Verbridge, Ian W. Frank, David M. Tanenbaum, Jeevak M. Parpia, Harold G. Craighead, and Paul L. McEuen. Electromechanical Resonators from Graphene Sheets. *Science*, 315(5811):490–493, January 2007.

[100] F. H. L. Koppens, T. Mueller, Ph. Avouris, A. C. Ferrari, M. S. Vitiello, and M. Polini. Photodetectors based on graphene, other two-dimensional materials and hybrid systems. *Nature Nanotechnology*, 9(10):780–793, October 2014.

[101] Rinaldo Raccichini, Alberto Varzi, Stefano Passerini, and Bruno Scrosati. The role of graphene for electrochemical energy storage. *Nature Materials*, 14(3):271–279, March 2015.

[102] Shikai Deng and Vikas Berry. Wrinkled, rippled and crumpled graphene: an overview of formation mechanism, electronic properties, and applications. *Materials Today*, 19(4):197–212, May 2016.

[103] Xi Shen, Zhenyu Wang, Ying Wu, Xu Liu, Yan-Bing He, and Jang-Kyo Kim. Multilayer Graphene Enables Higher Efficiency in Improving Thermal Conductivities of Graphene/Epoxy Composites. *Nano Letters*, 16(6):3585–3593, June 2016.

[104] Ryota Negishi, Chaopeng Wei, Yao Yao, Yui Ogawa, Masashi Akabori, Yasushi Kanai, Kazuhiko Matsumoto, Yoshitaka Taniyasu, and Yoshihiro Kobayashi. Turbostratic Stacking Effect in Multilayer Graphene on the Electrical Transport Properties. *physica status solidi (b)*, 257(2):1900437, February 2020.

[105] Sylvain Latil, Vincent Meunier, and Luc Henrard. Massless fermions in multilayer graphitic systems with misoriented layers: *Ab initio* calculations and experimental fingerprints. *Physical Review B*, 76(20):201402, November 2007.

[106] M. Michael Denner, J. L. Lado, and Oded Zilberberg. Antichiral states in twisted graphene multilayers. *Physical Review Research*, 2(4):043190, November 2020.

[107] Yung-Chang Lin, Amane Motoyama, Pablo Solís-Fernández, Rika Matsumoto, Hiroki Ago, and Kazu Suenaga. Coupling and Decoupling of Bilayer Graphene Monitored by Electron Energy Loss Spectroscopy. *Nano Letters*, 21(24):10386–10391, December 2021.

[108] Zizhao Xu, Taiki Inoue, Yuta Nishina, and Yoshihiro Kobayashi. Stacking order reduction in multilayer graphene by inserting nanospacers. *Journal of Applied Physics*, 132(17):174305, November 2022.

[109] Xu Du, Ivan Skachko, Anthony Barker, and Eva Y. Andrei. Approaching ballistic transport in suspended graphene. *Nature Nanotechnology*, 3(8):491–495, August 2008.

[110] Stéphane Berciaud, Sunmin Ryu, Louis E. Brus, and Tony F. Heinz. Probing the Intrinsic Properties of Exfoliated Graphene: Raman Spectroscopy of Free-Standing Monolayers. *Nano Letters*, 9(1):346–352, January 2009.

[111] Jannik C. Meyer, A. K. Geim, M. I. Katsnelson, K. S. Novoselov, T. J. Booth, and S. Roth. The structure of suspended graphene sheets. *Nature*, 446(7131):60–63, March 2007.

[112] K.I. Bolotin, K.J. Sikes, Z. Jiang, M. Klima, G. Fudenberg, J. Hone, P. Kim, and H.L. Stormer. Ultrahigh electron mobility in suspended graphene. *Solid State Communications*, 146(9-10):351–355, June 2008.

[113] Niklas Lindahl, Daniel Midtvedt, Johannes Svensson, Oleg A. Nerushev, Niclas Lindvall, Andreas Isacsson, and Eleanor E. B. Campbell. Determination of the Bending Rigidity of Graphene via Electrostatic Actuation of Buckled Membranes. *Nano Letters*, 12(7):3526–3531, July 2012.

[114] Alexandre F Fonseca, Sócrates O Dantas, Douglas S Galvão, Difan Zhang, and Susan B Sinnott. The structure of graphene on graphene/C $_{60}$ /Cu interfaces: a molecular dynamics study. *Nanotechnology*, 30(50):505707, December 2019.

[115] Javier Varillas and Otakar Frank. Wrinkle development in graphene sheets with patterned nano-protrusions: A molecular dynamics study. *Carbon*, 173:301–310, March 2021.

[116] Kai Haraguchi, Sogo Iwakami, and Tomonori Ohba. Fabrication of Fullerene-Pillared Porous Graphene and Its Water Vapor Adsorption. *The Journal of Physical Chemistry C*, 127(25):12333–12341, June 2023.

[117] Shengnan Wang, Hiroki Hibino, Satoru Suzuki, and Hideki Yamamoto. Atmospheric Pressure Chemical Vapor Deposition Growth of Millimeter-Scale Single-Crystalline Graphene on the Copper Surface with a Native Oxide Layer. *Chemistry of Materials*, 28(14):4893–4900, July 2016.

[118] Yui Ogawa, Yuya Murata, Satoru Suzuki, Hiroki Hibino, Stefan Heun, Yoshitaka Taniyasu, and Kazuhide Kumakura. Surface structures of graphene covered Cu(103). *Japanese Journal of Applied Physics*, 57(10):100301, October 2018.

[119] Xuesong Li, Yanwu Zhu, Weiwei Cai, Mark Borysiak, Boyang Han, David Chen, Richard D. Piner, Luigi Colombo, and Rodney S. Ruoff. Transfer of Large-Area Graphene Films for High-Performance Transparent Conductive Electrodes. *Nano Letters*, 9(12):4359–4363, December 2009.

[120] Ji Won Suk, Alexander Kitt, Carl W. Magnuson, Yufeng Hao, Samir Ahmed, Jinho An, Anna K. Swan, Bennett B. Goldberg, and Rodney S. Ruoff. Transfer of CVD-Grown Monolayer Graphene onto Arbitrary Substrates. *ACS Nano*, 5(9):6916–6924, September 2011.

[121] Andres Castellanos-Gomez, Michele Buscema, Rianda Molenaar, Vibhor Singh, Laurens Janssen, Herre S J Van Der Zant, and Gary A Steele. Deterministic transfer of two-dimensional materials by all-dry viscoelastic stamping. *2D Materials*, 1(1):011002, April 2014.

[122] Filippo Pizzocchero, Lene Gammelgaard, Bjarke S. Jessen, José M. Caridad, Lei Wang, James Hone, Peter Bøggild, and Timothy J. Booth. The hot pick-up technique for batch assembly of van der Waals heterostructures. *Nature Communications*, 7(1):11894, June 2016.

[123] Satoshi Toyoda, Teerayut Uwanno, Takashi Taniguchi, Kenji Watanabe, and Kosuke Nagashio. Pinpoint pick-up and bubble-free assembly of 2D materials using PDMS/PMMA polymers with lens shapes. *Applied Physics Express*, 12(5):055008, May 2019.

[124] A Jorio, M A Pimenta, A G Souza Filho, R Saito, G Dresselhaus, and M S Dresselhaus. Characterizing carbon nanotube samples with resonance Raman scattering. *New Journal of Physics*, 5:139–139, October 2003.

[125] Paulo T. Araujo, Stephen K. Doorn, Svetlana Kilina, Sergei Tretiak, Erik Einarsson, Shigeo Maruyama, Helio Chacham, Marcos A. Pimenta, and Ado Jorio. Third and Fourth Optical Transitions in Semiconducting Carbon Nanotubes. *Physical Review Letters*, 98(6):067401, February 2007.

[126] H. Zhao, K. Min, and N. R. Aluru. Size and Chirality Dependent Elastic Properties of Graphene Nanoribbons under Uniaxial Tension. *Nano Letters*, 9(8):3012–3015, August 2009.

[127] K. Min and N. R. Aluru. Mechanical properties of graphene under shear deformation. *Applied Physics Letters*, 98(1):013113, January 2011.

[128] Q.X. Pei, Y.W. Zhang, and V.B. Shenoy. A molecular dynamics study of the mechanical properties of hydrogen functionalized graphene. *Carbon*, 48(3):898–904, March 2010.

[129] Teng Zhang, Xiaoyan Li, and Huajian Gao. Defects controlled wrinkling and topological design in graphene. *Journal of the Mechanics and Physics of Solids*, 67:2–13, July 2014.

[130] Luiz A. Ribeiro Junior, Marcelo L. Pereira Junior, and Alexandre F. Fonseca. Elastocaloric Effect in Graphene Kirigami. *Nano Letters*, 23(18):8801–8807, September 2023.

[131] Bohayra Mortazavi, Brahmanandam Javvaji, Fazel Shojaei, Timon Rabczuk, Alexander V. Shapeev, and Xiaoying Zhuang. Exceptional piezoelectricity, high thermal conductivity and stiffness and promising photocatalysis in two-dimensional MoSi2N4 family confirmed by first-principles. *Nano Energy*, 82:105716, April 2021.

[132] Bohayra Mortazavi, Mohammad Silani, Evgeny V. Podryabinkin, Timon Rabczuk, Xiaoying Zhuang, and Alexander V. Shapeev. First-Principles Multiscale Modeling of Mechanical Properties in Graphene/Borophene Heterostructures Empowered by Machine-Learning Interatomic Potentials. *Advanced Materials*, 33(35):2102807, September 2021.

[133] Zachary H. Aitken and Rui Huang. Effects of mismatch strain and substrate surface corrugation on morphology of supported monolayer graphene. *Journal of Applied Physics*, 107(12):123531, June 2010.

[134] Hongwei Zhang, Zhengrong Guo, Hong Gao, and Tienchong Chang. Stiffness-dependent interlayer friction of graphene. *Carbon*, 94:60–66, November 2015.

[135] Kunqi Wang, Wengen Ouyang, Wei Cao, Ming Ma, and Quanshui Zheng. Robust superlubricity by strain engineering. *Nanoscale*, 11(5):2186–2193, 2019.

[136] Tao Jiang and Yong Zhu. Measuring graphene adhesion using atomic force microscopy with a microsphere tip. *Nanoscale*, 7(24):10760–10766, 2015.

[137] Steven P. Koenig, Narasimha G. Boddeti, Martin L. Dunn, and J. Scott Bunch. Ultrastrong adhesion of graphene membranes. *Nature Nanotechnology*, 6(9):543–546, September 2011.

[138] Xiangyang Gao, Xiyu Yu, Buxuan Li, Shangchun Fan, and Cheng Li. Measuring Graphene Adhesion on Silicon Substrate by Single and Dual Nanoparticle-Loaded Blister. *Advanced Materials Interfaces*, 4(9):1601023, May 2017.

[139] S. Sonde, F. Giannazzo, V. Raineri, and E. Rimini. Dielectric thickness dependence of capacitive behavior in graphene deposited on silicon dioxide. *Journal of Vacuum Science & Technology B: Microelectronics and Nanometer Structures*, 27(2):868, 2009.

[140] Masa Ishigami, J. H. Chen, W. G. Cullen, M. S. Fuhrer, and E. D. Williams. Atomic Structure of Graphene on SiO_2. *Nano Letters*, 7(6):1643–1648, June 2007.

[141] Andrea C. Ferrari and Denis M. Basko. Raman spectroscopy as a versatile tool for studying the properties of graphene. *Nature Nanotechnology*, 8(4):235–246, April 2013.

[142] L. G. Cançado, A. Jorio, E. H. Martins Ferreira, F. Stavale, C. A. Achete, R. B. Capaz, M. V. O. Moutinho, A. Lombardo, T. S. Kulmala, and A. C. Ferrari. Quantifying Defects in Graphene via Raman Spectroscopy at Different Excitation Energies. *Nano Letters*, 11(8):3190–3196, August 2011.

[143] Yee Kan Koh, Myung-Ho Bae, David G. Cahill, and Eric Pop. Reliably Counting Atomic Planes of Few-Layer Graphene ($n > 4$). *ACS Nano*, 5(1):269–274, January 2011.

[144] You-Shin No, Hong Kyw Choi, Jin-Soo Kim, Hakseong Kim, Young-Jun Yu, Choon-Gi Choi, and Jin Sik Choi. Layer number identification of CVD-grown multilayer graphene using Si peak analysis. *Scientific Reports*, 8(1):571, January 2018.

[145] A. C. Ferrari, J. C. Meyer, V. Scardaci, C. Casiraghi, M. Lazzeri, F. Mauri, S. Piscanec, D. Jiang, K. S. Novoselov, S. Roth, and A. K. Geim. Raman Spectrum of Graphene and Graphene Layers. *Physical Review Letters*, 97(18):187401, October 2006.

[146] Ying Ying Wang, Zhen Hua Ni, Ting Yu, Ze Xiang Shen, Hao Min Wang, Yi Hong Wu, Wei Chen, and Andrew Thye Shen Wee. Raman Studies of Monolayer Graphene: The Substrate Effect. *The Journal of Physical Chemistry C*, 112(29):10637–10640, July 2008.

[147] Kwanpyo Kim, Sinisa Coh, Liang Z. Tan, William Regan, Jong Min Yuk, Eric Chatterjee, M. F. Crommie, Marvin L. Cohen, Steven G. Louie, and A. Zettl. Raman Spectroscopy Study of Rotated Double-Layer Graphene: Misorientation-Angle Dependence of Electronic Structure. *Physical Review Letters*, 108(24):246103, June 2012.

[148] Rui He, Ting-Fung Chung, Conor Delaney, Courtney Keiser, Luis A. Jauregui, Paul M. Shand, C. C. Chancey, Yanan Wang, Jiming Bao, and Yong P. Chen. Observation of Low Energy Raman Modes in Twisted Bilayer Graphene. *Nano Letters*, 13(8):3594–3601, August 2013.

[149] Zhen Hua Ni, Ting Yu, Zhi Qiang Luo, Ying Ying Wang, Lei Liu, Choun Pei Wong, Jianmin Miao, Wei Huang, and Ze Xiang Shen. Probing Charged Impurities in Suspended Graphene Using Raman Spectroscopy. *ACS Nano*, 3(3):569–574, March 2009.

[150] Linda Vaisman, H. Daniel Wagner, and Gad Marom. The role of surfactants in dispersion of carbon nanotubes. *Advances in Colloid and Interface Science*, 128-130:37–46, December 2006.

[151] Frank Schwierz. Graphene transistors. *Nature Nanotechnology*, 5(7):487–496, July 2010.

[152] Qiaoliang Bao and Kian Ping Loh. Graphene Photonics, Plasmonics, and Broadband Optoelectronic Devices. *ACS Nano*, 6(5):3677–3694, May 2012.

[153] Jinhua Li, Liyong Niu, Zijian Zheng, and Feng Yan. Photosensitive Graphene Transistors. *Advanced Materials*, 26(31):5239–5273, August 2014.

[154] Wangyang Fu, Lin Jiang, Erik P. Van Geest, Lia M. C. Lima, and Grégory F. Schneider. Sensing at the Surface of Graphene Field-Effect Transistors. *Advanced Materials*, 29(6):1603610, February 2017.

[155] Yuan Cao, Valla Fatemi, Shiang Fang, Kenji Watanabe, Takashi Taniguchi, Efthimios Kaxiras, and Pablo Jarillo-Herrero. Unconventional superconductivity in magic-angle graphene superlattices. *Nature*, 556(7699):43–50, April 2018.

[156] Ghulam Abbas, Yu Li, Huide Wang, Wen-Xing Zhang, Cong Wang, and Han Zhang. Recent Advances in Twisted Structures of Flatland Materials and Crafting Moiré Superlattices. *Advanced Functional Materials*, 30(36):2000878, September 2020.

[157] Le Cai and Gui Yu. Fabrication Strategies of Twisted Bilayer Graphenes and Their Unique Properties. *Advanced Materials*, 33(13):2004974, April 2021.

[158] Umesha Mogera and Giridhar U. Kulkarni. A new twist in graphene research: Twisted graphene. *Carbon*, 156:470–487, January 2020.

[159] Mingda Ding, Taiki Inoue, John Isaac Enriquez, Harry Handoko Halim, Yui Ogawa, Yoshitaka Taniyasu, Yuji Hamamoto, Yoshitada Morikawa, and Yoshihiro Kobayashi. Reduction of Interlayer Interaction in Multilayer Stacking Graphene with Carbon Nanotube Insertion: Insights from Experiment and Simulation. *The Journal of Physical Chemistry C*, 127(49):23768–23777, December 2023.

[160] Deep Jariwala, Tobin J. Marks, and Mark C. Hersam. Mixed-dimensional van der Waals heterostructures. *Nature Materials*, 16(2):170–181, February 2017.

[161] Kin Fai Mak, Matthew Y. Sfeir, James A. Misewich, and Tony F. Heinz. The evolution of electronic structure in few-layer graphene revealed by optical spectroscopy. *Proceedings of the National Academy of Sciences*, 107(34):14999–15004, August 2010.

[162] Asaf Bolker, Cecile Saguy, Moshe Tordjman, and Rafi Kalish. Quantum confinement and Coulomb blockade in isolated nanodiamond crystallites. *Physical Review B*, 88(3):035442, July 2013.

[163] Qi Wang, Nareerat Plylahan, Manjusha V. Shelke, Rami Reddy Devarapalli, Musen Li, Palaniappan Subramanian, Thierry Djenizian, Rabah Boukherroub, and Sabine Szunerits. Nanodiamond particles/reduced graphene oxide composites as efficient supercapacitor electrodes. *Carbon*, 68:175–184, March 2014.

[164] Housseinou Ba, Seetharamulu Podila, Yuefeng Liu, Xiaoke Mu, Jean-Mario Nhut, Vasiliki Papaefthimiou, Spyridon Zafeiratos, Pascal Granger, and Cuong Pham-Huu. Nanodiamond decorated few-layer graphene composite as an efficient metal-free dehydrogenation catalyst for styrene production. *Catalysis Today*, 249:167–175, July 2015.

[165] Chi Cheng, Gengping Jiang, Christopher J. Garvey, Yuanyuan Wang, George P. Simon, Jefferson Z. Liu, and Dan Li. Ion transport in complex layered graphene-based membranes with tuneable interlayer spacing. *Science Advances*, 2(2):e1501272, February 2016.

[166] Zengguang Cheng, Qiaoyu Zhou, Chenxuan Wang, Qiang Li, Chen Wang, and Ying Fang. Toward Intrinsic Graphene Surfaces: A Systematic Study on Thermal Annealing and Wet-Chemical Treatment of SiO $_2$ -Supported Graphene Devices. *Nano Letters*, 11(2):767–771, February 2011.

[167] A. Pirkle, J. Chan, A. Venugopal, D. Hinojos, C. W. Magnuson, S. McDonnell, L. Colombo, E. M. Vogel, R. S. Ruoff, and R. M. Wallace. The effect of chemical residues on the physical and electrical properties of chemical vapor deposited graphene transferred to SiO2. *Applied Physics Letters*, 99(12):122108, September 2011.

[168] Xiaohan Wang, Andrei Dolocan, Harry Chou, Li Tao, Andrew Dick, Deji Akinwande, and C. Grant Willson. Direct Observation of Poly(Methyl Methacrylate) Removal from a Graphene Surface. *Chemistry of Materials*, 29(5):2033–2039, March 2017.

[169] L.G. Cançado, K. Takai, T. Enoki, M. Endo, Y.A. Kim, H. Mizusaki, N.L. Speziali, A. Jorio, and M.A. Pimenta. Measuring the degree of stacking order in graphite by Raman spectroscopy. *Carbon*, 46(2):272–275, February 2008.

[170] Y. Y. Wang, Z. H. Ni, Z. X. Shen, H. M. Wang, and Y. H. Wu. Interference enhancement of Raman signal of graphene. *Applied Physics Letters*, 92(4):043121, January 2008.

[171] Pablo Solís-Fernández and Hiroki Ago. Machine Learning Determination of the Twist Angle of Bilayer Graphene by Raman Spectroscopy: Implications for van der Waals Heterostructures. *ACS Applied Nano Materials*, 5(1):1356–1366, January 2022.

[172] Ji Eun Lee, Gwanghyun Ahn, Jihye Shim, Young Sik Lee, and Sunmin Ryu. Optical separation of mechanical strain from charge doping in graphene. *Nature Communications*, 3(1):1024, August 2012.

[173] T. M. G. Mohiuddin, A. Lombardo, R. R. Nair, A. Bonetti, G. Savini, R. Jalil, N. Bonini, D. M. Basko, C. Galiotis, N. Marzari, K. S. Novoselov, A. K. Geim, and A. C. Ferrari. Uniaxial strain in graphene by Raman spectroscopy: G peak splitting, Grüneisen parameters, and sample orientation. *Physical Review B*, 79(20):205433, May 2009.

[174] Yuhang Jiang, Jinhai Mao, Junxi Duan, Xinyuan Lai, Kenji Watanabe, Takashi Taniguchi, and Eva Y. Andrei. Visualizing Strain-Induced Pseudomagnetic Fields in Graphene through an hBN Magnifying Glass. *Nano Letters*, 17(5):2839–2843, May 2017.

[175] Dong-Ho Kang, Hao Sun, Manlin Luo, Kunze Lu, Melvina Chen, Youngmin Kim, Yongduck Jung, Xuejiao Gao, Samuel Jior Parluhutan, Junyu Ge, See Wee Koh, David Giovanni, Tze Chien Sum, Qi Jie Wang, Hong Li, and Donguk Nam. Pseudomagnetic field-induced slow carrier dynamics in periodically strained graphene. *Nature Communications*, 12(1):5087, August 2021.

[176] Antoine Reserbat-Plantey, Dipankar Kalita, Zheng Han, Laurence Ferlazzo, Sandrine Autier-Laurent, Katsuyoshi Komatsu, Chuan Li, Raphaël Weil, Arnaud Ralko, Laëtitia Marty, Sophie Guéron, Nedjma Bendiab, Hélène Bouchiat, and Vincent Bouchiat. Strain Superlattices and Macroscale Suspension of Graphene Induced by Corrugated Substrates. *Nano Letters*, 14(9):5044–5051, September 2014.

[177] C.-C. Hsu, M. L. Teague, J.-Q. Wang, and N.-C. Yeh. Nanoscale strain engineering of giant pseudo-magnetic fields, valley polarization, and topological channels in graphene. *Science Advances*, 6(19):eaat9488, May 2020.

[178] Si-Yu Li, Ying Su, Ya-Ning Ren, and Lin He. Valley Polarization and Inversion in Strained Graphene via Pseudo-Landau Levels, Valley Splitting of Real Landau Levels, and Confined States. *Physical Review Letters*, 124(10):106802, March 2020.

[179] Jie Ma, Dario Alfè, Angelos Michaelides, and Enge Wang. Stone-Wales defects in graphene and other planar s p 2 -bonded materials. *Physical Review B*, 80(3):033407, July 2009.

[180] O. Lehtinen, S. Kurasch, A.V. Krasheninnikov, and U. Kaiser. Atomic scale study of the life cycle of a dislocation in graphene from birth to annihilation. *Nature Communications*, 4(1):2098, June 2013.

[181] Te-Huan Liu, Grzegorz Gajewski, Chun-Wei Pao, and Chien-Cheng Chang. Structure, energy, and structural transformations of graphene grain boundaries from atomistic simulations. *Carbon*, 49(7):2306–2317, June 2011.

[182] Xi Shen, Xiuyi Lin, Nariman Yousefi, Jingjing Jia, and Jang-Kyo Kim. Wrinkling in graphene sheets and graphene oxide papers. *Carbon*, 66:84–92, January 2014.

[183] Lev Davidovich Landau and Evgenij M Lifshitz. *Theory of elasticity: volume 7*, volume 7. Elsevier, 1986.

[184] Yujie Wei, Baoling Wang, Jiangtao Wu, Ronggui Yang, and Martin L. Dunn. Bending Rigidity and Gaussian Bending Stiffness of Single-Layered Graphene. *Nano Letters*, 13(1):26–30, January 2013.

[185] Edmund Han, Jaehyung Yu, Emil Annevelink, Jangyup Son, Dongyun A. Kang, Kenji Watanabe, Takashi Taniguchi, Elif Ertekin, Pinshane Y. Huang, and Arend M. Van Der Zande. Ultrasoft slip-mediated bending in few-layer graphene. *Nature Materials*, 19(3):305–309, March 2020.

[186] Xiaoding Wei, Benjamin Fragneaud, Chris A. Marianetti, and Jeffrey W. Kysar. Nonlinear elastic behavior of graphene: *Ab initio* calculations to continuum description. *Physical Review B*, 80(20):205407, November 2009.

[187] Wen Wang, Shuyang Dai, Xide Li, Jiarui Yang, David J. Srolovitz, and Quanshui Zheng. Measurement of the cleavage energy of graphite. *Nature Communications*, 6(1):7853, August 2015.

[188] Ze Liu, Jefferson Zhe Liu, Yao Cheng, Zhihong Li, Li Wang, and Quanshui Zheng. Interlayer binding energy of graphite: A mesoscopic determination from deformation. *Physical Review B*, 85(20):205418, May 2012.

[189] D. F. Shanno. Conditioning of quasi-newton methods for function minimization. *Mathematics of Computation*, 24(111):647–656, 1970.

[190] C.A. Yan, R. Vescovini, and N. Fantuzzi. A neural network-based approach for bending analysis of strain gradient nanoplates. *Engineering Analysis with Boundary Elements*, 146:517–530, January 2023.

[191] Zhipeng Xiong, Yifeng Yu, Huan Chen, and Lichun Bai. A coarse-grained study on mechanical behaviors of diamond-like carbon based on machine learning. *Nanotechnology*, 34(38):385702, September 2023.

[192] Zesheng Zhang, Yang Hong, Bo Hou, Zhongtao Zhang, Mehrdad Negahban, and Jingchao Zhang. Accelerated discoveries of mechanical properties of graphene using machine learning and high-throughput computation. *Carbon*, 148:115–123, July 2019.

[193] Shuai Wang, Tian Yang, Chao Wang, and Lihong Liang. The mechanical response and microscopic deformation mechanism of graphene foams tuned by long carbon nanotubes and short crosslinkers. *Physical Chemistry Chemical Physics*, 25(1):192–202, 2023.

[194] Yifan Zhao, Yushun Zhao, Fan Wu, Yue Zhao, Yaming Wang, Chao Sui, Xiaodong He, Chao Wang, Huifeng Tan, and Chao Wang. The mechanical behavior and collapse of graphene-assembled hollow nanospheres under compression. *Carbon*, 173:600–608, March 2021.

[195] Xianhong Meng, Bowen Zhang, Hao Li, Fengwei Li, Zhan Kang, Ming Li, and Yuli Chen. A theoretical analysis on self-collapsing of nanotubes. *International Journal of Solids and Structures*, 160:51–58, March 2019.

[196] Y. Magnin, F. Rondepierre, W. Cui, D.J. Dunstan, and A. San-Miguel. Collapse phase diagram of carbon nanotubes with arbitrary number of walls. Collapse modes and macroscopic analog. *Carbon*, 178:552–562, June 2021.

[197] So Jeong Heo, Junghwan Kim, Gyeong Min Choi, Dongju Lee, Byeong Woo Im, Sung-Soo Kim, Bon-Cheol Ku, Heon Sang Lee, and Seo Gyun Kim. Microstructural evolution effects on the density of carbon nanotube fibers. *Carbon*, 226:119180, June 2024.

[198] R. Galafassi, F. Vialla, V. Pischedda, H. Diaf, and A. San-Miguel. Reversible Raman D-band changes: A new probe into the pressure-induced collapse of carbon nanotubes. *Carbon*, 229:119447, October 2024.

[199] Masayuki Hasegawa and Kazume Nishidate. Radial deformation and stability of single-wall carbon nanotubes under hydrostatic pressure. *Physical Review B*, 74(11):115401, September 2006.

[200] Weibang Lu, Tsu-Wei Chou, and Byung-Sun Kim. Radial deformation and its related energy variations of single-walled carbon nanotubes. *Physical Review B*, 83(13):134113, April 2011.

[201] Weibang Lu, Tsu-Wei Chou, and Byung-Sun Kim. Erratum: Radial deformation and its related energy variations of single-walled carbon nanotubes [Phys. Rev. B **83** , 134113 (2011)]. *Physical Review B*, 84(5):059901, August 2011.

[202] Paul Tangney, Rodrigo B. Capaz, Catalin D. Spataru, Marvin L. Cohen, and Steven G. Louie. Structural Transformations of Carbon Nanotubes under Hydrostatic Pressure. *Nano Letters*, 5(11):2268–2273, November 2005.

[203] D. Y. Sun, D. J. Shu, M. Ji, Feng Liu, M. Wang, and X. G. Gong. Pressure-induced hard-to-soft transition of a single carbon nanotube. *Physical Review B*, 70(16):165417, October 2004.

List of publications and conferences

List of publications during doctoral studies:

1. **M. Ding**, T. Inoue, J. I. Enriquez, H. H. Halim, Y. Ogawa, Y. Taniyasu, Y. Hamamoto, Y. Morikawa, Y. Kobayashi, "Experimental and Theoretical Investigation of Nanodiamond Insertion on the Interlayer Interaction in Multilayer Stacking Graphene", ***Carbon*** 229, 119464 (2024).

2. **M. Ding**, T. Inoue, J. I. Enriquez, H. H. Halim, Y. Ogawa, Y. Taniyasu, Y. Hamamoto, Y. Morikawa, Y. Kobayashi, "Reduction of interlayer interaction in multilayer stacking graphene with carbon nanotube insertion: Insights from experiment and simulation", ***Journal of Physical Chemistry C*** 127, 23768 (2023).

3. **M. Ding**, T. Inoue, J. I. Enriquez, H. H. Handoko, Y. Hamamoto, Y. Morikawa, Y. Kobayashi, On the microstructure of stacked graphene and carbon nanotubes: Multistable and hysteresis, (in preparation).

4. **M. Ding**, T. Inoue, Y. Kobayashi, Nonlinear electrical property of graphene-nanodiamond stacking system, (to be published).

5. K. Rong, R. Noro, H. Nishigaki, **M. Ding**, Y. Yao, T. Inoue, R. Katayama, Y. Kobayashi, K. Matsuda, S. Mouri, "Far-reaching Remote Doping for Monolayer MoS_2 Using Ferroelectric Substrate: Unveiling the Impact of h-BN Spacer Thickness", ***ACS Applied Electronic Materials*** 6, 5914–5922 (2024).

List of conferences during doctoral studies:
First author:

1. **M. Ding**, N. Sakurai, T. Inoue, T. Matsuzaki,T. Mizuno, K. Suzuki, J. I. Enriquez, H. H. Halim, Y. Hamamoto, H. Yoshikawa, Y. Morikawa, Y. Kobayashi "Mechanical hysteresis and bi-stability in graphene and carbon nanotube stacked structures" The 68th Fullerenes-Nanotubes-Graphene General Symposium (Meijo University, March 3-5, 2025)

2. **M. Ding**, T. Inoue, J. I. Enriquez, H. H. Halim, Y. Hamamoto, Y. Morikawa, Y. Kobayashi "Nanospacer-Induced Modulation of Interlayer Interactions in Stacked Multilayer Graphene: A Study on Carbon Nanotubes and Nanodiamonds" The 15th Recent Progress in Graphene and 2D Materials Research Conference (RPGR2024), Nanjing Univ., Nanjing China, (July 17-20, 2024).

3. **M. Ding**, T. Inoue, J. I. Enriquez, H. H. Halim, Y. Ogawa, Y. Taniyasu, Y. Hamamoto, Y. Morikawa, Y. Kobayashi "Experimental and computational research on the microstructure of multilayer graphene with nanospacer insertion" The 65th Fullerenes-Nanotubes-Graphene General Symposium (Nishijin Plaza, Kyushu University, Sep.4-Sep.6, 2023)

4. **M. Ding**, T. Inoue, J. I. Enriquez, H. H. Halim, Y. Hamamoto, Y. Morikawa, Y. Kobayashi "Comparative study on stacking structure of graphene/nanospacers by experimental and molecular dynamics approaches" The 64th Fullerenes-Nanotubes-Graphene General Symposium (Nagoya University, Mar. 1-Mar.3, 2023)

5. **M. Ding**, T. Inoue, Y. Ogawa, Y. Taniyasu, Y. Kobayashi "Suppression of interlayer coupling in graphene by inserting nanospacers via a transfer method" The 63rd Fullerenes-Nanotubes-Graphene General Symposium (Tokyo Metropolitan University, Aug.31-Sep.2, 2022)

Co-author:

1. H. Watanabe, K. Suzuki, **M. Ding**, T. Inoue, Y. Kobayashi “Nonlinear electrical characteristics induced by spacer insertion between graphene layers" The 72nd JSAP Spring Meeting 2025, (Tokyo University of Science & online, Mar 14-17, 2025).

2. K. Rong, R. Noro, H. Nishigaki, **M. Ding**, Y. Yao, T. Inoue, R. Katayama, Y. Kobayashi, S. Mouri “Doping effect of MoS2 using periodically polarization-inversed substrate” The 23rd International Conference on the Science and Applications of Nanotubes and Low-Dimensional Materials (NT’23), Arcachon France, (June 4-9, 2023), P045.

3. K. Rong, R. Noro, H. Nishigaki, **M. Ding**, Y. Yao, T. Inoue, R. Katayama, Y. Kobayashi, K. Matsuda, S. Mouri “Remote charge modulation effect of monolayer MoS2 using periodically polarization-inverted structure and hBN spacer layer” JSAP-Optica Joint Symposia (Kumamoto Japan, Sep.19-Sep.23, 2023)

4. K. Rong, R. Noro, H. Nishigaki, **M. Ding**, Y. Yao, T. Inoue, R. Katayama, Y. Kobayashi, K. Matsuda, S. Mouri “Remote charge density modulation of monolayer MoS2 using periodically polarization-inversed ferroelectric substrate” The 65th Fullerenes-Nanotubes-Graphene General Symposium (Nishijin Plaza, Kyushu University, Sep.4-Sep.6, 2023)

5. K. Rong, R. Noro, H. Nishigaki, **M. Ding**, Y. Yao, T. Inoue, R. Katayama, Y. Kobayashi, S. Mouri “Doping effect of MoS2 using periodically polarization-inversed structure” The 64th Fullerenes-Nanotubes-Graphene General Symposium (Nagoya University, Mar. 1-Mar.3, 2023)

Acknowledgements

First and foremost, I would like to express my deepest gratitude to Professor Yoshihiro Kobayashi for his profound knowledge, invaluable guidance, and for providing me with a supportive and independent research environment. His encouragement allowed me to explore and grow as a researcher throughout my doctoral journey.

I am also profoundly grateful to Assistant Professor Taiki Inoue for his detailed and thoughtful guidance, as well as his generous assistance with my experiments.

I would like to thank all the professors and students who collaborated with me on various research projects. First, my sincere thanks go to Professor Yoshitada Morikawa for his insightful guidance on my molecular simulation studies and for reviewing my doctoral thesis. I also extend my gratitude to other members of the Morikawa group, including Associate Professor Yuji Hamamoto, Dr. Harry Halim Handoko, and Dr. John Isaac Enriquez, for their helpful discussions and collaboration. Additionally, I am thankful to Assistant Professor Takahisa Matsusaki and Ms. Nanami Sakurai from the Yoshikawa group for their support with my nano-indentation experiments. My appreciation also goes to Associate Professor Shinichiro Mouri from Ritsumeikan University, Mr. Kaipeng Rong, and Mr. Peishan Yu. Working with you was a delightful experience, and I gained new knowledge through our collaboration.

I would also like to express my gratitude to the reviewers of my doctoral thesis, Professor Yuji Kuwahara, Professor Kanta Ono, and Professor Ry-

ota Negishi, for their valuable feedback and comments, which significantly improved the quality of my work.

My heartfelt thanks go to all members of the Kobayashi Laboratory, both current and past. In particular, I am deeply grateful to Dr. Zizhao Xu, Dr. Mengyue Wang, Ms. Yao Yao, Mr. Yuanjia Liu, Mr. Yungkai Chou, Ms. Yuna Himura, Mr. Man Shen, Mr. Takuo Mizuno, Mr. Kento Suzuki, Mr. Hayato Watanabe, Ms. Sumiyo Kitamura, and Ms. Iku Nakaya. Thank you for supporting me in my daily life, studies, and research. I will always cherish the wonderful moments we shared.

I am also thankful to my fellow students at Osaka University, including Dr. Luting Zhu, Mr. Yuchen Ji, Dr. Shaoxian Li, and many other friends. Spending time with you—whether engaging in sports, pursuing hobbies, or simply enjoying breaks from research—helped me alleviate the stress of academic life.

Finally, I wish to express my deepest gratitude to my parents for their unconditional love, nurturing, and unwavering support throughout my journey.